

# NONLINEAR DYNAMICS OF HEAT-EXCHANGER TUBES UNDER CROSSFLOW: A TIME-DELAY APPROACH

A Thesis Submitted  
in Partial Fulfillment of the Requirements for  
the Degree of

**Doctor of Philosophy**

by

**VARUN VOURGANTI**



भारतीय प्रौद्योगिकी संस्थान हैदराबाद  
Indian Institute of Technology Hyderabad

to the

DEPARTMENT OF MECHANICAL AND AEROSPACE ENGINEERING  
INDIAN INSTITUTE OF TECHNOLOGY HYDERABAD

JANUARY 2020

© Copyright by Varun Vourganti, 2020.  
All Rights Reserved

## Declaration

I declare that this written submission represents my ideas in my own words, and where others' ideas or words have been included, I have adequately cited and referenced the original sources. I also declare that I have adhered to all principles of academic honesty and integrity and have not misrepresented or fabricated or falsified any idea/data/fact/source in my submission. I understand that any violation of the above will be a cause for disciplinary action by the Institute and can also evoke penal action from the sources that have thus not been properly cited, or from whom proper permission has not been taken when needed.



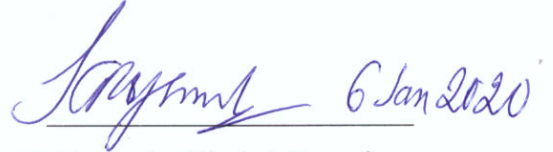
---

Varun Vourganti

ME14RESCH11008

## Approval Sheet

This thesis titled “Nonlinear dynamics of heat exchanger tubes under crossflow: A time delay approach” by Varun Vourganti is approved for the degree of Doctor of Philosophy from IIT Hyderabad.



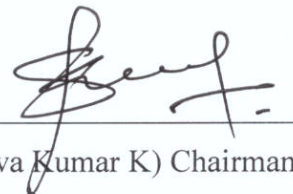
(Prof. K. R. Yogendra Simha) Examiner  
Dept. of Mechanical Engineering  
Indian Institute of Science Bangalore



(Dr. Syed Nizamuddin Khaderi) Internal Examiner  
Dept. of Mechanical and Aerospace Engineering  
Indian Institute of Technology Hyderabad



(Dr. Chandrika Prakash Vyasarayani) Adviser  
Dept. of Mechanical and Aerospace Engineering  
Indian Institute of Technology Hyderabad



(Dr. Siva Kumar K) Chairman  
Dept. of Electrical Engineering  
Indian Institute of Technology Hyderabad

# Acknowledgements

First and foremost, I would like to thank my advisor, Dr. Chandrika Prakash Vyasarayani for his continuous support and valuable insights and while I was pursuing a doctoral degree. I have tremendous gratitude for his fortitude and faith in me, and the utmost admiration for his knowledge and acumen. His guidance was helpful both, during the time of my research and in the writing of this thesis.

I would like to extend my gratitude to my doctoral committee: Dr. Harish, Dr. Syed, and Dr. Anantha Lakshminarayana, for their encouraging words, insightful comments, and challenging questions that incited me to obtain a deeper understanding of my research. I am particularly grateful to the Ministry of Human Resource Development, Government of India, for their monetary assistance during my Ph.D. research, and the Department of Mechanical and Aerospace Engineering for providing me all the appropriate resources for performing my research activities comfortably.

I thank my fellow labmates Ajinkya, Ashwanth, Damodar, Junaidvali, Lala Bahadur, Naresh, Nitish, Sayan, Shanti, Sumit and Surya, for the assisting me every single time I ran into roadblocks, and for their moral support, over the last five years. Also, I thank my wife for her emotional support, for believing in me, and for helping me feel relaxed, refreshed, and lively when the times were tough. I owe my sincerest gratitude to my mother and family members for raising me with care and for their love.

Varun Vourganti

# Abstract

Fluid-conveying heat-exchanger tubes in nuclear power plants are subjected to a secondary cross-flow to facilitate heat exchange. Beyond a critical value of the secondary flow velocity, the tube loses stability and vibrates with large amplitude. The equation governing the dynamics of a heat-exchanger tube is a delay differential equation (DDE). In all the earlier studies, only the stability boundaries in the parametric space of mass-damping parameter and reduced flow-velocity were reported. In this work using Galerkin approximations, the spectrum (characteristic roots) of the DDE is also obtained. The rightmost characteristic root, whose real part represents the damping in the heat-exchanger tube is included in the stability chart for the first time. The highest damping is found to be present in localized areas of the stability charts, which are close to the stability boundaries. These charts can be used to determine the optimal cross-flow velocities for operating the system for achieving maximum damping. Next, the interaction between the tube and the surrounding cladding at the baffle-plate makes it vital to determine the optimal design parameters for the baffle plates.

The linear stability of a heat-exchanger tube modeled as a single-span Euler-Bernoulli cantilever beam subjected to cross-flow is studied with two parameters: (i) varying stiffness of the baffle-cladding at the free end and (ii) varying flow velocity. The partial delay differential equation governing the dynamics of the continuous system is discretized to a set of finite, nonlinear DDEs through a Galerkin method in which a single mode is considered. Unstable regions in the parametric space of cladding stiffness and flow velocity are identified, along with the magnitude of damping in the stable region. This information can be used to determine the design cladding stiffness to achieve maximum damping at a known operational flow velocity. Moreover, the system is found to lose stability by Hopf bifurcation and the method of multiple scales is used to analyze its post-instability behavior. Stable and unstable limit cycles are observed for different values of the linear component of the dimensionless cladding stiffness. An optimal range for the linear cladding stiffness is recommended where tube vibrations would either diminish to zero or assume a relatively low amplitude associated with a stable limit cycle. Furthermore, heat-exchanger tubes undergo thermal expansion, and are consequently subject to thermal loads acting along the axial direction, apart from design-induced external tensile loads.

Nonlinear vibrations of a heat-exchanger tube modeled as a simply-supported Euler-Bernoulli beam under axial load and cross-flow have been studied. The fixed points (zero and buckled equilibria) of the nonlinear DDE are found, and their linear stability is analyzed. The stability of the DDE is investigated in the parametric space of fluid velocity and axial load. The method of multiple scales is used to study the post-instability behavior for both zero and buckled equilibria. Multiple limit-cycles coexist in the parametric space, which has implications on the fatigue life calculations of the heat-exchanger tubes.

# List of Publications

## Journals

1. Desai, A., **Vourganti, V.**, and Vyasarayani, C. P., “A note on damping in heat-exchanger tubes subjected to cross-flow”, *International Journal of Dynamics and Control*, 2019 (published online)
2. **Vourganti, V.**, Kandala, S. S., Meesala, V. C., and Vyasarayani, C. P., “Super-critical and subcritical Hopf bifurcations in a delay differential equation model of a heat exchanger tube under cross-flow”, *ASME Journal of Computational and Nonlinear Dynamics*, 15(2): 021007, 2020 (published)
3. **Vourganti, V.**, Desai. A., Samukham, S., and Vyasarayani, C. P., “Effect of nonlinear cladding stiffness on the stability and Hopf bifurcation of a heat-exchanger tube subject to cross-flow”, *Meccanica*, 2019 (accepted)

# Contents

|  |             |
|--|-------------|
| <b>Acknowledgements</b>  | <b>i</b>    |
| <b>Abstract</b>  | <b>iii</b>  |
| <b>List of Publications</b>  | <b>v</b>    |
| <b>List of Figures</b>   | <b>ix</b>   |
| <b>List of Tables</b>  | <b>xiii</b> |
| <b>List of Abbreviations</b>   | <b>xv</b>   |
| <b>1 Introduction</b>  | <b>1</b>    |
| 1.1 Heat Exchangers in PHWR Nuclear Reactors . . . . .   | 2           |
| 1.2 Cross-flow-induced Tube Vibrations . . . . .   | 3           |
| 1.3 Quasi-steady Model . . . . .   | 8           |
| 1.4 Single Flexible Cylinder in an Array of Rigid Cylinders . . . . .  | 9           |
| 1.5 Time Delay . . . . .   | 9           |
| 1.6 Heat-exchanger tube as Euler-Bernoulli beam . . . . .  | 10          |
| 1.7 Thesis Outline . . . . .   | 11          |
| <b>2 An Investigation of Damping in Heat-Exchanger Tubes</b>   | <b>15</b>   |
| 2.1 Introduction . . . . .   | 15          |
| 2.2 Quasi-steady model of Price and Paidoussis . . . . .   | 15          |
| 2.2.1 Time Delay due to Flow Retardation . . . . .   | 17          |
| 2.2.2 Fluid Forces on a Downstream Cylinder . . . . .  | 18          |
| 2.3 Mathematical Model . . . . .   | 20          |
| 2.4 Results . . . . .  | 25          |
| 2.4.1 Damping in the stable region . . . . .   | 26          |
| 2.4.2 Hopf bifurcation . . . . .   | 29          |
| 2.5 Chapter Summary . . . . .  | 31          |
| <b>3 Effect of Nonlinear Cladding Stiffness on the Stability and Hopf Bifurcation of a Heat-Exchanger Tube Subject to Cross-flow</b> | <b>33</b>   |
| 3.1 Introduction . . . . .   | 33          |



|          |   |            |
|----------|---|------------|
| 3.2      | Mathematical modeling . . . . .   | 35         |
| 3.3      | Stability and bifurcation analysis . . . . .  | 40         |
| 3.3.1    | Linear stability . . . . .  | 40         |
| 3.3.2    | Spectrum . . . . .  | 42         |
| 3.4      | Hopf bifurcation . . . . .  | 47         |
| 3.5      | Method of multiple scales . . . . .   | 49         |
| 3.5.1    | Supercritical Hopf bifurcation at points $P_1, P_3, P_5$ . . . . .  | 52         |
| 3.5.2    | Subcritical Hopf bifurcation at points $P_2$ and $P_4$ . . . . .  | 55         |
| 3.6      | Global bifurcation analysis . . . . .   | 57         |
| 3.7      | Chapter Summary . . . . .   | 60         |
| <b>4</b> | <b>Supercritical and Subcritical Hopf Bifurcations in a Delay Differential Equation Model of a Heat-Exchanger Tube Under Cross-flow</b> . . . . . | <b>63</b>  |
| 4.1      | Introduction . . . . .  | 63         |
| 4.2      | Mathematical modeling . . . . .   | 64         |
| 4.3      | Linear stability . . . . .  | 67         |
| 4.3.1    | Critical curves for the equilibrium at $\bar{q} = \bar{q}_1 = 0$ . . . . .  | 68         |
| 4.3.2    | Critical curves for the equilibrium at $\bar{q} = \bar{q}_2$ . . . . .  | 69         |
| 4.3.3    | Spectrum . . . . .  | 71         |
| 4.4      | Hopf bifurcation . . . . .  | 79         |
| 4.4.1    | Hopf bifurcation for the case of $\bar{q} = \bar{q}_1 = 0$ . . . . .  | 79         |
| 4.4.1.1  | Hopf bifurcation at point $P_1$ . . . . .   | 83         |
| 4.4.1.2  | Hopf bifurcation at point $P_2$ . . . . .   | 84         |
| 4.4.1.3  | Hopf bifurcation at point $P_3$ . . . . .   | 85         |
| 4.4.2    | Hopf bifurcation for the case of $\bar{q} = \bar{q}_2$ . . . . .  | 86         |
| 4.4.2.1  | Hopf bifurcation at point $P_5$ . . . . .   | 91         |
| 4.4.2.2  | Hopf bifurcation at point $P_6$ . . . . .   | 92         |
| 4.4.2.3  | Hopf bifurcation at point $P_7$ . . . . .   | 93         |
| 4.5      | Global bifurcation analysis . . . . .   | 94         |
| 4.6      | Chapter Summary . . . . .   | 97         |
| <b>5</b> | <b>Conclusions and Future Work</b> . . . . .  | <b>99</b>  |
| 5.1      | Open problems and future work . . . . .   | 101        |
|          | <b>References</b> . . . . .   | <b>102</b> |

# List of Figures

|     |   |    |
|-----|---|----|
| 1.1 | Schematic of a CANDU-type nuclear power plant. . . . .  | 2  |
| 1.2 | Schematic of a typical steam generator (heat exchanger) showing its various components including the bundle of U-shaped tubes, as taken from S.F. Corzo et al. [1]. . . . .   | 3  |
| 1.3 | Schematic of a bundle of tubes used in shell-and-tube heat exchangers of CANDU-type nuclear power plants. . . . .   | 4  |
| 1.4 | A compendium of characteristic damage to heat-exchanger tube arrays due to fluidelastic instability: (a) from a CANDU steam generator; (b) from Na <sub>2</sub> H <sub>2</sub> O steam generator; (c) from a steam–steam heat exchanger; (d) from a steam condenser; (e) from another heat exchanger. All figures are taken from Paidoussis et al. [2]. . . . .   | 6  |
| 1.5 | Examples for tube failure by flow-induced vibrations where (a-b) show the tube failure at the support due to fretting wear (modified from Atomic Energy Canada Ltd). (c) Tube failure by clashing between tubes and also fretting wear between tubes and supports (modified from UK Atomic Energy Authority). Figure taken from [3]. . . . .  | 7  |
| 2.1 | Schematic of the two geometries as used in Price and Paidoussis [4]. (a) Geometry I: a double row of flexible cylinders ( $L_s/D = 0.688$ , $T_a/D = 1.191$ ) (b) Geometry II: a double row of flexible cylinders within an array of rigid cylinders ( $L_s/D = 0.688$ , $T_a/D = 1.191$ , $P/D = 1.375$ ). Orange box encloses the double row of flexible cylinders. Figures are not to scale. . . . .   | 16 |
| 2.2 | Schematic of a double row of flexible cylinders with (a) the cylinder numbering. (b) The velocity vector diagram for flow approaching a flexible cylinder. . . . .  | 17 |
| 2.3 | Schematic of a single flexible cylinder (solid blue color) in an array of rigid cylinders subject to cross-flow, as used in [4]. Figure not to scale. . . . .   | 21 |
| 2.4 | Stability chart obtained from the current model along with the stability threshold (red dots) from the model by [4], for $\mu = 1$ in (a) the $[m\delta, U]$ plane and (b) the low mass-damping parameter region demarcated by black dashed-lines in (a). Color map/contours indicate the damping (real part of the rightmost characteristic root). The white region represents the unstable region where the damping is not reported. Experimental data: $\triangleleft$ , Hartlen [5]; $*$ , Heilker and Vincent [6]; $\circ$ , Pettigrew et al. [7]; $+$ , Weaver and Grover [8]; $\bullet$ , Weaver and El-Kashlan [9]. . . . . | 26 |
| 2.5 | Characteristic roots at $m\delta = 1.333$ , and $U = 0.791$ , with the DDE given by $\ddot{y} + 0.218\dot{y} + y + 1.444y(t - \tau) = 0$ as obtained from Eq. (2.22). . . . .   | 27 |

|      |   |    |
|------|---|----|
| 2.6  | Comparison of the stability chart obtained from the current model (color map) and the stability threshold from [4] (red dots) for (a) $\mu = 2$ (b) $\mu = 0.5$ , in the $[m\delta, U]$ plane. Color map/contours indicate the damping (real part of the rightmost characteristic root). The white region represents the unstable region where the damping is not reported. | 29 |
| 2.7  | Variation of the real part of the rightmost characteristic roots with reduced velocity for $m\delta = 1$ , in the vicinity of the critical points. . . . .  | 30 |
| 3.1  | Schematic of (a) a section of a heat exchanger with tubes, baffle plates and claddings, with (b) a top view depicting the square array of tubes, (c) a cross-sectional view of a tube with claddings, where $G_1$ is the baffle-hole diameter (figures not to scale). . . . .   | 35 |
| 3.2  | Schematic of a single flexible tube modeled as a cantilever beam (figure not to scale). . . . .   | 35 |
| 3.3  | Critical curves for Hopf bifurcation for equilibrium point $\bar{q}_1 = 0$ . . . . .  | 42 |
| 3.4  | Stability chart in the $[U, k_1]$ plane obtained from the Galerkin approximation, with color contours representing the damping present in the rightmost root. . . . .   | 45 |
| 3.5  | Characteristic roots of Eq. (3.21a) obtained using Galerkin approximations for $U = 7$ and for (a) $k_1 = 3.85$ , (b) $k_1 = 17.05$ , (c) $k_1 = 33.27$ , (d) $k_1 = 70.55$ , and (e) $k_1 = 91.6$ . . . . .  | 46 |
| 3.6  | Variation of the real part of the rightmost characteristic root of Eq. (3.21a) for $U = 7$ and for $0 < k_1 \leq 100$ . . . . .   | 47 |
| 3.7  | (a) Local bifurcation diagram at point $P_1$ . System response at $P_1$ for (b) $\epsilon\Delta = -1$ with initial conditions for Eqs. (3.56a) and (3.56b) given by point $A_1$ in Fig. 3.7(a) and (c) $\epsilon\Delta = +1$ with initial conditions for Eqs. (3.56a) and (3.56b) given by point $A_2$ in Fig. 3.7(a). . . . .  | 53 |
| 3.8  | (a) Local bifurcation diagram at point $P_3$ . System response at $P_3$ for (b) $\epsilon\Delta = -1$ with initial conditions for Eqs. (3.57a) and (3.57b) given by point $A_1$ in Fig. 3.8(a) and (c) $\epsilon\Delta = +1$ with initial conditions for Eqs. (3.57a) and (3.57b) given by point $A_2$ in Fig. 3.8(a). . . . .  | 54 |
| 3.9  | (a) Local bifurcation diagram at point $P_5$ . System response at point $P_5$ for (b) $\epsilon\Delta = -1$ with initial conditions for Eqs. (3.58a) and (3.58b) given by point $A_1$ in Fig. 3.9(a) and (c) $\epsilon\Delta = +1$ with initial conditions for Eqs. (3.58a) and (3.58b) given by point $A_2$ in Fig. 3.9(a). . . . .  | 54 |
| 3.10 | (a) Local bifurcation diagram at point $P_2$ . System response at point $P_2$ for (b) $\epsilon\Delta = -1$ with initial conditions for Eqs. (3.59a) and (3.59b) given by point $A_1$ in Fig. 3.10(a) and (c) $\epsilon\Delta = -0.1$ with initial conditions for Eqs. (3.59a) and (3.59b) given by point $A_2$ in Fig. 3.10(a). . . . .                                    | 55 |
| 3.11 | (a) Local bifurcation diagram at point $P_4$ . System response at $P_4$ for (b) $\epsilon\Delta = -1$ with initial conditions for Eqs. (3.60a) and (3.60b) given by point $A_1$ in Fig. 3.11(a) and (c) $\epsilon\Delta = -0.1$ with initial conditions for Eqs. (3.60a) and (3.60b) given by point $A_2$ in Fig. 3.11(a). . . . .  | 56 |
| 3.12 | Global bifurcation diagram obtained from Eq. (3.17) for $U = 7$ and $k_1 \in (0, 100]$ , for (a) $k_2 = 50$ and (b) $k_2 = 500$ ; vertical dash-dotted lines represent $k_1 = 5$ , $k_1 = 25$ , and $k_1 = 50$ . . . . .  | 57 |

|      |  |    |
|------|--|----|
| 3.13 | Limit cycles for $U = 7$ with (a) $k_1 = 5$ , (b) $k_1 = 25$ and (c) $k_1 = 50$ . . .  | 59 |
| 4.1  | (a) Schematic of the heat-exchanger tube bundle with its isometric view along with the coordinate axes, (b) the cross-sectional view of the tube bundle, and (c) idealized model of the heat-exchanger tube as a simply supported beam under axial loads and cross flow fluid forces. . . . .  | 65 |
| 4.2  | Two ways in which the rightmost characteristic roots of Eq. (4.13) can cross the imaginary axis, leading to the loss of stability of equilibrium at $\bar{q}$ : (a) $\omega_{cr} \neq 0$ (Hopf bifurcation) and (b) $\omega_{cr} = 0$ (static bifurcation). It should be noted that in both (a) and (b), only the first few rightmost roots of the infinite spectrum of the DDE given by Eq. (4.13) are shown. . . . . | 68 |
| 4.3  | Critical curves for Hopf and static bifurcation for equilibrium points $\bar{q}_1 = 0$ and $\bar{q}_2$ . Curves 1, 2, 4, and 5 correspond to Hopf bifurcation ( $\omega_{cr} \neq 0$ ) and curve 3 corresponds to static bifurcation ( $\omega_{cr} = 0$ ). Six regions are labeled (I to VI) for later discussion. . . . .  | 70 |
| 4.4  | Possible locations of the characteristic roots on the critical curves for the case of (a) $\omega_{cr} \neq 0$ and (b) $\omega_{cr} = 0$ . It should be noted that in both (a) and (b), only the first few rightmost roots of the infinite spectrum of the DDE given by Eq. (4.13) are shown. . . . .  | 71 |
| 4.5  | Stability chart in the $[U, p_0]$ plane, generated using the Galerkin approximation method, with $N = 100$ . Color contours indicate the damping present in the rightmost root. . . . .  | 74 |
| 4.6  | Characteristic roots of Eq. (4.14), obtained using Galerkin approximations for $U = 1$ and for (a) $p_0 = -11.652$ , (b) $p_0 = -7.923$ , (c) $p_0 = 6.978$ , (d) $p_0 = 11.822$ , (e) $p_0 = 19.273$ , and (f) $p_0 = 21.137$ . . . . .   | 77 |
| 4.7  | Characteristic roots of Eq. (4.14) obtained using Galerkin approximations for $U = 1$ and for $p_0 = 10.207$ . . . . .   | 78 |
| 4.8  | Variation of the real part of rightmost characteristic root of Eq. (4.14) for $U = 1$ and for $-15 \leq p_0 \leq 30$ . . . . .   | 78 |
| 4.9  | (a) Local bifurcation diagram at point $P_1$ . System response at local bifurcation point $P_1$ for (b) $\epsilon\Delta = -0.1$ with initial conditions for Eqs. (4.60a) and (4.60b) given by point A1 in Fig. 4.9(a) and (c) $\epsilon\Delta = 0.1$ with initial conditions for Eqs. (4.60a) and (4.60b) given by point A2 in Fig. 4.9(a). . . . .  | 84 |
| 4.10 | (a) Local-bifurcation diagram at point $P_2$ . System response at local bifurcation point $P_2$ for $\epsilon\Delta = 0.1$ with initial conditions for Eqs. (4.61a) and (4.61b) given in Fig. 4.10(a) by point (b) A1 and (c) A2. . . . .  | 85 |
| 4.11 | (a) Local bifurcation diagram at point $P_3$ . System response at local bifurcation point $P_3$ for (b) $\epsilon\Delta = -0.1$ with initial conditions for Eqs. (4.62a) and (4.62b) given by point A1 in Fig. 4.11(a) and (c) $\epsilon\Delta = 0.1$ with initial conditions for Eqs. (4.62a) and (4.62b) given by point A2 in Fig. 4.11(a). . . . .  | 86 |
| 4.12 | (a) Local bifurcation diagram at point $P_5$ . System response at local bifurcation point $P_5$ for $\epsilon^2\Delta = 0.01$ with initial conditions for Eqs. (4.87a) and (4.87b) given in Fig. 4.12(a) by point (b) A1 and (c) A2. . . . .   | 91 |

- 
- 4.13 (a) Local bifurcation diagram at point  $P_6$ . System response at local bifurcation point  $P_6$  for (b)  $\epsilon^2\Delta = -0.01$  with initial conditions for Eqs. (4.88a) and (4.88b) given by point A1 in Fig. 4.13(a) and for (c)  $\epsilon^2\Delta = 0.01$  with initial conditions for Eqs. (4.88a) and (4.88b) given by point A2 in Fig. 4.13(a). . . . . 92
- 4.14 (a) Local bifurcation diagram at point  $P_7$ . System response at local bifurcation point  $P_7$  for  $\epsilon^2\Delta = 0.01$  with initial conditions for Eqs. (4.89a) and (4.89b) given in Fig. 4.14(a) by point (b) A1 and (c) A2. . . . . 93
- 4.15 Global bifurcation diagram of Eq. (4.8) for  $U = 1$  and  $p_0 \in [-15, 30]$ . Stable limit-cycles arising from points  $P_1$ ,  $P_3$  and  $P_6$  are denoted by SLC and the unstable limit-cycles arising from points  $P_2$ ,  $P_5$  and  $P_7$  are denoted by ULC. Stable zero equilibrium is represented by blue solid line (SZE) and the unstable zero equilibrium is represented by dotted blue line (UZE). Magenta solid line represents the stable buckled equilibrium (SBE) and magenta dotted line represents the unstable buckled equilibrium (UBE). . . . . 94
- 4.16 (a) Limit-cycles for  $U = 1$  with (a)  $p_0 = 1$ , (b)  $p_0 = 13$  and (c)  $p_0 = 20$ . 96

# List of Tables

|     |  |    |
|-----|--|----|
| 2.1 | Parametric values borrowed from Price and Paidoussis [4]. . . . .  | 25 |
| 2.2 | Velocity of root-crossing obtained numerically and analytically for the rightmost characteristic roots at the critical points, along $m\delta = 1$ . . . .   | 31 |
| 3.1 | Values of nondimensional parameters $\alpha_1$ to $\alpha_7$ used in the nonlinear DDE given by Eq. (3.13). . . . .  | 39 |
| 3.2 | Values of $k_1^{cr}$ , $\omega_{cr}$ , $\bar{\Gamma}$ (numerical), $\Gamma$ (analytical), and relative error between the latter $\hat{\epsilon} = \left(\frac{\bar{\Gamma}-\Gamma}{\Gamma}\right)$ expressed as a percentage, for points $P_1$ to $P_5$ indicated on the stability chart (see Fig. 3.4). . . . .     | 45 |
| 4.1 | Values of $p_{cr}$ , $\omega_{cr}$ , $\bar{\Gamma}$ (numerical), $\Gamma$ (analytical), and relative error between the latter $\hat{\epsilon} = \left(\frac{\bar{\Gamma}-\Gamma}{\Gamma}\right)$ expressed as a percentage, for different bifurcation points as shown in the stability chart (see Fig. 4.5). . . . . | 75 |

# List of Abbreviations

|       |                                     |
|-------|-------------------------------------|
| CANDU | Canada Deuterium Uranium            |
| CFD   | Computational fluid dynamics        |
| DDE   | Delay differential equation         |
| FEI   | Fluid-elastic instability           |
| FIV   | Flow-induced vibration              |
| FSI   | Fluid-structure interaction         |
| MMS   | Method of multiple scales           |
| PDDE  | Partial delay differential equation |
| PHWR  | Pressurized heavy water reactor     |
| TDS   | Time-delayed system                 |

# Chapter 1

## Introduction

Nuclear power production in India began in 1969 and has grown from an installed capacity of 320MW in 1969 to 6,780 MW in 2017, and planned to be 9,580 MW by end of 2022 and 14,380 MW by end of 2027 [10]. In 2016, the Government of India released a Draft Electricity Plan [11] stating that the capacity of nuclear power projects would be enhanced by 2,800 MW during 2017-2022 and by another 4,800 MW during 2022-2027. The addition of the estimated 7,600 MW of nuclear power by end of 2027, would mean an increase of 112% over the installed capacity of March 2017 [10]. This implies that nuclear power is being looked up to as a prospective resource for addressing the energy needs of this country. Nuclear power has taken the lion's share of pros as compared to cons, and it seems to meet the majority of demands with less cost of operation. First, since nuclear power generation does not rely upon products from fossil fuels, nuclear plants contribute minimally to the greenhouse effect [12]. Secondly, fully loaded nuclear plants can be in continuous operation for 18 to 24 months with fewer interruptions as compared to thermal plants [13]. Third, nuclear power plants occupy minimal space when compared to other power plants. In addition to the Canadian-supplied Canada Deuterium Uranium (CANDU) reactors, India now has six Pressurized Heavy Water Reactors (PHWRs) in operation, modeled on the Canadian-built CANDU type [14]. In fact, nuclear reactors have also been an important source of power generation in the Canadian provinces of Quebec and Ontario. As noted by Khalifa et al. [3], the CANDU reactor, which uses heavy water as the moderator, was invented by Atomic Energy Canada Limited, Canada's largest nuclear technology company and federal Crown corporation in the 1960s. As of August 2007, the Bruce Nuclear Generating Station in Ontario supplies 4,700 MW ( $24 \times 7$ ), which is approximately 20% of the province's supply of power [15]. As of 2010, Gentilly Nuclear Generating Station in Quebec accounts for 635MW [16].



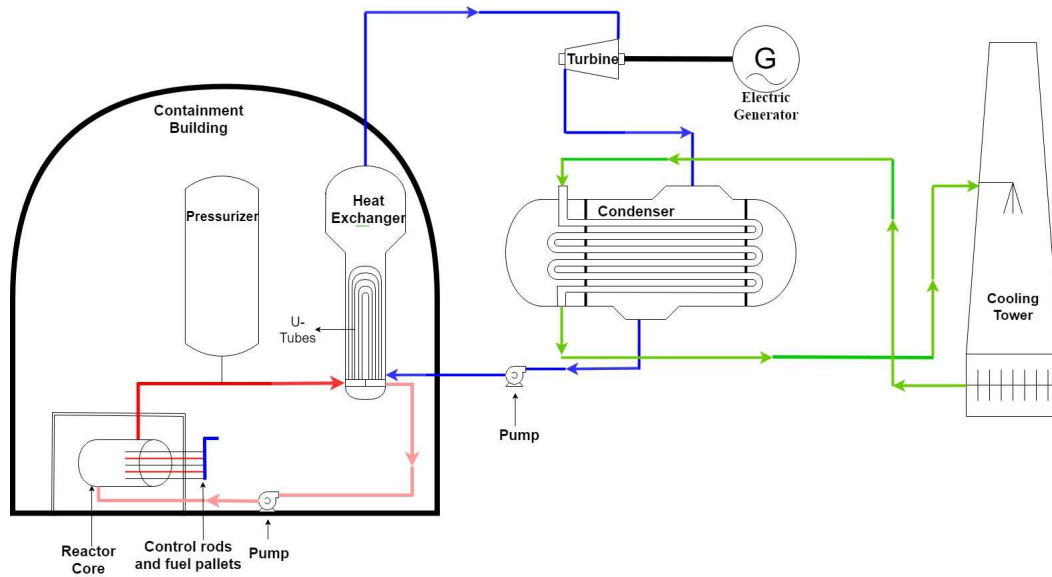


FIGURE 1.1: Schematic of a CANDU-type nuclear power plant.

## 1.1 Heat Exchangers in PHWR Nuclear Reactors

Figure 1.1 shows a schematic of a CANDU-type nuclear power plant. A typical nuclear power plant contains a cylindrical vessel called nuclear core (simply “core”), charged with an array of nuclear fuel pellets clad in zircaloy metal and equipped with a graphite-based control-rod. Heavy water (primary coolant) is utilized for cooling the core and as a moderator to control thermal neutrons that are generated from nuclear fission. Light water (secondary coolant) is used for generating steam. The exothermic heat of a fission reaction diffuses to the primary coolant at a high pressure. The primary fluid passes through long U-shaped tubes of a heat exchanger (Fig. 1.2) [1], where it exchanges heat with the secondary fluid through conduction and convection. The secondary coolant, inside the heat exchanger, extracts a fraction of heat from the primary coolant and is converted to steam. The secondary fluid is fed to the heat exchanger from the top surface of the tubes. A typical shell-and-tube heat exchanger (Fig. 1.3) contains a bundle of U-shaped tubes that are enclosed in a cylindrical shell. Thin baffle plates separate the tubes. They provide structural support and direct the secondary flow across the tubes. The baffle plates are drilled with marginally oversized holes to allow for thermal expansion of tubes and for comfortable fitting.

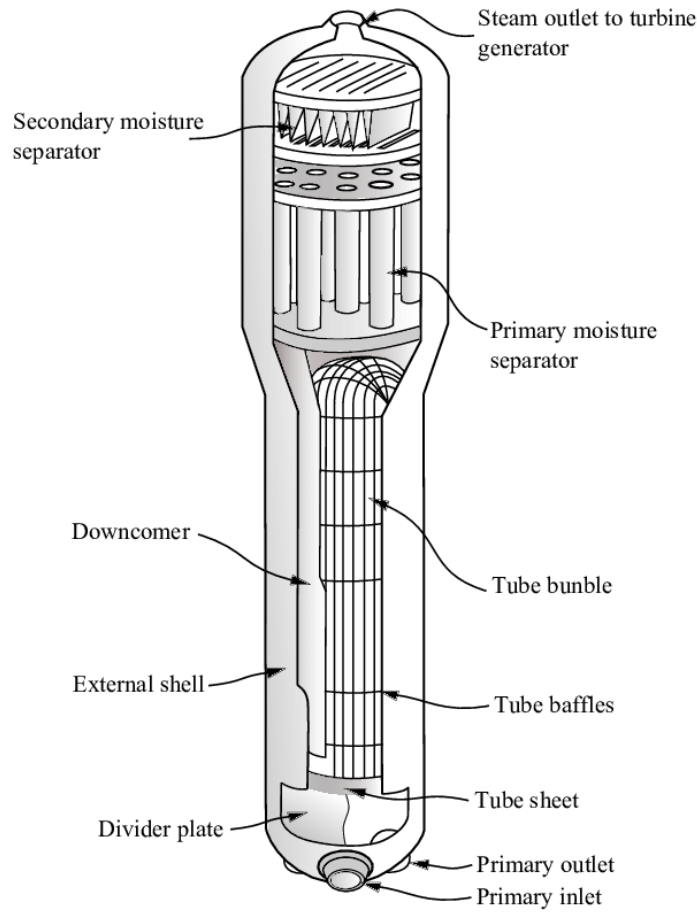


FIGURE 1.2: Schematic of a typical steam generator (heat exchanger) showing its various components including the bundle of U-shaped tubes, as taken from S.F. Corzo et al. [1].

## 1.2 Cross-flow-induced Tube Vibrations

Heat-exchanger tube vibration is one of the primary concerns of heat exchanger failures and sometimes results in plant shutdown, which leads to economic losses. In heat exchangers, the secondary fluid flows across the tubes, and hence the system is called a cross-flow heat exchanger. Tubes extract energy from the secondary flowing fluid and are therefore subject to oscillations in the transverse direction. These oscillations are called cross-flow-induced vibrations. Higher secondary flow velocities enhance the rate of heat transfer between primary and secondary fluids. However, they come with the caveat of increasing the flow-induced vibration (FIV) amplitude. The minimum velocity at which the amplitude growth begins to occur is called critical flow velocity. If the amplitude exceeds the baffle hole clearance gap, the tube impacts against the baffle plate. This results in enlargement of the baffle hole, and fatigue wear-and-tear of the tube surface. Worse, cylinder impact with baffle supports “wears the tubes

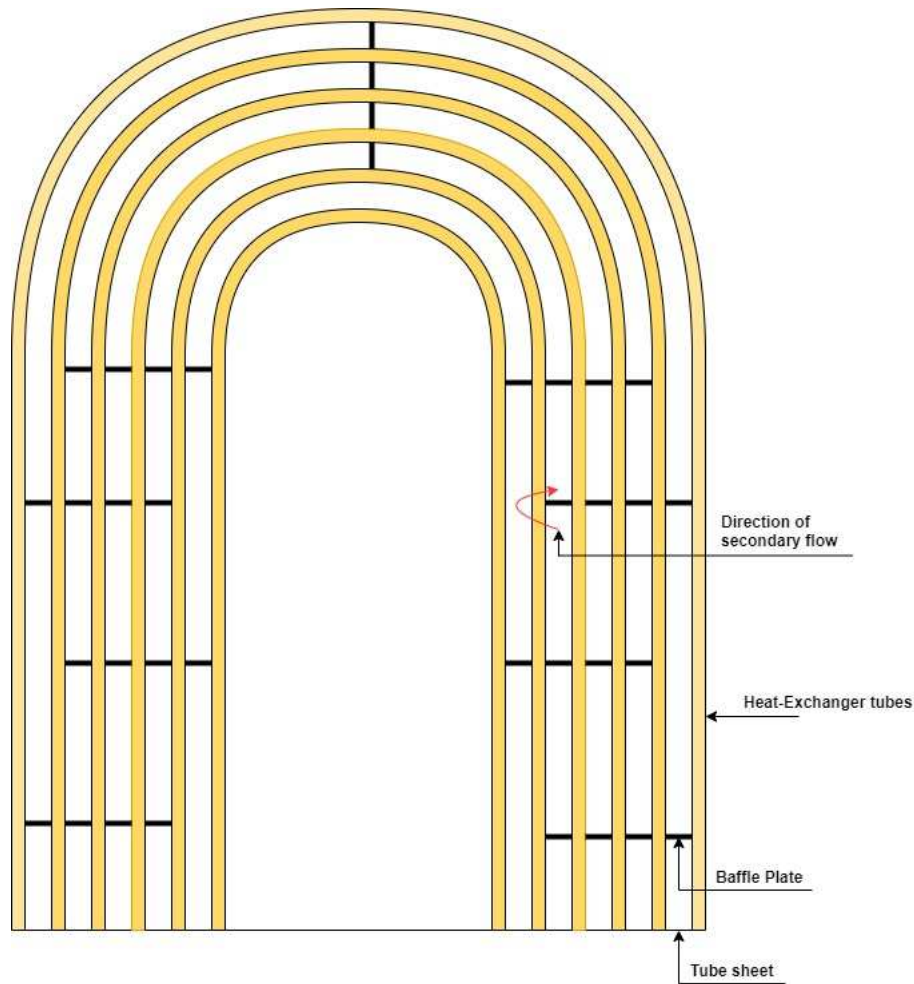


FIGURE 1.3: Schematic of a bundle of tubes used in shell-and-tube heat exchangers of CANDU-type nuclear power plants.

thin till they burst and cuts through the baffle supports, creating a free double-span resulting in higher amplitude vibration” [17]. The low-stiffness in the U-bend region makes it particularly vulnerable to large-amplitude vibrations [3] that result in failure and fretting wear. In some cases of low tube pitch and larger baffle plate distance, tubes may impact with adjacent tubes. Tube failure causes leakage of fluid that carries radioactive material, which can be catastrophic. The causes of flow-induced vibrations are [18]:

- Vortex-shedding: Cylinder-wake instability results in von Karman vortex shedding and causes the cylinder to experience unsteady forces that induce vibrations [19]. The cylinder motion can cause the vortex-shedding frequency to match the vibration frequency resulting in lock-in, which causes the oscillations of the tube to increase.

- Turbulent buffeting: As the flow traverses deep into the array, the detached flow becomes turbulent due to complex interactions. The tubes extract energy from the turbulent flow. When the dominant frequency for the turbulent buffeting matches the natural frequency, a considerable transfer of energy leads to high vibration amplitudes [18].
- Fluid-elastic Instability (FEI).

Among the above, FEI is the most dangerous and difficult to identify. Furthermore, “fluidelastic instability is particularly crucial, as the damage caused by the first two mechanisms over years of service can be produced by fluid-elastic instability in a matter of hours” [3]. According to Chen [20], there are two types of mechanisms for dynamic FEI, which have been summarized here:

- Damping controlled FEI: This type of FEI is also known as velocity-controlled FEI, because the dominant fluid force, i.e., fluid-damping is proportional to the cylinder velocity. This force may act as an energy-dissipation mechanism or an excitation mechanism for structural oscillations [21]. Past the critical velocity, the system becomes unstable when the modal damping becomes negative. This instability can occur in a single elastic cylinder in a rigid array; fluid coupling with other cylinders is not a necessary condition for instability.
- Stiffness-controlled FEI: This type of FEI is also known as displacement-controlled FEI. This is because the dominant fluid force, called fluidelastic force, is proportional to the displacement of the cylinder. The system becomes unstable when the modal damping becomes negative because of the fluidelastic force, at high flow velocity [20]. The phase difference among different cylinders is the essential feature of this type of instability and fluidelastic coupling between cylinders is a necessary condition for stiffness-controlled instability.

Below the critical flow velocity the rate of dissipation of energy is higher than the rate of energy extracted by the structure from the fluid. At the critical velocity, the rate of energy-dissipation and the rate of energy-input from the fluid are equal and undamped oscillation occurs. Beyond the critical velocity, the amplitude of structural oscillations increases and reaches a steady limit cycle. Since tubes in shell-and-tube heat exchangers are thin and long, they are more likely to exhibit damping-controlled FEI [22].

The reliance of the Canadian provinces of Quebec and Ontario on nuclear energy and the catastrophic consequences of fluid-elastic instability in heat exchangers have drawn the attention of researchers at Quebec and Ontario universities. Many of these studies have been summarized here for reference. It should be noted that the problem of fluidelastic instability began receiving attention more than three decades ago. Paidoussis et al. [2] noted: “The existence of fluidelastic instability in cylinder arrays was not discovered till the 1960s, although failures because of it occurred before, but were erroneously attributed to vortex-shedding. Insufficient knowledge, at a time when new designs of nuclear steam generators were being built, with even higher velocities, caused a proliferation of failures worldwide.” Roberts first developed a “semi-empirical analytical model for predicting critical flow velocity for the onset of instability” in a staggered row of cylinders, in 1962 [23]. In 1970, Connors [24] arrived at the well-known Connors Equation, which relates the dimensionless critical velocity to the mass-damping parameter for a single row of cylinders:

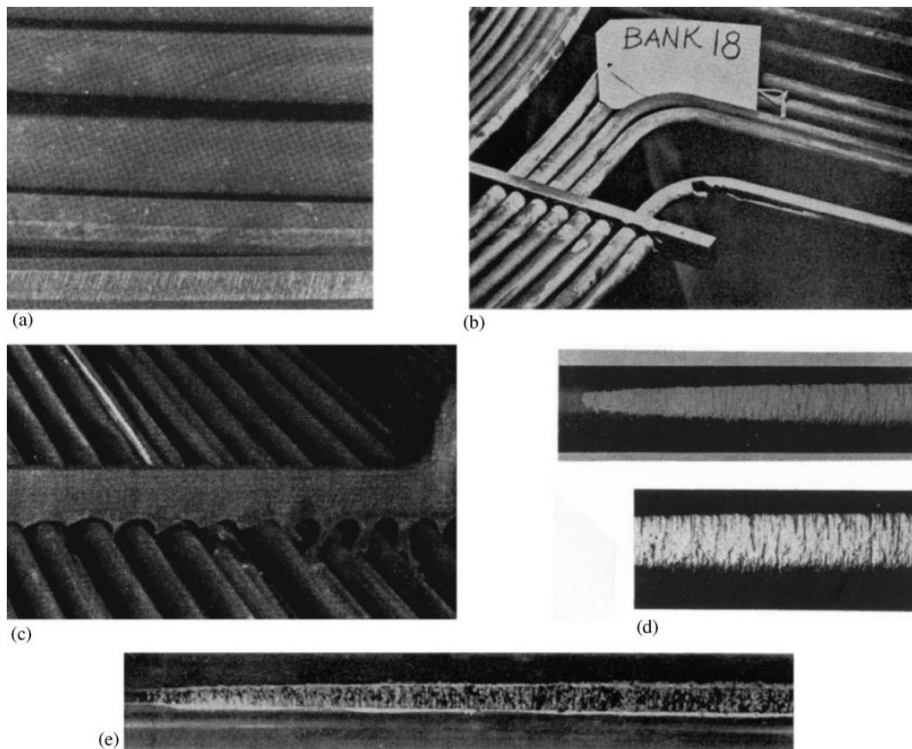


FIGURE 1.4: A compendium of characteristic damage to heat-exchanger tube arrays due to fluidelastic instability: (a) from a CANDU steam generator; (b) from  $\text{Na}_2\text{H}_2\text{O}$  steam generator; (c) from a steam-steam heat exchanger; (d) from a steam condenser; (e) from another heat exchanger. All figures are taken from Paidoussis et al. [2].

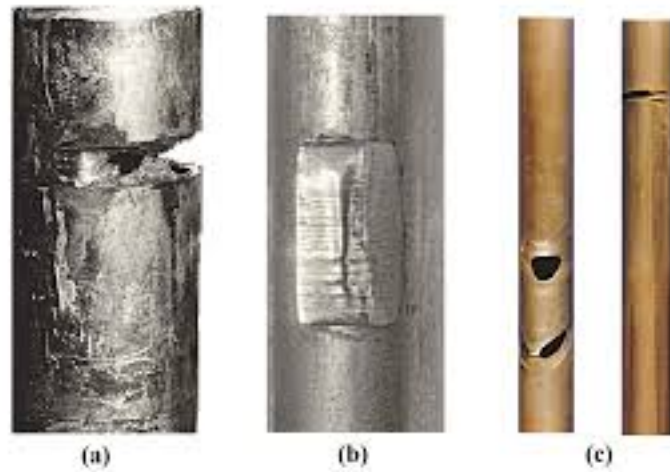


FIGURE 1.5: Examples for tube failure by flow-induced vibrations where (a-b) show the tube failure at the support due to fretting wear (modified from Atomic Energy Canada Ltd). (c) Tube failure by clashing between tubes and also fretting wear between tubes and supports (modified from UK Atomic Energy Authority). Figure taken from [3].

$$\frac{\tilde{U}_c}{fD} = K \left( \frac{M\delta}{\rho D^2} \right)^{0.5}, \quad (1.1)$$

where  $K$  is the well-known Connors coefficient,  $f$  is the natural frequency of the cylinder,  $\tilde{U}_c$  is the critical velocity,  $D$  is the cylinder diameter,  $M$  is its mass per unit length,  $\rho$  is the fluid density and  $\delta$  is the logarithmic decrement. Connors Equation was unjustifiably extended to multi-row cylinder arrays and widely accepted by the industry, leading to severe consequences. It was later discovered that the extension was only valid if  $K$  was taken to be 2.7 – 3.9 [17]. This had ended up in several heat exchangers designed with  $K = 9.9$ , which meant that  $\tilde{U}_c$  was taken to be 3 times what it should have been [17]. To quote [17], “In roughly a decade, the cumulative damages (including power replacement costs) world-wide are estimated at \$1000 M”. A few illustrations demonstrating the damages caused to heat-exchanger tubes due to FEI [3] are presented here for reference (Figs. 1.4 and 1.5). Owing to the extensive curiosity that the phenomenon has generated in the academia and the potential damage that it causes to heat-exchanger tubes, scientific studies for a deeper understanding of the instability mechanism continue.

### 1.3 Quasi-steady Model

Analytical and semi-analytical models have gained more popularity than Computational Fluid Dynamics (CFD) due to the challenges involved in modeling fluid-structure interaction (FSI) problems computationally [25]. First, the differential equations and boundary conditions affiliated to the fluid domain and structural domain need to be satisfied at the same time. Secondly, an extremely reliable mesh-moving scheme must be employed for the fluid domain that changes with change in the structural displacement. The latter must be computed at every time-step. It becomes difficult for the mesh-moving scheme to warrant high accuracy and mesh quality at every time-step, especially for large structural displacements. The computational time and overhead required to implement this procedure for several flow velocities would be immense.

Additionally, flow past an array of cylinders is fraught with turbulence. Different turbulence models yield different pressure responses, which may not comply with experiments (Shinde et al. [26]). Furthermore, in order to capture the complexity of the flow a fine mesh is desirable. First off, modeling of large amplitude vibrations come with the caveat of mesh-element distortion. Furthermore, for a sufficiently fine mesh i.e., for a sufficiently small  $\Delta x$  (cell-size), a time step-size  $\Delta t < c\Delta x/Re$  would be needed for convergence, where  $c$  is a constant for a given tube geometry and incompressible fluid. For a large  $Re$ ,  $\Delta t$  would have to be very small. For a range of velocities, the computational cost and time increases considerably.

Finally, incorporating nonlinearities due to supports becomes difficult in computational studies. Studies like those of Shinde et al. [26], for instance, obtained good agreement with experiments for the damping ratio by availing LES to address the problem of FSI for a harmonically oscillating cylinder. However, nonlinearities due to supports were not accounted for.

For the reasons cited above, this thesis resorts to a semi-analytical approach, instead of a CFD model. The quasi-steady model developed by Price and Paidoussis [4] is utilized in the present study. The quasi-steady model is essentially the quasi-static model but with the inclusion of a frequency-dependent term arising out of the time-delay due to flow retardation (see Section 1.5). The quasi-steady model has several advantages. It facilitates analytical calculations that are not possible in CFD studies. It captures some of the most vital characteristics of the FEI problem when the damping-controlled instability mechanism is more dominant, as is the case in the current study.

## 1.4 Single Flexible Cylinder in an Array of Rigid Cylinders

In this thesis, a single flexible tube within an array of rigid cylinders subjected to cross-flow is considered. Experiments by Lever and Weaver [27] demonstrated that the critical velocity for a single flexible cylinder in an array of rigid cylinders was virtually the same for an array of 19 flexible cylinders. Later, Khalifa et al. [28] provided experimental evidence that a single flexible tube located in the third row of a rigid parallel triangular array becomes fluid-elastically unstable at essentially the same threshold as for the fully flexible array. Therefore, several modern studies have analyzed the stability of a single flexible cylinder. These include: nonlinear models [29–31], CFD models [32, 33], theoretical models [34], as well as empirical and semi-empirical models [35, 36].

Additionally, the single flexible cylinder is constrained to oscillate only in the lift direction. Earlier experimental studies by Weaver and Grover [8], and Weaver and El-Kashlan [9] have concluded that FEI for cylinder arrays is predominant in the transverse direction. Observations made in ref. [4] for a double row of flexible (varying from one to seven in number) cylinders in an array of rigid cylinders indicate that the amplitude of oscillation in the lift direction is larger than the amplitude in the in-line direction by  $\mathcal{O}(2)$ . Based on these observations, several subsequent analyses [34–37] have explored the onset of FEI in cylinder arrays only in the lift direction.

## 1.5 Time Delay

The equation governing the dynamics of the heat-exchanger tube is a delay differential equation (DDE) [4]. The time-delay has been attributed to various mechanisms in the literature. For a single flexible cylinder in an array of rigid cylinders, the quasi-steady model finds that the time-delay between tube displacement and fluid forces is only due to retardation of the flow as it approaches the cylinder array [4]. The quasi-unsteady model [38] attributes the time-delay to the reorganization of the flow as downstream vortices “diffuse-convect” while the tube is in motion. A memory effect of the flow is proposed, as opposed to the flow-retardation effect to account for the time-delay. However, experiments by Mahon and Meskell [35] and Sawadogo and Mureithi [36] were found to be in qualitative agreement with, and of the same order of magnitude as, respectively, the time-delay proposed by Price and Paidoussis [4]. Therefore, in



this thesis, the time-delay is assumed to be constant and is given by  $\Delta T = \mu D/\tilde{U}$ , where  $\tilde{U}$  is the flow velocity. Here,  $\mu \approx \mathcal{O}(1)$ , and we take  $\mu = 1$  [4]. Owing to the presence of the time-delayed displacement term, DDEs are infinite-dimensional systems, and their characteristic equation is a quasi-polynomial that admits infinitely many characteristic roots.

## 1.6 Heat-exchanger tube as Euler-Bernoulli beam

Different studies have modeled the tube as a beam with different physical constraints. Paidoussis and Li [37] modeled a two-span flexible tube within an array of rigid cylinders, as a clamped beam with a loose support at its mid-point. Impact dynamics were modeled using cubic and trilinear springs. Limit-cycle motion was found to exist past the first Hopf bifurcation. For a single-span flexible cantilever in a rigid array, Wang and Ni [29] placed a loose support, modeled as a cubic spring, at the tip (baffle gap). For sufficiently high flow velocities, chaotic and quasi-periodic motions were observed. Xia and Wang [31] explored the post-instability nonlinearity associated with the mean axial extension of a loosely-supported flexible cylinder within an array of rigid cylinders subjected to cross-flow. It was discovered that the nonlinearity related to the force associated with impact against loose supports was more dominant compared to the nonlinearity due to mean axial tension. Wang et al. [30] studied the effect of initial axial load on the instability and nonlinear dynamics of a single flexible tube in an array of rigid cylinders. Numerical simulations indicated the existence of three regions in the parametric space of dimensionless flow velocity and axial load: the stable region, the flutter-instability region, and the buckling-instability region. Recently, Sadath et al. [39] modeled a heat-exchanger tube as a cantilever beam with two loose supports: one located at the mid-span and the other at one end. The impact loading with tube baffles (loose supports) was modeled with either a cubic or a trilinear spring. The analytically-obtained critical velocity at which the system undergoes a Hopf bifurcation compared well with numerically-obtained bifurcation diagrams. Sadath et al. [40] later developed a mathematical model for flow past a simply-supported beam with a loose support at its center (modeled as a cubic spring) and subjected to axial loads. Related work by Cai and Chen [41] studies a pinned-pinned-free beam with impact force represented by linear springs.

## 1.7 Thesis Outline

The ultimate purpose of this thesis is to obtain a better understanding of the physics underlying FEI in heat-exchanger tubes, as the discussion above necessitates. Following the precedent of most of the studies outlined above, a single flexible cylinder in an array of rigid cylinders is considered. The damping-controlled FEI is studied and the tube is constrained to vibrate in the lift direction only.

We have already mentioned that the equation governing the dynamics of a heat-exchanger tube is a delay differential equation (DDE) [4]. DDEs are infinite-dimensional systems, and their characteristic equation is a quasi-polynomial that admits infinitely many characteristic roots. The stability of the DDE is determined by the location of the real part (damping) of the rightmost characteristic root. In the literature, none of the studies have reported the damping contours along with the stability boundaries [4, 32, 33, 42–48]. In **Chapter 2** of this thesis, we would like to fill this gap in the literature. Since DDEs are infinite-dimensional in nature, it is relatively more complex to calculate the characteristic roots of the DDE as compared to calculating the stability boundary. In this Chapter, Galerkin approximations [49] are used to obtain the characteristic roots of the DDE. The damping contours within the stability chart give information about the rate of decay of the vibration response as a function of mass-damping parameter and reduced flow velocity. Contrary to popular belief, operating the heat exchanger deep within the stable region (high mass-damping, low reduced velocity) may not give the best damping behavior. We found that the highest damping values are present in isolated islands in the stability chart and are found to be close to the stability boundary. The damping information reported in this chapter is expected to be useful in the safe and efficient operation of heat exchangers in the industry.

The presence of baffle-supports introduces nonlinearities in the governing equation of motion for the tube. Furthermore, the damage due to tube impact on the surrounding baffle-plates makes it vital to determine the optimal design parameters for the baffle plates. In **Chapter 3**, the linear stability of a heat-exchanger tube modeled as a single-span cantilever beam subjected to cross-flow is studied in the parametric space of the stiffness of the baffle-cladding at the free end and flow velocity. A mathematical model incorporating the motion-dependent fluid forces acting on the beam is developed using the Euler-Bernoulli beam theory, under the inextensible condition. Fluid forces acting on the beam are modeled using an added-mass

coefficient and aerodynamic parameters taken from the literature. The partial delay differential equation (PDDE) governing the dynamics of the continuous system is discretized to a set of finite, nonlinear DDEs through a Galerkin method in which a single mode is considered. The fixed points and the critical curves of the model are derived. The stability chart for the system in the parametric space of dimensionless flow velocity and linear cladding stiffness is presented, along with the spectrum at the points of critical cladding stiffness for a fixed value of flow velocity. The system is found to lose stability by Hopf bifurcation and the method of multiple scales (MMS) is used to analyze its post-instability behavior. Stable and unstable limit cycles are observed for different values of the linear component of the dimensionless cladding stiffness. To the author's knowledge, this is the first time the free end of a cantilever has been modeled as a combination of a linear spring and a cubic spring in the context of research on cross-flow induced instabilities.

Over the past three decades, many researchers have assumed the heat-exchanger tube to be simply supported. Some examples are found in [50–52]. As quoted by Paidoussis and Li [37] – “Supports in real heat exchangers are somewhere between a simple support and a clamped one, and exact integral relationships between frequencies are rather rare.” It should be noted that clamped tubes are stiffer compared to simply-supported tubes. Therefore, the stability results for simply-supported tubes will be more conservative as compared to fixed tubes. Furthermore, if the tubes are long, and if the support thickness is small as compared to the diameter of the tube, a simply-supported boundary condition can be assumed. Another important consideration is that heat-exchanger tubes undergo thermal expansion, and are consequently subject to thermal loads acting along the axial direction, apart from design-induced external tensile loads. Nonlinear vibrations of a heat-exchanger tube modeled as a simply-supported Euler-Bernoulli beam under axial load and cross-flow have been studied in **Chapter 4**. Using the modal-expansion procedure, the governing PDDE is converted into a nonlinear DDE. The fixed points (zero and buckled equilibria) of the nonlinear DDE are found, and their linear stability is analyzed. Using Galerkin approximations, the characteristic roots (spectrum) of the DDE are found and reported in the parametric space of dimensionless flow velocity and axial load. The damping present in the stable region of the parametric space is obtained from the real part of the rightmost characteristic roots. The MMS is used to investigate the behavior of the system post instability. The purpose of this study is to assess the implication of the post-instability behavior on fatigue life calculations. Furthermore, for a given flow velocity, axial load can be tuned from the stability chart for achieving

maximum damping. Finally, **Chapter 5** summarizes the important inferences and the contribution of this PhD dissertation.

## Chapter 2

# An Investigation of Damping in Heat-Exchanger Tubes

### 2.1 Introduction

In this chapter, contour plots showing the damping in the parametric space of mass-damping parameter ( $m\delta$ ) and reduced flow-velocity ( $U = \tilde{U}/fD$ ) are reported for different values of the flow-retardation parameter ( $\mu$ ) and a normal-triangular array of cylinders. In all the earlier studies, only the stability boundaries in the parametric space have been reported, due to the complexity in solving the infinite-dimensional nonlinear eigenvalue problem associated with characteristic roots of the governing DDE. In this chapter, using Galerkin approximations, the spectrum (characteristic roots) of the DDE is obtained. The rightmost characteristic root, whose real part represents the damping in the heat-exchanger tube is included in the stability chart. The stability charts for different values of  $\mu$  can be used to determine the optimal cross-flow velocities for operating the heat-exchanger tube while achieving maximum damping.

### 2.2 Quasi-steady model of Price and Paidoussis

Several studies [29–32, 37] on cross-flow induced instability of cylinder rows are based on the quasi-steady mathematical model developed by Price and Paidoussis [4]. Since this theoretical model has been used so extensively, we have re-derived the equation of motion. Price and Paidoussis [4] arrived at an expression that facilitates obtaining the fluid forces on a flexible cylinder, numerically. Two geometries were considered,

as seen in Fig. 2.1. Geometry I (Fig. 2.1(a)) denotes a double row of flexible cylinders in a triangular configuration. Here,  $L_s/D = 0.688$  and  $T_a/D = 1.191$ , where  $L_s$  is the streamwise distance between two rows of cylinders and  $2T_a$  is the distance between two adjacent cylinders in the same row. Geometry II denotes a double row of flexible cylinders within an array of rigid cylinders in a rotated equilateral triangular configuration. Here,  $L_s/D$  and  $T_a/D$  are the same as for Geometry I, and  $P/D = 1.375$  for Geometry II, where  $P$  is the cylinder pitch.

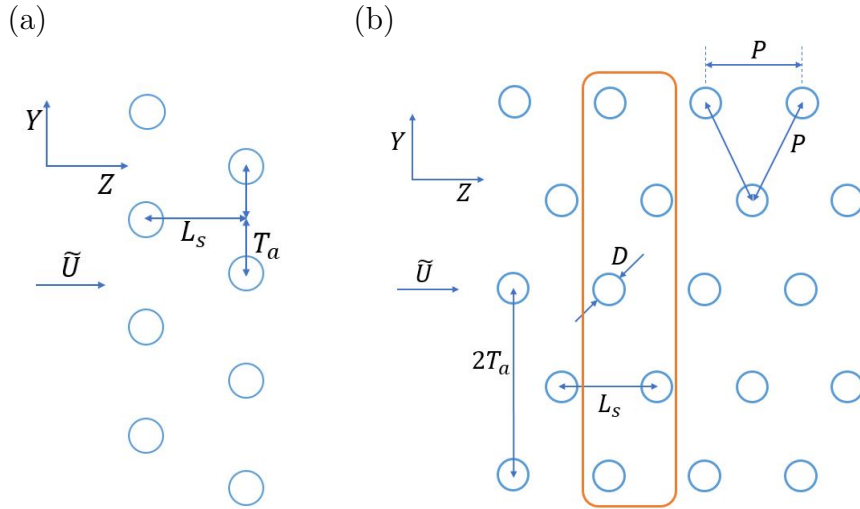


FIGURE 2.1: Schematic of the two geometries as used in Price and Paidoussis [4]. (a) Geometry I: a double row of flexible cylinders ( $L_s/D = 0.688$ ,  $T_a/D = 1.191$ ) (b) Geometry II: a double row of flexible cylinders within an array of rigid cylinders ( $L_s/D = 0.688$ ,  $T_a/D = 1.191$ ,  $P/D = 1.375$ ). Orange box encloses the double row of flexible cylinders. Figures are not to scale.

As shown in Fig. 2.2(a) the flow approaches upstream cylinders  $i - 1$  and  $i + 1$  with the free-stream velocity ( $\tilde{U}$ ) and downstream cylinder  $i$  with gap velocity ( $\tilde{U}_G$ ). Mass-conservation dictates that  $\tilde{U}_G(2T_a - D) = \tilde{U}(2T_a)$ . This can be written as

$$\tilde{U}_G = a\tilde{U}, \quad a = \frac{T_a}{T_a - D/2} \quad (2.1)$$

In general, it is expected that the fluid forces on cylinder  $i$  are influenced by the motion of the cylinders adjacent to it, i.e.  $i + 1$  and  $i - 1$ , for this geometry. However, since we are considering a single flexible cylinder within an array of rigid cylinders as explained in Section 1.4, only the motion of a downstream cylinder is analyzed, and it is assumed that cylinders  $i + 1$  and  $i - 1$  are rigid.

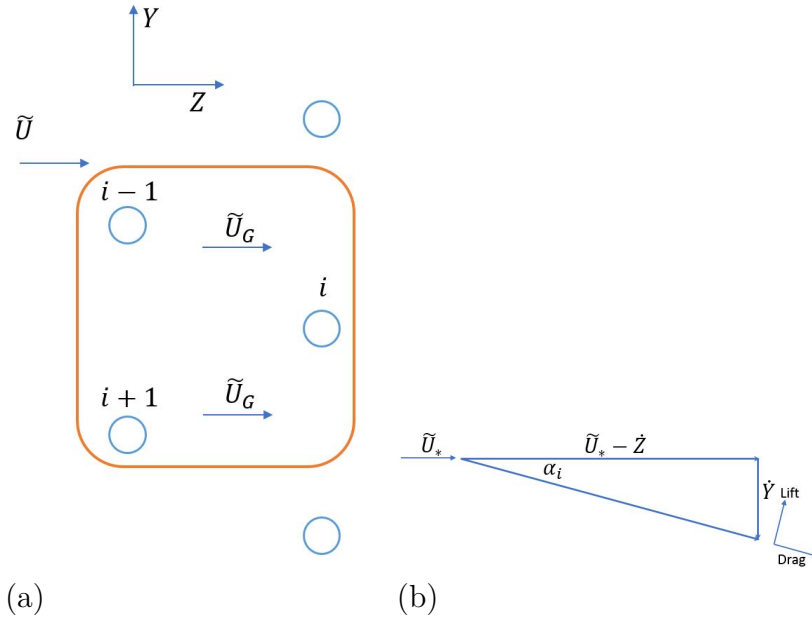


FIGURE 2.2: Schematic of a double row of flexible cylinders with (a) the cylinder numbering. (b) The velocity vector diagram for flow approaching a flexible cylinder.

### 2.2.1 Time Delay due to Flow Retardation

The apparent time taken by the flow to traverse the streamwise distance from  $-Z_1$  to  $-R - \Delta R$  is given by  $T = (Z_1 - R - \Delta R)/\tilde{U}_*$ , where  $\tilde{U}_* = \tilde{U}$  for an upstream cylinder,  $R$  is the radius of the cylinder, and  $Z = -Z_1$  is a point in the free-stream. Considering that the flow decelerates as it approaches the cylinder, the actual time taken ( $T + \Delta T$ ) will be given by

$$T + \Delta T = \int_{-Z_1}^{-R-\Delta R} \frac{1}{\tilde{U}_a} dZ, \quad (2.2)$$

where  $\tilde{U}_a$  is the approach speed. According to potential flow theory, the potential function ( $\phi_Z$ ) and speed  $\partial\phi_Z/\partial Z$  for flow approaching a cylinder along the  $Z$  axis is given by

$$\phi_Z = \tilde{U}_* \left( Z + \frac{R^2}{Z} \right), \quad \frac{\partial\phi_Z}{\partial Z} = \tilde{U}_* \left( 1 - \frac{R^2}{Z^2} \right) \quad (2.3)$$

Substituting Eq. (2.3) in Eq. (2.2), and integrating w.r.t.  $Z$ , we obtain

$$\begin{aligned} T + \Delta T &= \frac{1}{\tilde{U}_*} \int_{-Z_1}^{-R-\Delta R} \left( 1 + \frac{R^2}{Z^2 - R^2} \right) dZ \\ &= \frac{1}{\tilde{U}_*} \int_{-Z_1}^{-R-\Delta R} \left( 1 + \frac{R}{2} \left[ \frac{1}{Z - R} - \frac{1}{Z + R} \right] \right) dZ \\ &= \frac{Z_1 - R - \Delta R}{\tilde{U}_*} + \frac{R}{2\tilde{U}_*} \ln \left( \frac{2R + \Delta R}{\Delta R} \frac{Z_1 - R}{Z_1 + R} \right) \end{aligned} \quad (2.4a)$$

If we choose  $Z_1 \gg R > \Delta R$ , and substitute  $D = 2R$ , where  $D$  is the diameter of a cylinder tube, we get

$$\Delta T = \frac{D}{4U} \ln \left( \frac{2R + \Delta R}{\Delta R} \right) = \mu \frac{D}{\tilde{U}_*}, \quad (2.5)$$

where  $\mu$  is the time-delay parameter that was first introduced in Section 1.5. If we choose  $\Delta R = 0.1R$ ,  $\mu \approx 0.75$ , while for  $\Delta R = 0.01R$ ,  $\mu \approx 1.32$ . Hence, we can safely assume that  $\mu$  is of  $O(1)$ . Later, we discover that the choice of  $\mu$  changes the stability threshold by very high percentages, which makes it important to pick an accurate value for  $\mu$ . Typically, we choose  $\mu = 1$ .

Next, we assume a solution of the form  $Y(T) = Y_0(T)e^{\tilde{\lambda}T}$ , where  $\tilde{\lambda}(\in \mathbb{C})$  represents an eigenvalue, and  $T$  is time. The above analysis implies that at time  $T$ , the actual displacement of the cylinder in the lift direction is  $Y(T - \Delta T) = Y(T)e^{-\tilde{\lambda}\Delta T} = W(T)g_r$ , where  $g_r = e^{-\tilde{\lambda}\Delta T} = e^{-\mu\tilde{\lambda}\frac{D}{\tilde{U}_*}}$ . It must be noted that for an upstream cylinder,  $\tilde{U}_* = \tilde{U}$  and  $g_r$  can be designated as  $g_{r\infty} = e^{-\mu\tilde{\lambda}\frac{D}{\tilde{U}}}$ . For a downstream cylinder, Eq. (2.2) becomes

$$T + \Delta T = \frac{Z_1 - L_s}{\tilde{U}} + \int_{-L_s}^{-R-\Delta R} \frac{1}{\tilde{U}_a} dZ, \quad \tilde{U}_a = \tilde{U}_G \left( 1 - \frac{R^2}{Z^2} \right) \quad (2.6)$$

Simplifying Eq. (2.6) in the manner described above, we get

$$T + \Delta T = \frac{Z_1 - L_s}{\tilde{U}} + \frac{L_s - R - \Delta R}{\tilde{U}_G} + \frac{R}{2\tilde{U}_G} \ln \left( \frac{2R + \Delta R}{\Delta R} \frac{L_s - R}{L_s + R} \right) \quad (2.7)$$

This would mean that for a downstream cylinder,

$$\Delta T = \frac{R}{2\tilde{U}_G} \ln \left( \frac{2R + \Delta R}{\Delta R} \frac{L_s - R}{L_s + R} \right) \quad (2.8)$$

For  $\Delta R = 0.01R$  and  $L_s/D = 0.688$ , we find that  $\Delta T \approx 0.87 \frac{D}{\tilde{U}_G}$ . It would be reasonably safe to assume that for a downstream cylinder, i.e. for  $\tilde{U}_* = \tilde{U}_G$ ,  $g_r = g_{rd} = e^{-\mu\tilde{\lambda}\frac{D}{\tilde{U}_G}} = e^{-\mu\tilde{\lambda}\frac{D}{\tilde{U}_G}}$  with  $\mu = 1$ .

### 2.2.2 Fluid Forces on a Downstream Cylinder

As shown in Fig. 2.2(b), the flow approaches cylinder  $i$  at an angle of incidence ( $\alpha_i$ ), by virtue of its streamwise velocity ( $\dot{Z}_i$ ) and transverse velocity ( $\dot{Y}_i$ ). If  $D_F$  is the drag force,  $L_F$  the lift force on cylinder  $i$  in the directions as given by Fig. 2.2(b),  $L$  the tube length, and  $\tilde{U}_*$  the resultant approach velocity, the following expression for



the force in the transverse direction ( $F_{Y_i}$ ) can be obtained:

$$F_{Y_i} = L_F \cos \alpha_i - D_F \sin \alpha_i = \frac{1}{2} \rho \tilde{U}_*^2 LD \left[ \bar{C}_L \left( \frac{\tilde{U}_G - \dot{Z}_i}{\tilde{U}_*} \right) - \bar{C}_D \left( \frac{\dot{Y}_i}{\tilde{U}_*} \right) \right] \quad (2.9)$$

where,

$$\sin \alpha_i = \left( \frac{\dot{Y}_i}{\tilde{U}_*} \right), \quad \cos \alpha_i = \left( \frac{\tilde{U}_G - \dot{Z}_i}{\tilde{U}_*} \right), \quad (2.10)$$

$$\tilde{U}_* = \sqrt{(\tilde{U}_G - \dot{Z}_i)^2 + \dot{Y}_i^2} = \tilde{U}_G \sqrt{\left(1 - \frac{\dot{Z}_i}{\tilde{U}_G}\right)^2 + \left(\frac{\dot{Y}_i}{\tilde{U}_G}\right)^2} \approx \tilde{U}_G \left(1 - \frac{\dot{Z}_i}{\tilde{U}_G}\right). \quad (2.11)$$

$\bar{C}_D$  and  $\bar{C}_L$  are the drag and lift coefficients based on the gap velocity  $\tilde{U}_G$  for cylinder  $i$ . Equation (2.9) can be re-written as

$$\begin{aligned} F_{Y_i} &= \frac{1}{2} \rho LD \left[ \bar{C}_L \tilde{U}_* \tilde{U}_G \left(1 - \frac{\dot{Z}_i}{\tilde{U}_G}\right) - \bar{C}_D \tilde{U}_* \dot{Y}_i \right] = \\ &= \frac{1}{2} \rho LD \tilde{U}_G^2 \left[ \bar{C}_L \left(1 - \frac{\dot{Z}_i}{\tilde{U}_G}\right) - \bar{C}_D \left(1 - \frac{\dot{Z}_i}{\tilde{U}_G}\right) \frac{\dot{Y}_i}{\tilde{U}_G} \right], \end{aligned}$$

which upon further simplification and neglecting the second order terms, gives

$$F_{Y_i} \approx \frac{1}{2} \rho LD \tilde{U}_G^2 \left[ \bar{C}_L \left(1 - \frac{2\dot{Z}_i}{\tilde{U}_G}\right) - \bar{C}_D \left(\frac{\dot{Y}_i}{\tilde{U}_G}\right) \right] \quad (2.12)$$

Now,

$$F_D = \frac{1}{2} \rho LD \bar{C}_D \tilde{U}_G^2 = \frac{1}{2} \rho LDC_D \tilde{U}^2, \quad F_L = \frac{1}{2} \rho LD \bar{C}_L \tilde{U}_G^2 = \frac{1}{2} \rho LDC_L \tilde{U}^2 \quad (2.13)$$

where  $C_D$  and  $C_L$  are the drag and lift coefficients for cylinder  $i$ , associated with the far-stream velocity  $\tilde{U}$ . Substituting Eq. (2.13) in Eq. (2.12) and non-dimensionalizing, i.e. by defining  $z_i = Z_i/D$  and  $y_i = Y_i/D$ , we arrive at the following expressions:

$$F_{Y_i} = \frac{1}{2} \rho \tilde{U}^2 LD \left[ C_L \left(1 - \frac{2D}{a\tilde{U}} \dot{z}_i\right) - C_D \left(\frac{D}{a\tilde{U}} \dot{y}_i\right) \right] \quad (2.14)$$

Next, we have:

$$C_{L_i} = C_{L_{0i}} + z_i \frac{\partial C_{L_i}}{\partial z_i} + y_i \frac{\partial C_{L_i}}{\partial y_i} \quad (2.15a)$$

$$C_{D_i} = C_{D_{0i}} + z_i \frac{\partial C_{D_i}}{\partial z_i} + y_i \frac{\partial C_{D_i}}{\partial y_i} \quad (2.15b)$$

It can be inferred that  $C_{L_{0i}}$  corresponds to flow past a stationary cylinder, and due to the symmetric nature of such flow,  $C_{L_{0i}} = 0$ . Similarly, symmetry dictates that an infinitesimal displacement ( $dZ_i$ ) of the cylinder along the  $+/-Z$  axis should cause no change in the lift (which is along the  $Y$  axis), which gives us  $\partial C_{L_i}/\partial z_i = 0$ . Next, an infinitesimal displacement ( $dY_i$ ) of the cylinder along the  $+/-Y$  axis would cause an equal change in drag for either direction. This implies that  $\partial C_{D_i}/\partial y_i = -\partial C_{D_i}/\partial y_i = 0$ . Substituting Eqs. (2.15a) and (2.15b) in Eq. (2.14), and neglecting the  $\mathcal{O}(z_i \dot{z}_i, y_i \dot{y}_i, z_i \dot{y}_i, y_i \dot{z}_i)$  terms, we get:

$$F_{Y_i} = \frac{1}{2} \rho \tilde{U}^2 L D \left[ -C_{D_{0i}} \left( \frac{D}{a\tilde{U}} \right) \dot{y}_i + g_{rd} \frac{\partial C_{L_i}}{\partial y_i} y_i \right] \quad (2.16)$$

Here, we remember that the actual displacement of cylinder  $i$  is  $y_i(T - \Delta T) = g_{rd} y_i(T)$  (Section 2.2.1) and therefore replace  $y_i$  with  $g_{rd} y_i$ . With the understanding that we are focusing on a downstream cylinder, i.e. cylinder  $i$ , we will discard the subscript  $i$  for simplicity. Equation (2.16) can be written in a condensed form as follows:

$$F = \frac{1}{2} \rho \tilde{U}^2 L D \left[ \bar{\beta} \left( \frac{D}{a\tilde{U}} \right) \dot{y} + g_{rd} \bar{\kappa} y \right] \quad (2.17)$$

where  $\bar{\beta} = -C_{D_0}$ , and  $\bar{\kappa} = \partial C_L / \partial y$ . It must be noted that  $\dot{y}$  represents the derivative of the non-dimensional displacement ( $y$ ) w.r.t. the dimensional time ( $T$ ). Using  $t = \omega_n T$ , where  $\omega_n$  represents the undamped angular frequency of oscillation for the no-flow condition ( $\omega_n = 2\pi f$ ), and  $t$  represents the non-dimensional time, we get:

$$F = \frac{1}{2} \rho \tilde{U}^2 L D \left[ \bar{\beta} \left( \frac{D\omega_n}{a\tilde{U}} \right) \dot{y} + g_{rd} \bar{\kappa} y \right] \quad (2.18)$$

Here,  $\dot{y}$  now represents the derivative w.r.t non-dimensional time ( $dy/dt$ ).

## 2.3 Mathematical Model

Figure 2.3 shows a schematic of a single flexible cylinder in a rotated-equilateral array of rigid cylinders under cross-flow [4]. The equation of motion for a flexible cylinder in the lift ( $Y$ ) direction is given by:

$$ML \frac{d^2 Y}{dT^2} + C \frac{dY}{dT} + KY = \frac{1}{2} \rho \tilde{U}^2 L D \left[ \bar{\beta} \left( \frac{D\omega_n}{a\tilde{U}} \right) \dot{y} + g_{rd} \bar{\kappa} y \right] \quad (2.19)$$

Here,  $M$  is the mass of the tube per unit length,  $C$  is the modal damping coefficient, and  $K$  is the modal cylinder stiffness. Again, substituting  $y = Y/D$  and  $t = \omega_n T$  on

the LHS in Eq. (2.19), we get:

$$MLD\omega_n^2\ddot{y} + CD\omega_n\dot{y} + KDy = \frac{1}{2}\rho\tilde{U}^2LD\left[\bar{\beta}\left(\frac{D\omega_n}{a\tilde{U}}\right)\dot{y} + g_{rd}\bar{\kappa}y\right], \quad (2.20)$$

where  $g_{rd} = e^{-\tilde{\lambda}\mu D/aU_\infty}$  for a single flexible (downstream) cylinder in an array of rigid cylinders, and  $\tilde{\lambda}$  is an eigenvalue as mentioned in Section 2.2.1. Since  $\omega_n$  is the undamped radian frequency of oscillation for the no-flow condition, we have  $\omega_n = \sqrt{K/ML}$  [4]. Next, we use the well-known relation  $C/ML = 2\zeta\omega_n$ , where  $\zeta$  is the damping ratio. Furthermore, we know that  $\zeta \approx \delta/\pi$  for  $\delta \ll 1$ , where  $\delta$  is the logarithmic decrement. Dividing Eq. (2.20) by  $ML\omega_n^2$  throughout, and using  $C/ML\omega_n = \delta/\pi$ ,  $K/ML = \omega_n^2$  as outlined above, and  $U = \tilde{U}/D\omega_n$ , where  $U$  is the dimensionless flow velocity, we obtain

$$\ddot{y} + \left[\frac{\delta}{\pi} - \bar{\beta}\frac{U}{4\pi am}\right]\dot{y} + \left[1 - g_{rd}\bar{\kappa}\frac{U^2}{8\pi^2 m}\right]y = 0. \quad (2.21)$$

As done in Section 2.2.1,  $g_{rd}y$  can be recast as  $y(t)e^{-\tilde{\lambda}\mu D/aU_\infty} = y_0e^{\tilde{\lambda}t}e^{-\tilde{\lambda}\mu D/aU_\infty} = y(t - \tilde{\lambda}\mu D/aU_\infty)$ , and Eq. (2.21) can be written as a DDE by separating out the delay-dependent displacement term:

$$\ddot{y} + \dot{y}\left[\frac{\delta}{\pi} - \bar{\beta}\frac{U}{4\pi am}\right] + y - \bar{\kappa}\frac{U^2}{8\pi^2 m}y(t - \tau) = 0, \quad (2.22)$$

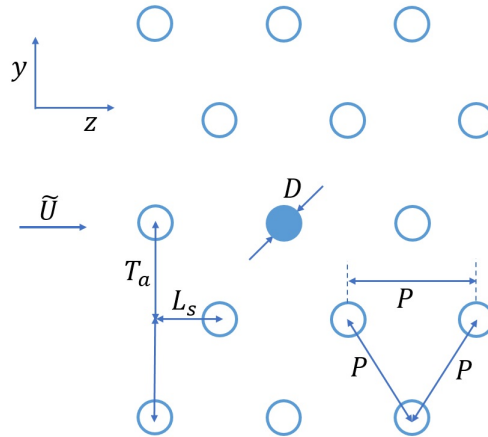


FIGURE 2.3: Schematic of a single flexible cylinder (solid blue color) in an array of rigid cylinders subject to cross-flow, as used in [4]. Figure not to scale.

where  $\tau = \mu\omega_n D/a\tilde{U} = \mu/aU$  is the dimensionless time-delay. The characteristic equation of Eq. (2.22) is given by

$$D(\lambda, U) = \lambda^2 + \lambda \left[ \frac{\delta}{\pi} - \bar{\beta} \frac{U}{4\pi am} \right] + 1 - \bar{\kappa} \frac{U^2}{8\pi^2 m} e^{-\lambda\tau} = 0, \quad (2.23)$$

Here,  $\lambda$  represents the roots of the characteristic equation and is dimensionless. It must be noted that the focus of the analysis by Price and Paidoussis [4] was obtaining only the stability *boundary*, which was accomplished by assuming  $\Re(\lambda) = 0$  in Eq. (2.23). This is reasonable since the characteristic roots must lie on the imaginary axis as the system transitions from stable to unstable. Hence,  $\lambda = i\omega_c$  is substituted in Eq. (2.23), where  $\omega_c = \Im(\lambda)$  at the stability threshold. The resulting expression was separated into its real and imaginary parts, which were each equated to zero, as follows:

$$\omega_c^2 - 1 + \frac{\bar{\kappa}U_c^2}{8\pi^2 m} \cos\left(\frac{2\pi\mu\omega_c}{aU_c}\right) = 0, \quad (2.24a)$$

$$\omega_c \left[ \frac{\delta}{\pi} - \frac{\bar{\beta}U_c}{4\pi am} \right] + \frac{\bar{\kappa}U_c^2}{8\pi m} \sin\left(\frac{2\pi\mu\omega_c}{aU_c}\right) = 0. \quad (2.24b)$$

Equations (2.24a) and (2.24b) constituted the characteristic equations, which were solved numerically to obtain  $U_c$  as a function of either  $m$  or  $\delta$ , i.e., the stability boundary, as it were. Note that the term “stability boundary” is more appropriately called the critical curve instead. We cannot definitively say that the critical curves *always* represent the stability boundary. The only conclusion we can draw is that a set of characteristic roots are purely imaginary along the critical curve. Let us consider an example. Equation (2.23) is transcendental and has infinitely many roots. Consider a case in which a set of characteristic roots lie on the imaginary axis, with another set of roots lying on the right half of the complex plane. The system would actually be *unstable* although there exists a pair of roots that lie on the imaginary axis, which satisfy Eqs. (2.24a) and (2.24b). These roots would lead us into believing that the system is at the stability boundary instead. In order to overcome this limitation, we solve for the roots of the characteristic equation (Eq. (2.23)) on the entire plane of  $[m\delta, U]$  in the following manner.

Equation (2.23) is a transcendental equation and has infinitely many roots. A large linear eigenvalue problem can be solved to compute the roots of Eq. (2.23). Although the procedure for converting a DDE into a system of ODEs for obtaining the characteristic roots has been reported in literature [49], a brief summary has been offered here for reference. Let  $\mathbf{y} = [y(t), \dot{y}(t)]^T$ . Substituting this in Eq. (2.22), we get

$$\dot{\mathbf{y}}(t) = \mathbf{A}\mathbf{y} + \mathbf{B}\mathbf{y}(t - \tau), \quad (2.25a)$$

$$\mathbf{A} = \begin{bmatrix} 0 & 1 \\ -1 & -\frac{\delta}{\pi} + \frac{\bar{\beta}U}{4\pi am} \end{bmatrix}, \quad \mathbf{B} = \begin{bmatrix} 0 & 0 \\ \frac{\bar{\kappa}U^2}{8\pi^2 m} & 0 \end{bmatrix}. \quad (2.25b)$$

Now, a shift-of-time transformation of the form  $\mathbf{y}(t+s) = \mathbf{z}(s, t)$  is introduced, where  $s \in [-\tau, 0]$ . Hence,  $\mathbf{y}(t) = \mathbf{z}(0, t)$  and  $\mathbf{y}(t - \tau) = \mathbf{z}(-\tau, t)$ . With the help of the chain rule for partial differentiation, we get

$$\frac{\partial \mathbf{z}(s, t)}{\partial t} = \frac{\partial \mathbf{y}(t+s)}{\partial(t+s)} \frac{\partial(t+s)}{\partial t} = \frac{\partial \mathbf{y}(t+s)}{\partial(t+s)} \quad (2.26a)$$

$$\frac{\partial \mathbf{z}(s, t)}{\partial s} = \frac{\partial \mathbf{y}(t+s)}{\partial(t+s)} \frac{\partial(t+s)}{\partial s} = \frac{\partial \mathbf{y}(t+s)}{\partial(t+s)}. \quad (2.26b)$$

Comparing Eqs. (2.26a) and (2.26b), we get:

$$\frac{\partial \mathbf{z}}{\partial t} = \frac{\partial \mathbf{z}}{\partial s}, \quad \forall \quad s \in [-\tau, 0]. \quad (2.27)$$

Furthermore,  $\mathbf{y}(t) = \mathbf{z}(0, t)$  and  $\mathbf{y}(t - \tau) = \mathbf{z}(-\tau, t)$ . Substituting the above relations in Eq. (2.25(a)), we obtain

$$\left. \frac{\partial \mathbf{z}}{\partial t} \right|_{s=0} = \mathbf{A}\mathbf{z}(0, t) + \mathbf{B}\mathbf{z}(-\tau, t). \quad (2.28)$$

Invoking a Galerkin approximation,  $\mathbf{z}$  is discretized as follows.

$$z_i(s, t) = \sum_{j=1}^N \phi_{ij}(s) r_{ij}(t) = \mathbf{\Phi}_i(s) \mathbf{r}_i(t); \quad i = 1, 2, \quad (2.29)$$

where  $\mathbf{\Phi}_i(s) = [\phi_{i1}(s), \phi_{i2}(s), \dots, \phi_{iN}(s)]^T$  and  $\mathbf{r}_i(t) = [r_{i1}(t), r_{i2}(t), \dots, r_{iN}(t)]^T$  are the basis functions and the independent coordinates, respectively. Eq. (2.29) can be written in vector form as

$$\mathbf{z}(s, t) = \mathbf{\Phi}^T(s) \boldsymbol{\chi}(t), \quad (2.30a)$$

$$\mathbf{\Phi} = \begin{bmatrix} \mathbf{\Phi}_1(s) & \mathbf{0} \\ \mathbf{0} & \mathbf{\Phi}_2(s) \end{bmatrix}, \quad \boldsymbol{\chi}(t) = \begin{bmatrix} \mathbf{r}_1(t) \\ \mathbf{r}_2(t) \end{bmatrix}, \quad (2.30b)$$

which upon substituting in Eq. (2.27), we get

$$\mathbf{\Phi}^T(s) \dot{\boldsymbol{\chi}}(t) = \mathbf{\Phi}'(s)^T \boldsymbol{\chi}(t), \quad (2.31)$$

where  $\Phi'(s) = \partial\Phi/\partial s$ . Premultiplying Eq. (2.31) by  $\Phi(s)$  and integrating with respect-to  $s$  over  $[-\tau, 0]$ , we get

$$\left(\int_{-\tau}^0 \Phi(s)\Phi^T(s)ds\right)\dot{\chi}(t) = \left(\int_{-\tau}^0 \Phi(s)\Phi'^T(s)ds\right)\chi(t) \quad (2.32a)$$

$$\Rightarrow \mathbf{C}\dot{\chi}(t) = \mathbf{D}\chi(t), \quad (2.32b)$$

where  $\mathbf{C}$  and  $\mathbf{D}$  are square, block-diagonal matrices of dimension  $2N$  each. We obtain the matrices on the boundary conditions as follows. From Eq. (2.30a) we have:

$$\left.\frac{\partial z}{\partial t}\right|_{s=0} = \Phi^T(s)\dot{\chi}(t) \quad (2.33a)$$

$$\mathbf{z}(0, t) = \Phi^T(0)\chi(t) \quad (2.33b)$$

$$\mathbf{z}(-\tau, t) = \Phi^T(-\tau)\chi(t). \quad (2.33c)$$

Substituting the above relations in Eq. (2.28), we get:

$$\Phi^T(0)\dot{\chi}(t) = [\mathbf{A}\Phi^T(0) + \mathbf{B}\Phi^T(-\tau)]\chi(t) \quad (2.34)$$

In Eq. (2.34), both  $\Phi^T(0)$  and  $[\mathbf{A}\Phi^T(0) + \mathbf{B}\Phi^T(-\tau)]$  are matrices of dimension  $2 \times 2N$ . These matrices contain information on the boundary conditions. Equations (2.32b) and (2.34) are combined by replacing the  $N$ th and  $2N$ th rows of matrices  $\mathbf{C}$  and  $\mathbf{D}$  (Eq. (2.32b)) with the first and second rows of  $\Phi^T(0)$  and  $[\mathbf{A}\Phi^T(0) + \mathbf{B}\Phi^T(-\tau)]$  (Eq. (2.34)), respectively. The equations obtained after combining the respective matrices are written as:

$$\mathbf{M}\dot{\chi}(t) = \mathbf{K}\chi(t), \quad (2.35a)$$

$$\Rightarrow \dot{\chi}(t) = \mathbf{M}^{-1}\mathbf{K}\chi(t), \quad (2.35b)$$

where  $\mathbf{M}$  and  $\mathbf{K}$  are both square matrices of dimensions  $2N$ . Hence, the DDE given by Eq. (2.22) has been approximated to a system of ODEs given by Eq. (2.35b). The basis functions used in this chapter are shifted Legendre polynomials given by

$$\phi_{i1}(s) = 1, \quad \phi_{i2}(s) = 1 + \frac{2s}{\tau}, \quad (2.36a)$$

$$\phi_{ik}(s) = \frac{(2k-3)\phi_{i2}(s)\phi_{ik-1}(s) - (k-2)\phi_{ik-2}(s)}{k-1}, \quad (2.36b)$$

$\forall k \in \{3, 4, \dots, N\}$  and  $i = 1, 2$ . More about this formulation and the entries of  $\mathbf{C}$  and  $\mathbf{D}$  can be found in ref. [49]. As  $N$  increases, approximately  $N/2$  eigenvalues of  $\mathbf{M}^{-1}\mathbf{K}$  converge to the characteristic roots, i.e., the roots of Eq. (2.23). It follows

from the above analysis that  $\mathbf{M}^{-1}\mathbf{K}$  is a function of the parameters  $m$ ,  $\delta$ , and  $U$ . The relevant aerodynamic force coefficients, stiffness and damping coefficients, and geometric parameters that inform the entries of  $\mathbf{M}^{-1}\mathbf{K}$  and the stability threshold are taken from [4] and summarized in Tab. 2.1. A grid with approximately  $10000 \times 9000$  points is constructed for the  $[m\delta, U]$  plane with  $m\delta \in [0.1, 10^3]$  and  $U \in [0.1, 10^2]$ . The eigenvalues ( $\bar{\lambda}$ ) of  $\mathbf{M}^{-1}\mathbf{K}$  are evaluated at each grid point. The system is considered to be stable at a particular grid point only if  $\Re(\bar{\lambda}) < 0, \forall \bar{\lambda}$  that satisfies Eq. (2.35b).

TABLE 2.1: Parametric values borrowed from Price and Paidoussis [4].

| Parameter | Value | Parameter                         | Value |
|-----------|-------|-----------------------------------|-------|
| $L_s/D$   | 0.688 | $C_{D0}$                          | 6.8   |
| $T_a/D$   | 1.191 | $\bar{\beta}$                     | -6.8  |
| $a$       | 1.724 | $\frac{\partial C_L}{\partial y}$ | -243  |
| $\delta$  | 0.1   | $\bar{\kappa}$                    | -243  |

## 2.4 Results

Since large values of  $N$  can result in increased computational overload, an optimal value of  $N$  that does not compromise on accuracy is first determined. In this study, the effect of different values of  $N$  ( $3 \leq N \leq 30$ ) required for obtaining eigenvalues that have converged to the characteristic roots is investigated. Residuals are obtained at each grid-point by substituting the rightmost eigenvalue ( $\bar{\lambda}_r$ ) in the characteristic equation (Eq. (2.23)). The eigenvalues of  $\mathbf{M}^{-1}\mathbf{K}$  are said to be converged if all residual values are less than  $10^{-6}$ . Since the minimum value of  $N$  required for convergence was found to be 30, all results presented here are for  $N = 30$ .

Before proceeding any further, it may be useful to obtain typical values of  $m\delta$  from data made available by the industry. Typical tube diameters and their thickness specifications have been reported by the Tubular Exchangers Manufacturers Association Inc. [53]. Typical tube material can be carbon steel, nickel-chromium alloys, admiralty brass, bronze and alloys of copper-nickel or nickel-chromium [53, 54]. The specific gravity of these materials can be found in [54]. The combined knowledge of this information and the specific gravity of heavy water, which is the typical secondary coolant in the heat exchangers of nuclear reactors, it can be argued that  $1 \leq m \leq 10$  is appropriate for industrial purposes. For  $\delta = 0.1$ , as is chosen for this

study,  $0.1 \leq m\delta \leq 1$ . Hence, lower values of  $m\delta$  are relevant to nuclear reactors. High  $m\delta$  are characteristic of gaseous flows [2].

### 2.4.1 Damping in the stable region

Figure 2.4(a) shows the stability chart for the system in the  $[m\delta, U]$  plane, for  $\mu = 1$ . The system is stable in the region of color. The stability threshold as reported by [4] is obtained by putting Eqs. (2.24a) and (2.24b) through a Newton-Raphson solver and plotted (red dots) for comparison with the current model. The following preliminary observations can be made. First, the stability boundary obtained from the Galerkin approximation gives a more conservative estimate of  $U_c$ , as compared to experiments (data from experiments was extracted from [4]). Secondly, it is in excellent agreement with the stability boundary obtained from the method used by [4]. The “critical curve” from [4] is therefore the stability boundary indeed. Third, alternating regions of negative and positive damping (unstable and stable regions, respectively) are found to exist for  $m\delta < 2$  (Fig. 2.4(b)). Such alternating regions were also reported by [4] (red dots in Fig. 2.4(b)).

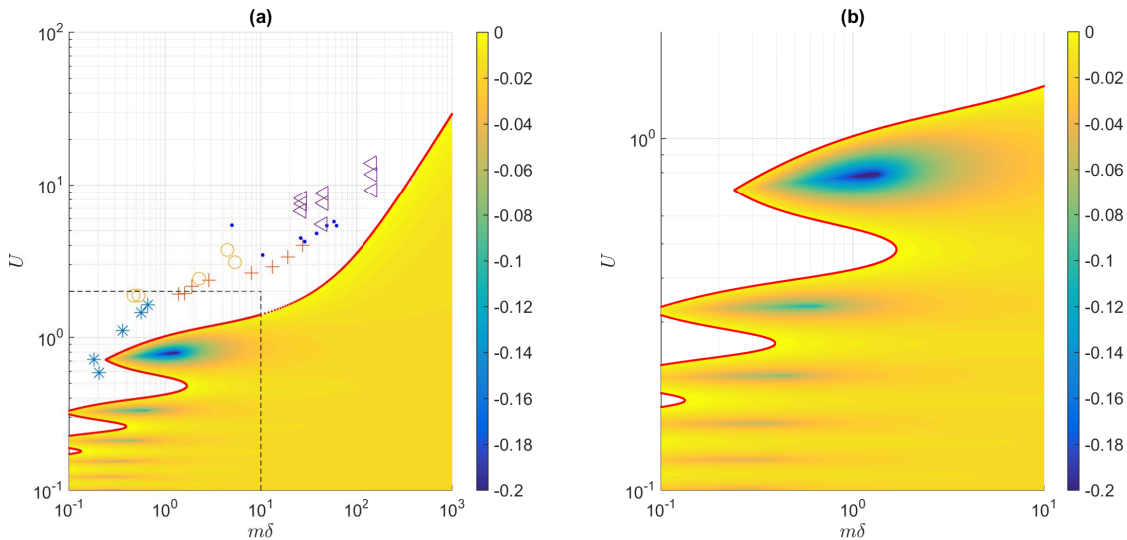


FIGURE 2.4: Stability chart obtained from the current model along with the stability threshold (red dots) from the model by [4], for  $\mu = 1$  in (a) the  $[m\delta, U]$  plane and (b) the low mass-damping parameter region demarcated by black dashed-lines in (a). Color map/contours indicate the damping (real part of the rightmost characteristic root). The white region represents the unstable region where the damping is not reported. Experimental data:  $\triangleleft$ , Hartlen [5];  $*$ , Heilker and Vincent [6];  $\circ$ , Pettigrew et al. [7];  $+$ , Weaver and Grover [8];  $\bullet$ , Weaver and El-Kashlan [9].



The most distinguishing result is the damping present in the stable region, represented by the color contours. These are obtained from the real part of the rightmost characteristic roots ( $\bar{\lambda}_r$ ) obtained from the current method. At high values of  $m\delta$ , i.e., for  $m\delta \geq 100$ , the damping is relatively low. An important feature of Fig. 2.4(a) is the region of maximum damping around  $m\delta = 1$  and  $U = 0.8$ . This region has been magnified in Fig. 2.4(b). More specifically, the highest damping in this region is found at  $m\delta = 1.333$ ,  $U = 0.791$ . The eigenvalues that have converged to the characteristic roots at this point are shown in Fig. 2.5. At this point,  $\Re(\lambda_r) \approx -0.2396$ , indicating that the peaks of the vibration response will decay at a rate proportional to  $e^{-0.2396t}$ . The region around this point is also a region of relatively low damping (Fig. 2.4(b)). This means that although  $(m\delta = 1, U = 0.4)$ , for instance, lies in a region of instability, it is more advisable for the system to operate at double the flow velocity ( $U = 0.8$ ) for the same value of mass-damping parameter. This challenges the notion that operating the system at lower values of  $U$  would guarantee a more stable system.

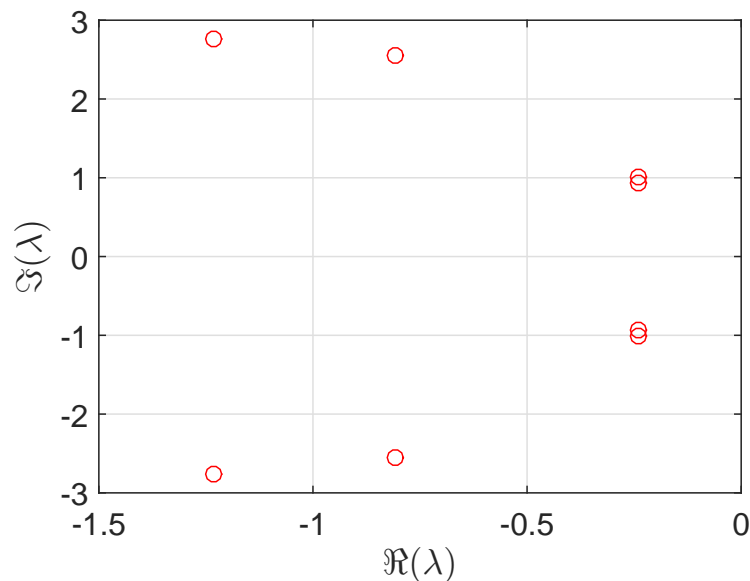


FIGURE 2.5: Characteristic roots at  $m\delta = 1.333$ , and  $U = 0.791$ , with the DDE given by  $\ddot{y} + 0.218\dot{y} + y + 1.444y(t - \tau) = 0$  as obtained from Eq. (2.22).

In order to obtain an understanding of how the stability behavior of the system changes with different values of the time-delay, stability charts are obtained for  $\mu = 2$  and  $\mu = 0.5$ . Figure 2.6(a) shows the stability chart for  $\mu = 2$ , along with the stability threshold (red dots) for  $\mu = 2$ , in the  $[m\delta, U]$  plane. Both sets of data are obtained from the current model. A comparison of Fig. 2.4(a) and Fig. 2.6(a)

shows that at  $m\delta = 1000$ ,  $U_c$  is approximately 100% smaller in magnitude than that for  $\mu = 1$ . Furthermore, there are twice as many regions of alternate negative and positive damping as those observed for  $\mu = 1$ . Figure 2.6(b) shows the stability chart for  $\mu = 0.5$ , along with the stability threshold (red dots) for  $\mu = 0.5$ , in the  $[m\delta, U]$  plane, with both sets of data obtained from the current model. A comparison of Fig. 2.4(a) and Fig. 2.6(a) shows that at  $m\delta = 1000$ ,  $U_c$  is approximately 100% larger in magnitude than that for  $\mu = 1$ . This corroborates well with the analysis by [4]. Only one region of alternating negative and positive damping is observed, reiterating the dependence of the damping-controlled instability on  $\mu$ . This suggests that the damping-controlled instability (the dominant instability for low  $m\delta$  [4]) is contingent on the flow-retardation parameter, and hence the dimensionless time-delay ( $\tau$ ). The shift in the region of maximum damping implies that the choice of  $\mu$  is important from an operational perspective and that the accepted convention of  $\mu = 1$  is questionable, from a practical point of view.

It must be noted that our analysis pertains to a non-dimensional parametric space. The advantage of using dimensionless parameters is that it gives us the flexibility of adjusting several dimensional physical quantities for a fixed value of the dimensionless parameter, with minimal computational overhead. Once the dimensionless parameters ( $m\delta$  and  $U$ ) are chosen, the engineer has a host of dimensional design parameters (tube material, thickness, and diameter) to adjust, in order to get the desired values of  $m\delta$  and  $U$ . In this manner, the system can be operated in a region of high damping.

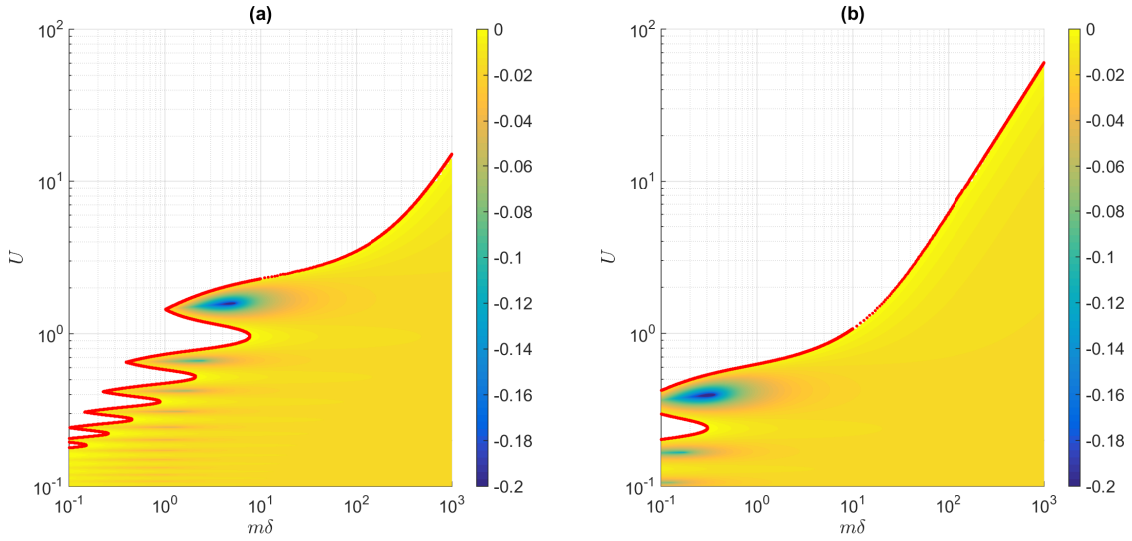


FIGURE 2.6: Comparison of the stability chart obtained from the current model (color map) and the stability threshold from [4] (red dots) for (a)  $\mu = 2$  (b)  $\mu = 0.5$ , in the  $[m\delta, U]$  plane. Color map/contours indicate the damping (real part of the rightmost characteristic root). The white region represents the unstable region where the damping is not reported.

## 2.4.2 Hopf bifurcation

It may be useful to understand the kind of bifurcation through which the system becomes unstable at the stability threshold. The occurrence of Hopf bifurcation can be investigated by observing the velocity at which the rightmost characteristic root ( $\lambda_r$ ) crosses the imaginary axis at the stability threshold. The velocity of root-crossing can be analytically obtained as follows. Differentiating Eq. (2.23) with respect to  $U$  and applying the chain rule, we get:

$$\frac{dD}{dU}(\lambda, U) = \frac{\partial D}{\partial U} + \frac{\partial D}{\partial \lambda} \frac{d\lambda}{dU} = 0, \quad (2.37a)$$

$$\Rightarrow \frac{d\lambda}{dU} = -\frac{\partial D / \partial U}{\partial D / \partial \lambda}. \quad (2.37b)$$

Substituting Eq. (2.23) in Eq. (2.37b), we get:

$$\frac{d\lambda}{dU} = \frac{\bar{\beta}\lambda\pi + \bar{\kappa}Uae^{-\frac{2\pi\lambda\mu}{aU}} + \bar{\kappa}\lambda\mu\pi e^{-\frac{2\pi\lambda\mu}{aU}}}{8a\pi^2m\lambda + 4a\pi m\delta - \pi\bar{\beta}U + \bar{\kappa}\mu\pi Ue^{-\frac{2\pi\lambda\mu}{aU}}}, \quad (2.38)$$

At the stability threshold,  $\Re(\lambda_r) = 0$ , so  $\lambda_r = i\omega_c$  is substituted in Eq. (2.38). Upon further simplification, and using  $e^{-i\theta} = \cos \theta - i \sin \theta$ , where  $\theta = \frac{2\pi\omega_c\mu}{aU}$ , we get:

$$\frac{d\lambda}{dU} = \frac{\frac{aU}{\pi} + \mu\omega_c \tan \theta + i \left( \frac{\bar{\beta}\omega_c}{\bar{\kappa} \cos \theta} - \frac{aU \tan \theta}{\pi} + \omega_c \mu \right)}{\mu U + \frac{4am\delta - \beta U}{\bar{\kappa} \cos \theta} + i \left( \frac{8a\pi m\omega_c}{\bar{\kappa} \cos \theta} - \mu U \tan \theta \right)}. \quad (2.39)$$

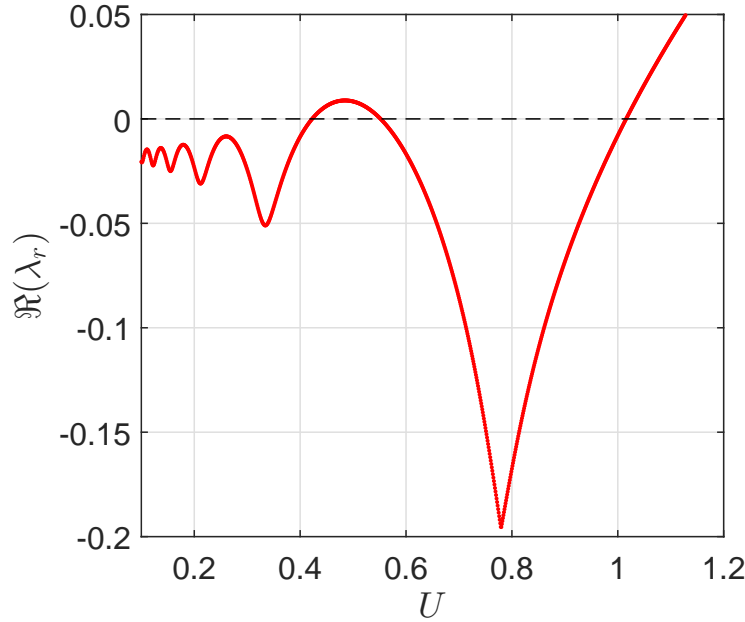


FIGURE 2.7: Variation of the real part of the rightmost characteristic roots with reduced velocity for  $m\delta = 1$ , in the vicinity of the critical points.

The real part of Eq. (2.39) gives the velocity of root-crossing at a point of interest on the stability threshold. For the sake of brevity, only the case of  $m\delta = 1$  has been considered to explore the possibility of Hopf bifurcation. Fig. 2.7 shows the variation of the real part of the rightmost root ( $\Re(\lambda_r)$ ) of the characteristic equation (Eq (2.23)), with  $U$ , for  $m\delta = 1$ . It can be seen that the plot of the  $\Re(\lambda_r)$  begins from  $\Re(\lambda_r) < 0$ , where the system is stable. The  $\Re(\lambda_r)$  then switches signs three times as the system transitions to the unstable region, back into the stable region and finally, back into the unstable region (This can be easily corroborated by traveling along the line  $m\delta = 1$  in Fig. 2.4(b)). The three points where  $\Re(\lambda_r) = 0$  are referred to as critical points. The dimensionless critical velocity ( $U_c$ ) and the imaginary part ( $\omega_c$ ) of  $\lambda_r$ , at these critical points, is shown in Tab. 2.2. By substituting these values of  $\omega_c$  into Eq. (2.39), the velocities at which the corresponding  $\lambda_r$  crosses the imaginary axis in the complex plane can be obtained analytically. These velocities can also be obtained, numerically, from evaluating the slope of the curve in Fig. 2.7 wherever it crosses the line  $\Re(\lambda_r) = 0$ .

The values obtained analytically ( $\bar{\Gamma}$ ) and numerically ( $\Gamma$ ) are compared in Tab. 2.2. These are within an error of less than 2% from each other, implying that  $\bar{\Gamma}$  and  $\Gamma$  are in reasonable agreement. Furthermore, since  $\bar{\Gamma}, \Gamma \neq 0$ , the three critical points under consideration are indeed Hopf bifurcation points. At  $U = 0.4230$ ,  $\bar{\Gamma}, \Gamma > 0$ , implying that the system is transitioning from stable to unstable. At  $U = 0.5520$ ,  $\bar{\Gamma}, \Gamma < 0$ , implying that the system is transitioning back from unstable to stable. At  $U = 1.016$ ,  $\bar{\Gamma}, \Gamma > 0$ , implying that the system is finally transitioning into an unstable region.

## 2.5 Chapter Summary

A stability analysis involving the second-order delay differential equation of motion from [4] is conducted for a single flexible cylinder in the parametric space of mass-damping parameter and reduced velocity. Galerkin approximations are used to model the equation. The stability boundary obtained from the current analysis is more conservative compared to data from experiments. However, it is in strong agreement with that obtained from the method used in [4]. This work goes beyond obtaining the stability threshold to report the damping present in the stable region of the  $[m\delta, U]$  plane, for  $\mu = 0.5, 1$ , and  $2$ . This is facilitated by the real parts of the rightmost characteristic roots obtained from the Galerkin method. Three important observations can be made from the information regarding damping:

1. At high mass-damping parameter ( $m\delta \geq 100$ ), the damping is relatively low.
2. Alternating regions of positive and negative damping are indeed found to exist for  $m\delta < 10$ , which corroborates observations from [4].
3. Finally, and most importantly, the region of the highest damping and therefore, maximum stability is found to exist around  $m\delta = 1.333$  and  $U = 0.791$ . The region of maximum damping is achieved at a comparatively lower mass-damping

TABLE 2.2: Velocity of root-crossing obtained numerically and analytically for the rightmost characteristic roots at the critical points, along  $m\delta = 1$ .

| $U$    | $\omega_c$ | $\Gamma$ | $\bar{\Gamma}$ |
|--------|------------|----------|----------------|
| 0.4230 | 0.9838     | 0.3047   | 0.3019         |
| 0.5520 | 1.0386     | -0.2528  | -0.2578        |
| 1.016  | 0.8288     | 0.4951   | 0.4947         |

parameter value for  $\mu = 0.5$ , and a comparatively higher mass-damping parameter value for  $\mu = 2$ .

The velocity of root-crossing is computed, numerically and analytically, at the three critical points for  $m\delta = 1$ . Since both methods provide non-zero values that are in strong agreement with each other, it is inferred that Hopf bifurcation occurs at the three critical points. Hopf bifurcation can also be proved to exist at other points on the stability threshold by deploying a similar analysis for different values of  $m\delta$ , indicating that the stability threshold is a locus of bifurcation points. The existence of Hopf bifurcation is important for the purpose of bifurcation control.

Much of the work presented in this chapter is new and very relevant to emerging studies on heat-exchanger tubes. Contrary to several earlier studies that have reported only the stability threshold, the information on the damping in the stable region has been reported here for the first time. Moreover, we report the region of maximum damping in the parametric space, where the vibration response of the tube will decay most rapidly. Remarkably, the mass-damping parameter in this region is low ( $m\delta < 10$ ). This is of prime importance from an operational point of view since nuclear reactors operate at low values of mass-damping parameter. Furthermore, popular opinion holds that it is safer to operate at a flow velocity lower than the lowest critical velocity for a given mass-damping parameter. However, the results in this chapter indicate that the region of maximum damping is a localized region in the parametric space, where the system is more stable at a higher velocity than the lowest critical velocity for that mass-damping parameter. This localized region is also close to the stability boundary. Since the region of maximum damping shifts with change in the flow-retardation parameter and hence the time-delay, the latter also bears significance if this region must be leveraged.

## Chapter 3

# Effect of Nonlinear Cladding Stiffness on the Stability and Hopf Bifurcation of a Heat-Exchanger Tube Subject to Cross-flow

### 3.1 Introduction

The linear stability of a heat-exchanger tube modeled as a single-span cantilever beam subjected to cross-flow has been studied with two parameters: (i) varying stiffness of the baffle-cladding at the free end and (ii) varying flow velocity. A mathematical model incorporating the motion-dependent fluid forces acting on the beam is developed using the Euler-Bernoulli beam theory, under the inextensible condition. The partial delay differential equation governing the dynamics of the continuous system is discretized to a set of finite, nonlinear delay differential equations through a Galerkin method in which a single mode is considered. Unstable regions in the parametric space of dimensionless cladding stiffness and flow velocity are identified, along with the magnitude of damping in the stable region. This information can be used to determine the cladding stiffness at which the system should be operated to achieve maximum damping at a known operational flow velocity. Furthermore, the system is found to lose stability by Hopf bifurcation and the method of multiple scales is used to analyze its post-instability behavior. Stable and unstable limit cycles are observed for different values of the linear component of the dimensionless cladding stiffness. A global bifurcation analysis indicates that the number of limit cycles decreases with increasing linear cladding stiffness. An optimal range for the linear cladding stiffness

is recommended where tube vibrations would either diminish to zero or assume a relatively low amplitude associated with a stable limit cycle.

This chapter is organized as follows. In Section 3.2, a detailed account of modeling the heat-exchanger tube as an Euler-Bernoulli cantilever beam is described. Fluid forces acting on the beam are modeled using an added-mass coefficient and aerodynamic parameters taken from the literature. Assuming a single dominant mode of vibration, the fixed points and the critical curves of the model are derived in Section 3.3. Section 3.3.1 establishes the base for the linear stability analysis. In Section 3.3.2, the procedure for approximating the delay differential equation (DDE) as a set of ordinary differential equations (ODEs) using Galerkin approximations is given. The stability chart for the system in the parametric space of dimensionless flow velocity and  $k_1$  is presented, along with the spectrum at the points of critical dimensionless cladding stiffness for a fixed value of dimensionless flow velocity. Section 3.4 establishes the presence of Hopf-bifurcation points. In Section 3.5, the method of multiple scales (MMS) is used to obtain the normal-form equations for both, the supercritical and subcritical Hopf-bifurcation points. Section 3.6 shows the global bifurcation diagram along with the limit cycles at selected values of  $k_1$ . Finally, Section 3.7 summarizes the contribution of this chapter.



### 3.2 Mathematical modeling

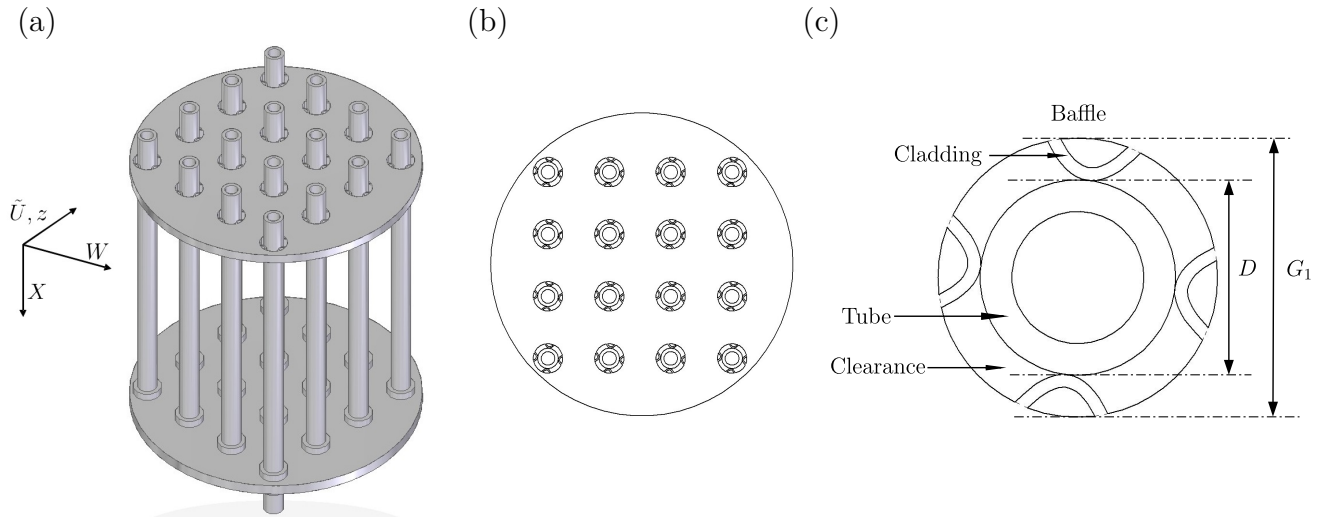


FIGURE 3.1: Schematic of (a) a section of a heat exchanger with tubes, baffle plates and claddings, with (b) a top view depicting the square array of tubes, (c) a cross-sectional view of a tube with claddings, where  $G_1$  is the baffle-hole diameter (figures not to scale).

The single-span flexible tube under consideration is modeled as an Euler-Bernoulli cantilever beam (Fig. 3.2) supported by a nonlinear spring that simulates the baffle-cladding at the free end (Fig. 3.1(c)).

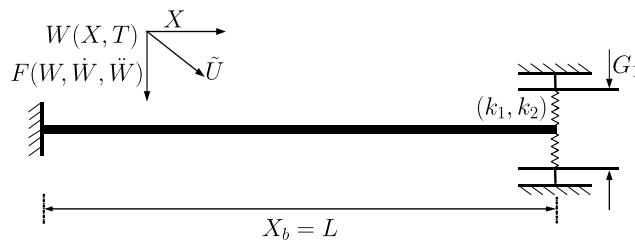


FIGURE 3.2: Schematic of a single flexible tube modeled as a cantilever beam (figure not to scale).

The tube axis is aligned in the  $X$  direction. Fluid with density  $\rho$  flows across the tube and along the  $z$  direction with a velocity of  $\tilde{U}$ . This flow produces a transverse deflection  $W$  of the tube. The equation that governs the motion of the tube when

modeled as an Euler-Bernoulli beam [30] is given by:

$$EI \frac{\partial^4 W}{\partial X^4} + C \frac{\partial W}{\partial T} + M \frac{\partial^2 W}{\partial T^2} + \delta(X - X_b) \tilde{f}(W) - \frac{EA}{2L} \frac{\partial^2 W}{\partial X^2} \int_0^L \left( \frac{\partial W}{\partial X} \right)^2 dX = F(W, \dot{W}, \ddot{W}), \quad (3.1)$$

where  $EI$  is the flexural rigidity,  $C$  is the damping coefficient, and  $M$  is the mass of the tube per unit length.  $A$  is the cross-sectional area of the cylindrical tube,  $X$  is the spatial coordinate, and  $T$  is time. The baffle and the support springs are located at a distance  $X_b = L$  from the fixed end. The force due to the support springs is represented by  $\tilde{f}$ , and  $\delta(X - X_b)$  is the Dirac delta function.  $F(W, \dot{W}, \ddot{W})$  is the cross-flow-induced force acting on the tube and is given by [37]:

$$F(W, \dot{W}, \ddot{W}) = -\frac{\pi}{4} \rho D^2 C_{ma} \frac{\partial^2 W(X, T)}{\partial T^2} - \frac{1}{2} \rho \tilde{U} D C_D \frac{\partial W(X, T)}{\partial T} + \frac{1}{2} \rho \tilde{U}^2 D \frac{\partial C_L}{\partial W} W(X, T - \Delta T). \quad (3.2)$$

$C_D$  and  $C_L$  are the drag and lift coefficients, respectively, which depend on the flow velocity in the gap between the tubes.  $C_{ma}$  is the added-mass coefficient of the fluid around the tube.  $\Delta T$  ( $= \mu D / \tilde{U}$ ) is the time-delay that arises due to the phase lag between cylinder motion and fluid dynamic forces, and  $\mu$  is a parameter related to tube-array pattern. In order to convert Eq. (3.1) into its non-dimensional form, the following dimensionless quantities are introduced:

$$w = \frac{W}{D}, \quad x = \frac{X}{L}, \quad t = \lambda_1^2 \sqrt{\frac{EI}{ML^4}} T = \Omega_1 T, \quad \xi = \frac{C}{\Omega_1 M}, \quad m = \frac{M}{\rho D^2}, \quad (3.3)$$

$$U = \frac{2\pi \tilde{U}}{D \Omega_1}, \quad \beta = \frac{1}{1 + \frac{4m}{\pi C_{ma}}}, \quad \gamma = \frac{AD^2}{2I \lambda_1^4}, \quad \text{and } f = \frac{\tilde{f}}{M \Omega_1^2 L D}.$$

Here,  $\lambda_1$  is the dimensionless eigenvalue of the first mode of the beam in the absence of nonlinear terms and fluid forces. On substituting the dimensionless parameters (Eq. (3.3)) into Eq. (3.1), we obtain:

$$\frac{1}{\lambda_1^4} \frac{\partial^4 w(x, t)}{\partial x^4} + \left( \xi + \frac{U C_D}{4\pi m} \right) \frac{\partial w(x, t)}{\partial t} + \frac{1}{1 - \beta} \frac{\partial^2 w(x, t)}{\partial t^2} + \delta(x - x_b) f(w(x, t)) - \gamma \frac{\partial^2 w(x, t)}{\partial x^2} \int_0^1 \left( \frac{\partial w(x, t)}{\partial x} \right)^2 dx - \frac{U^2}{8\pi^2 m} \frac{\partial C_L}{\partial w} w(x, t - \tau) = 0. \quad (3.4)$$

The dimensionless time-delay is given by  $\tau = 2\pi/U$  for  $\mu = 1$  [37]. The solution  $w(x, t)$  of Eq. (3.4) is approximated using a standard Galerkin expansion and by considering

only one dominant mode of vibration:

$$w(x, t) = \phi(x)q(t). \quad (3.5)$$

Here,  $\phi(x)$  is the shape function of a fixed-free beam of unit length, which is given by [39]:

$$\phi(x) = - \left( \frac{\cos \lambda_1 + \cosh \lambda_1}{\sin \lambda_1 + \sinh \lambda_1} \right) (\sinh \lambda_1 x - \sin \lambda_1 x) + (\cosh \lambda_1 x - \cos \lambda_1 x), \quad (3.6)$$

where  $\lambda_1 = 1.8751$  is the first dimensionless eigenvalue for the first mode [39]. We have considered a single mode for two of reasons. First, the critical velocity at which the tube becomes unstable is lowest for the first mode. Secondly, the multiple-scales analysis for obtaining normal forms (Section 3.5) becomes very complicated when higher modes are included. On substituting the approximated solution (Eq. (3.5)) into Eq. (3.4) and by defining  $\phi^I(x) = \frac{\partial \phi}{\partial x}$ ,  $\phi^{II}(x) = \frac{\partial^2 \phi}{\partial x^2}$  and  $\phi^{IV}(x) = \frac{\partial^4 \phi}{\partial x^4}$ , we get:

$$\begin{aligned} R(x, t) = & \frac{1}{1 - \beta} \phi(x) \ddot{q}(t) + \left( \xi + \frac{UC_D}{4\pi m} \right) \phi(x) \dot{q}(t) + \frac{1}{\lambda_1^4} \phi^{IV}(x) q(t) \\ & + \delta(x - x_b) f(w(x, t)) - \gamma \phi^{II}(x) q(t) \int_0^1 (\phi^I(x) q(t))^2 dx \\ & - \frac{U^2}{8\pi^2 m} \frac{\partial C_L}{\partial w} \phi(x) q(t - \tau). \end{aligned} \quad (3.7)$$

In Eq. (3.7),  $R(x, t)$  is the residue and error incurred in Eq. (3.1) from substituting the approximate solution given by Eq. (3.5). Using a Galerkin approximation, the weighted integrals of the residue are set to zero:

$$\int_0^1 R(x, t) \phi(x) dx = 0. \quad (3.8)$$

Upon substituting Eq. (3.7) into Eq. (3.8) and using the following expressions:

$$\int_0^1 \phi(x)^2 dx = 1, \quad (3.9a)$$

$$\int_0^1 \phi(x) \phi^{IV}(x) dx = \lambda_1^4, \quad (3.9b)$$

$$\int_0^1 \phi(x) \phi^{II}(x) \int_0^1 \phi^I(x)^2 dx = \bar{\mu} = 3.9887, \quad (3.9c)$$

$$\int_0^1 \phi(x) f(w(x_b)) \delta(x - x_b) dx = \phi(x_b) f(w(x_b)), \quad (3.9d)$$

we get the DDE

$$\begin{aligned} \ddot{q}(t) + (1 - \beta) \left( \frac{\delta_1}{\pi} + \frac{UC_D}{4\pi m} \right) \dot{q}(t) + (1 - \beta) q(t) - \gamma (1 - \beta) \bar{\mu} q^3(t) \\ - \frac{U^2}{8\pi^2 m} \frac{\partial C_L}{\partial w} (1 - \beta) q(t - \tau) + \phi(x_b) f(w(x_b)) (1 - \beta) = 0. \end{aligned} \quad (3.10)$$

In Eq. (3.10), damping ratio ( $\xi$ ) has been replaced by the modal damping ( $\delta_1/\pi$ ),  $\delta_1$  being the logarithmic decrement. For a square array with pitch-to-diameter ratio ( $P/D$ ) of 1.5, the values of the parameters in Eq. (3.10) are  $\beta = 0.24$ ,  $\delta_1 = 0.06$ ,  $C_D = 0.26$ ,  $m = 3$ ,  $\partial C_L/\partial w = -8.1$ , and  $\gamma = 0.015$  [40]. In this chapter, the dimensionless restraining spring force ( $f$ ) is chosen to be a combination of a linear spring and a cubic spring with dimensionless stiffness  $k_1$  and  $k_2$ , respectively. Therefore,

$$f(w(x_b)) = k_1 w(x_b) + k_2 w^3(x_b), \quad (3.11a)$$

$$k_1 = \frac{K_1 L^4}{\lambda_1^4 EID}, \quad k_2 = \frac{K_2 L^6}{\lambda_1^4 EID}, \quad (3.11b)$$

where  $K_1$  is the linear spring stiffness and  $K_2$  is the cubic spring stiffness. We have incorporated a cubic nonlinearity in addition to linear stiffness in the cladding force to account for large deformation at the cladding. It can be seen from Eq. (3.11a) that for small  $|w|$ , the contribution from the nonlinear term is very low, i.e., the spring will behave predominantly like a linear spring. However, when the amplitudes are large, the nonlinear stiffness contributes significantly to the force. Therefore, a combination of a linear and a cubic spring has been used in this study. Next, we introduce the following parameters

$$\alpha_1 = \frac{\delta_1}{\pi} (1 - \beta), \quad (3.12a)$$

$$\alpha_2 = \frac{C_D}{4\pi m} (1 - \beta), \quad (3.12b)$$

$$\alpha_3 = (1 - \beta), \quad (3.12c)$$

$$\alpha_4 = -\gamma \bar{\mu} (1 - \beta), \quad (3.12d)$$

$$\alpha_5 = -\frac{1}{8\pi^2 m} \frac{\partial C_L}{\partial w} (1 - \beta), \quad (3.12e)$$

$$\alpha_6 = \phi_1(x_b)^2 (1 - \beta), \quad (3.12f)$$

$$\alpha_7 = \phi_1(x_b)^4 (1 - \beta). \quad (3.12g)$$

The values of  $\alpha_6$  and  $\alpha_7$  can be obtained by substituting  $x_b = 1$ , as would be the case for support springs at the free end of the cantilever. The expressions and values for  $\alpha_1$  to  $\alpha_7$  have been summarized in Table 3.1 for reference.

TABLE 3.1: Values of nondimensional parameters  $\alpha_1$  to  $\alpha_7$  used in the nonlinear DDE given by Eq. (3.13).

| Parameter  | Expression  | Value   |
|------------|---|---------|
| $\alpha_1$ | $\delta_1 (1 - \beta) / \pi$                              | 0.0145  |
| $\alpha_2$ | $C_D (1 - \beta) / 4\pi m$                                | 0.0052  |
| $\alpha_3$ | $(1 - \beta)$   | 0.76    |
| $\alpha_4$ | $-\gamma \bar{\mu} (1 - \beta)$                           | -0.0098 |
| $\alpha_5$ | $-\frac{\partial C_L}{\partial w} (1 - \beta) / 8\pi^2 m$ | 0.026   |
| $\alpha_6$ | $\phi(x_b)^2 (1 - \beta)$                                 | 3.04    |
| $\alpha_7$ | $\phi(x_b)^4 (1 - \beta)$                                 | 12.1599 |

Equation (3.10) becomes:

$$\ddot{q}(t) + (\alpha_1 + U\alpha_2) \dot{q}(t) + (\alpha_3 + k_1\alpha_6) q(t) + (\alpha_4 + k_2\alpha_7) q^3(t) + U^2\alpha_5 q(t - \tau) = 0. \quad (3.13)$$

In the analysis that follows, care must be taken to choose values of  $k_1$  ( $K_1$ ) and  $k_2$  ( $K_2$ ) that are not too small. The effective linear stiffness coefficient in Eq. (3.13) above is the coefficient of the displacement term, i.e.,  $(\alpha_3 + k_1\alpha_6)$ . Substituting for  $\alpha_3$  and  $\alpha_6$ , the effective linear stiffness coefficient becomes  $(0.76 + 3.04k_1)$ . Here, the number 0.76 represents the nondimensional stiffness of the beam and the term  $3.04k_1$  represents the nondimensional linear stiffness of the baffle spring. For the linear stability and bifurcation analyses in this study, we have varied  $k_1$  from 0 to 100, thereby effectively varying  $3.04k_1$  from 0 to 304. Therefore, we have varied the linear cladding stiffness term up to 400 times the beam stiffness (0.76). Similarly, the nonlinear nondimensional stiffness coefficient due to cladding is given by  $\alpha_7 k_2$ . For  $k_2 = 50$  and  $\alpha_7 = 12.16$ ,  $\alpha_7 k_2 = 608$ , which is very high compared to the linear stiffness of the beam ( $\alpha_3 = 0.76$ ). Therefore, the values of  $k_1$  ( $K_1$ ) and  $k_2$  ( $K_2$ ) considered in this chapter are not small (relatively speaking).

### 3.3 Stability and bifurcation analysis

The equilibrium points for the system are first determined via a linear stability analysis. The stability and bifurcation analysis of the tube under varying dimensionless flow velocity and linear spring stiffness is then carried out.

#### 3.3.1 Linear stability

In this section, the fixed points of Eq. (3.13) are determined and their linear stability is analyzed. To determine the fixed points, we substitute  $q(t) = q(t - \tau) = \bar{q}$  in Eq. (3.13), and on further dropping the rate-dependent terms at the fixed points, we obtain:

$$(\alpha_3 + k_1\alpha_6)\bar{q} + \alpha_4\bar{q}^3 + k_2\alpha_7\bar{q}^3 + U^2\alpha_5\bar{q} = 0. \quad (3.14)$$

Solving for  $\bar{q}$  in Eq. (3.14), we get:

$$\bar{q}_1 = 0 \text{ and } \bar{q}_2 = \pm \sqrt{\frac{-(\alpha_3 + k_1\alpha_6) - U^2\alpha_5}{(\alpha_4 + k_2\alpha_7)}}. \quad (3.15)$$

In order to study the stability of the system at (around) the fixed points, we substitute  $q(t) = r(t) + \bar{q}$  in Eq. (3.13), which results in

$$\begin{aligned} \ddot{r}(t) + (\alpha_1 + U\alpha_2)\dot{r}(t) + (\alpha_3 + k_1\alpha_6)(r(t) + \bar{q}) + (\alpha_4 + k_2\alpha_7)(r(t) + \bar{q})^3 \\ + U^2\alpha_5(r(t - \tau) + \bar{q}) = 0. \end{aligned} \quad (3.16)$$

From Eq. (3.15) it is clear that equilibrium at the fixed point  $\bar{q}_2$  exists only for  $k_2 < -\frac{\alpha_4}{\alpha_7} = 8 \times 10^{-4}$ , which means the value of  $k_2$  must be unreasonably low and is therefore impractical. Hence, only zero equilibrium is studied in this chapter. Upon substituting  $\bar{q} = 0$  in Eq. (3.16), the following equation is obtained:

$$\ddot{r}(t) + (\alpha_1 + U\alpha_2)\dot{r}(t) + (\alpha_3 + k_1\alpha_6)r(t) + (\alpha_4 + k_2\alpha_7)r^3(t) + U^2\alpha_5r(t - \tau) = 0. \quad (3.17)$$

The stability of Eq. (3.17) depends on the roots of its characteristic equation. The linearized zero equilibrium of the system, after removing the nonlinear terms in  $r(t)$  from Eq. (3.17), is represented by:

$$\ddot{r}(t) + (\alpha_1 + U\alpha_2)\dot{r}(t) + (\alpha_3 + k_1\alpha_6)r(t) + U^2\alpha_5r(t - \tau) = 0. \quad (3.18)$$

The characteristic equation for Eq. (3.18) can be obtained by substituting  $r(t) = r_0 e^{\lambda t}$ :

$$\lambda^2 + (\alpha_1 + U\alpha_2)\lambda + (\alpha_3 + k_1\alpha_6) + U^2\alpha_5 e^{-\lambda\tau} = 0. \quad (3.19)$$

Equation (3.19) is a quasi-polynomial (due to the appearance of the  $e^{-\lambda\tau}$  term) and has infinitely many roots. If the real parts of all the characteristic roots of Eq. (3.19) are negative, then the equilibrium at  $\bar{q}$  is stable. It is generally not possible to obtain the roots of Eq. (3.19) in closed form. However, information regarding the critical curves that separate the stable and unstable regions in the  $[U, k_1]$  parametric space can be obtained. The stability of Eq. (3.17) around  $\bar{q}$  is lost when its rightmost characteristic roots cross the imaginary axis ( $\text{Real}(\lambda) = 0$ ). Therefore, in order to get the stability boundary, we substitute  $\lambda = j\omega_{cr}$  and  $k_1 = k_1^{cr}$  into Eq. (3.19). Next, using  $e^{-j\omega_{cr}\tau} = \cos(\omega_{cr}\tau) - j\sin(\omega_{cr}\tau)$ , and separating the real and imaginary parts of the resulting equation, the following nonlinear equations are obtained:

$$-\omega_{cr}^2 + \alpha_3 + k_1^{cr}\alpha_6 + U^2\alpha_5 \cos(\omega_{cr}\tau) = 0, \quad (3.20a)$$

$$(\alpha_1 + U\alpha_2)\omega_{cr} - U^2\alpha_5 \sin(\omega_{cr}\tau) = 0. \quad (3.20b)$$

For a given value of the critical dimensionless linear stiffness ( $k_1^{cr}$ ), Eqs. (3.20a) and (3.20b) can be solved numerically to determine the values of  $U$  and  $\omega_{cr}$  along the stability boundary. The stability boundary so obtained is shown by the critical curves 1 to 5 in Fig. 3.3. These curves divide the grid into 6 regions, viz. I to VI (see Fig. 3.3).

Note that the term “stability boundary” is a misnomer in this case. It cannot be definitively said that the critical curves always represent the stability boundary. The only deduction that can be drawn is that a set of characteristic roots are purely imaginary along each of the curves 1 – 5. A simple example that demonstrates this is a case where a set of characteristic roots lie on the imaginary axis, with another set lying on the right half of the complex plane, in which case the system is unstable. To counter this limitation, a Galerkin method is used to obtain information on the stability in each region (I – VI) and the amount of damping associated with the stable regions.

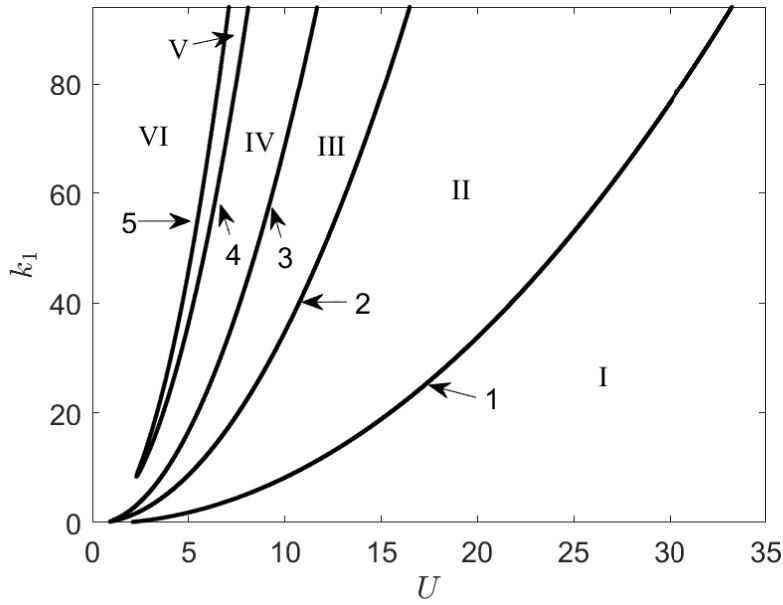


FIGURE 3.3: Critical curves for Hopf bifurcation for equilibrium point  $\bar{q}_1 = 0$ .

### 3.3.2 Spectrum

The detailed procedure for applying the Galerkin method to obtain the characteristic roots of the DDE is provided here. The DDE is converted into a set of finite-dimensional ODEs. The linearized zero equilibrium of the system (Eq. (3.17)) and the corresponding characteristic equation are rewritten here for reference:

$$\ddot{r}(t) + (\alpha_1 + U\alpha_2) \dot{r}(t) + (\alpha_3 + k_1\alpha_6) r(t) + U^2\alpha_5 r(t - \tau) = 0, \quad (3.21a)$$

$$\lambda^2 + (\alpha_1 + U\alpha_2) \lambda + (\alpha_3 + k_1\alpha_6) + U^2\alpha_5 e^{-\lambda\tau} = 0. \quad (3.21b)$$

Again, Eq. (3.21b) contains a transcendental term  $e^{-\lambda\tau}$  and has infinitely many roots. To determine the roots of Eq. (3.21b), a Galerkin approximation is used. In this method, the DDE is converted into a set of ODEs whose characteristic roots are approximately equal to those of the original DDE (Eq. (3.21a)). Although this procedure has been reported in the literature [49, 55] it is repeated here for completeness. The second-order DDE (Eq. (3.21a)) is first converted into two first-order DDEs by defining the following vector:

$$\mathbf{r}(t) = [r(t), \dot{r}(t)]^T. \quad (3.22)$$



Using Eq. (3.22), Eq. (3.21a) can be written as:

$$\dot{\mathbf{r}}(t) = \mathbf{A}\mathbf{r}(t) + \mathbf{B}\mathbf{r}(t - \tau). \quad (3.23)$$

We now introduce the time-shift transformation,  $\mathbf{r}(t + s) = \mathbf{y}(s, t)$ ,  $s \in [-\tau, 0]$ . The initial-value problem (Eq. (3.23)) is then converted into an initial-boundary value problem and Eq. (3.23) can be recast as:

$$\frac{\partial \mathbf{y}(s, t)}{\partial t} = \frac{\partial \mathbf{y}(s, t)}{\partial s}, \quad -\tau \leq s \leq 0. \quad (3.24)$$

$$\left. \frac{\partial \mathbf{y}(s, t)}{\partial t} \right|_{s=0} = \mathbf{A}\mathbf{y}(0, t) + \mathbf{B}\mathbf{y}(-\tau, t). \quad (3.25)$$

Now, we have converted the DDE (Eq. (3.21a)) into an equivalent PDE (Eq. (3.24)) with the boundary conditions given by Eq. (3.25). The solution of the PDE (Eq. (3.24)) is discretized using the following finite-series solution:

$$y_i(s, t) = \sum_{j=1}^N \psi_{ij}(s) z_{ij}(t) = \boldsymbol{\psi}_i(s)^T \mathbf{z}_i(t), \quad i = 1, 2. \quad (3.26)$$

Here,  $\boldsymbol{\psi}_i(s) = [\psi_{i1}(s), \psi_{i2}(s), \dots, \psi_{iN}(s)]^T$  are the basis functions, and  $\mathbf{z}_i(t) = [z_{i1}(t), z_{i2}(t), \dots, z_{iN}(t)]^T$ . Now, we define the matrix  $\boldsymbol{\Psi}(s) \in \mathbb{R}^{2N \times 2}$  and vector  $\mathbf{Z}(t) \in \mathbb{R}^{2N \times 1}$  as follows:

$$\boldsymbol{\Psi}(s) = \begin{bmatrix} \boldsymbol{\psi}_1(s) & \mathbf{0} \\ \mathbf{0} & \boldsymbol{\psi}_2(s) \end{bmatrix}, \quad \mathbf{Z}(t) = \begin{Bmatrix} \mathbf{z}_1(t) \\ \mathbf{z}_2(t) \end{Bmatrix}. \quad (3.27)$$

Using Eq. (3.27), Eq. (3.26) can be written in vector form as:

$$\mathbf{y}(s, t) = \boldsymbol{\Psi}^T(s) \mathbf{Z}(t). \quad (3.28)$$

Substituting Eq. (3.28) into Eq. (3.24), we get:

$$\boldsymbol{\Psi}^T(s) \dot{\mathbf{Z}}(t) = \boldsymbol{\Psi}'(s)^T \mathbf{Z}(t), \quad (3.29)$$

where  $\boldsymbol{\Psi}'(s)$  is the derivative of  $\boldsymbol{\Psi}(s)$  with respect to  $s$ . Premultiplying Eq. (3.29) by  $\boldsymbol{\Psi}(s)$  and integrating over the domain  $s \in [-\tau, 0]$ , we obtain:

$$\left( \int_{-\tau}^0 \boldsymbol{\Psi}(s) \boldsymbol{\Psi}^T(s) ds \right) \dot{\mathbf{Z}}(t) = \left( \int_{-\tau}^0 \boldsymbol{\Psi}(s) \boldsymbol{\Psi}'(s)^T ds \right) \mathbf{Z}(t). \quad (3.30)$$

Equation (3.30) can be rewritten in matrix form as:

$$\mathbf{C}\dot{\mathbf{Z}}(t) = \mathbf{D}\mathbf{Z}(t), \quad (3.31)$$

where  $\{\mathbf{C}, \mathbf{D}\} \in \mathbb{R}^{2N \times 2N}$  are block-diagonal matrices and are defined as:

$$\mathbf{C} \triangleq \int_{-\tau}^0 \boldsymbol{\Psi}(s)\boldsymbol{\Psi}^T(s)ds, \quad \mathbf{D} \triangleq \int_{-\tau}^0 \boldsymbol{\Psi}(s)\boldsymbol{\Psi}'(s)^T ds. \quad (3.32)$$

The boundary conditions for the system can be obtained by substituting Eq. (3.28) into Eq. (3.25):

$$\boldsymbol{\Psi}^T(0)\dot{\mathbf{Z}}(t) = [\mathbf{A}\boldsymbol{\Psi}^T(0) + \mathbf{B}\boldsymbol{\Psi}^T(-\tau)] \mathbf{Z}(t). \quad (3.33)$$

Equation (3.33) has two rows. The boundary conditions are incorporated into Eq. (3.31) by replacing the  $N^{th}$  and  $2N^{th}$  rows of Eq. (3.31) by the first and second rows of Eq. (3.33), respectively. The resulting equations can be written as:

$$\mathbf{M}\dot{\mathbf{Z}}(t) = \mathbf{K}\mathbf{Z}(t) \implies \dot{\mathbf{Z}}(t) = \mathbf{G}\mathbf{Z}(t), \quad (3.34)$$

where  $\mathbf{G} \triangleq \mathbf{M}^{-1}\mathbf{K}$ . Equation (3.34) represents an approximated system of ODEs for the DDE given Eq. (3.21a). As we increase the number of terms ( $N$ ) in the series solution given by Eq. (3.26), the eigenvalues of Eq. (3.34) converge to the characteristic roots of Eq. (3.21b). Therefore, the stability of the DDE given by Eq. (3.21a) can be studied by determining the eigenvalues of Eq. (3.34). Shifted Legendre polynomials are used as basis functions in Eq. (3.26), since the literature shows that they result in relatively faster convergence to the characteristic roots [49]. Figure 3.4 shows the stability chart for the system governed by Eq. (3.21a). The entire region of Fig. 3.4 has been discretized into  $500 \times 1000$  points. At each of these points, the eigenvalues of matrix  $\mathbf{G}$  (see Eq. (3.34)) are evaluated. If all the eigenvalues fall on the left side of complex plane, the system is considered to be stable; otherwise, it is considered unstable. Figure 3.4 clearly delineates the unstable regions from the stable ones, where the system can be safely operated. All the points in the white regions I, III, and V (Fig. 3.4) are unstable. The color contours indicate the damping present in the rightmost characteristic root, in the stable regions. The highest damping is present in the region around  $U = 23$  and  $k_1 = 90$ . The information regarding damping can be used to determine the linear cladding stiffness at which the system should be operated to achieve maximum damping at a known operational flow velocity. Figure 3.4 must be contrasted with Fig. 3.3 as the boundary curves shown in both the figures are the same.

Next, we study the distribution of the characteristic roots for different critical

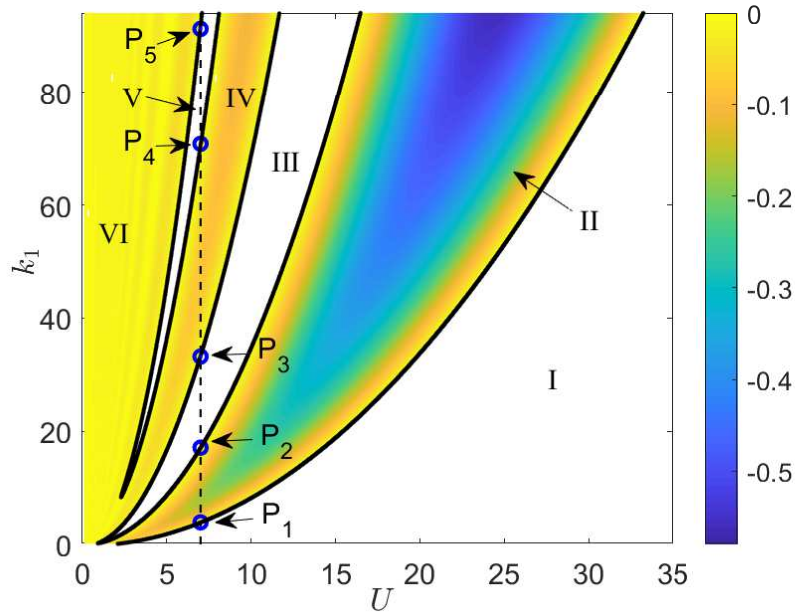


FIGURE 3.4: Stability chart in the  $[U, k_1]$  plane obtained from the Galerkin approximation, with color contours representing the damping present in the rightmost root.

points in Fig. 3.4 along  $U = 7$ , shown by the dashed vertical line in Fig. 3.4. Points  $P_1$  to  $P_5$  are the bifurcation points of zero equilibrium. The values of critical dimensionless linear stiffness ( $k_1^{cr}$ ) and frequency ( $\omega_{cr}$ ) at these points are shown in the second and third columns of Table 3.2, respectively.

Figure 3.5 shows the 12 rightmost characteristic roots of Eq. (3.21a), corresponding to the points  $P_1$  to  $P_5$ , which lie on the stability boundary. In all cases, it is clearly

TABLE 3.2: Values of  $k_1^{cr}$ ,  $\omega_{cr}$ ,  $\bar{\Gamma}$  (numerical),  $\Gamma$  (analytical), and relative error between the latter  $\hat{e} = \left(\frac{\bar{\Gamma}-\Gamma}{\Gamma}\right)$  expressed as a percentage, for points  $P_1$  to  $P_5$  indicated on the stability chart (see Fig. 3.4).

| Point | $k_1^{cr}$ | $\omega_{cr}$ | $\bar{\Gamma} (\times 10^{-4})$ | $\Gamma (\times 10^{-4})$ | $\hat{e} (\%)$ |
|-------|------------|---------------|---------------------------------|---------------------------|----------------|
| $P_1$ | 3.85       | 3.347         | -744                            | -745                      | 0.13           |
| $P_2$ | 17.05      | 7.335         | 140                             | 139                       | 0.72           |
| $P_3$ | 33.27      | 10.04         | -79                             | -75                       | 5.3            |
| $P_4$ | 70.55      | 14.71         | 29                              | 33                        | 12.1           |
| $P_5$ | 91.6       | 16.68         | -23                             | -25                       | 8.0            |

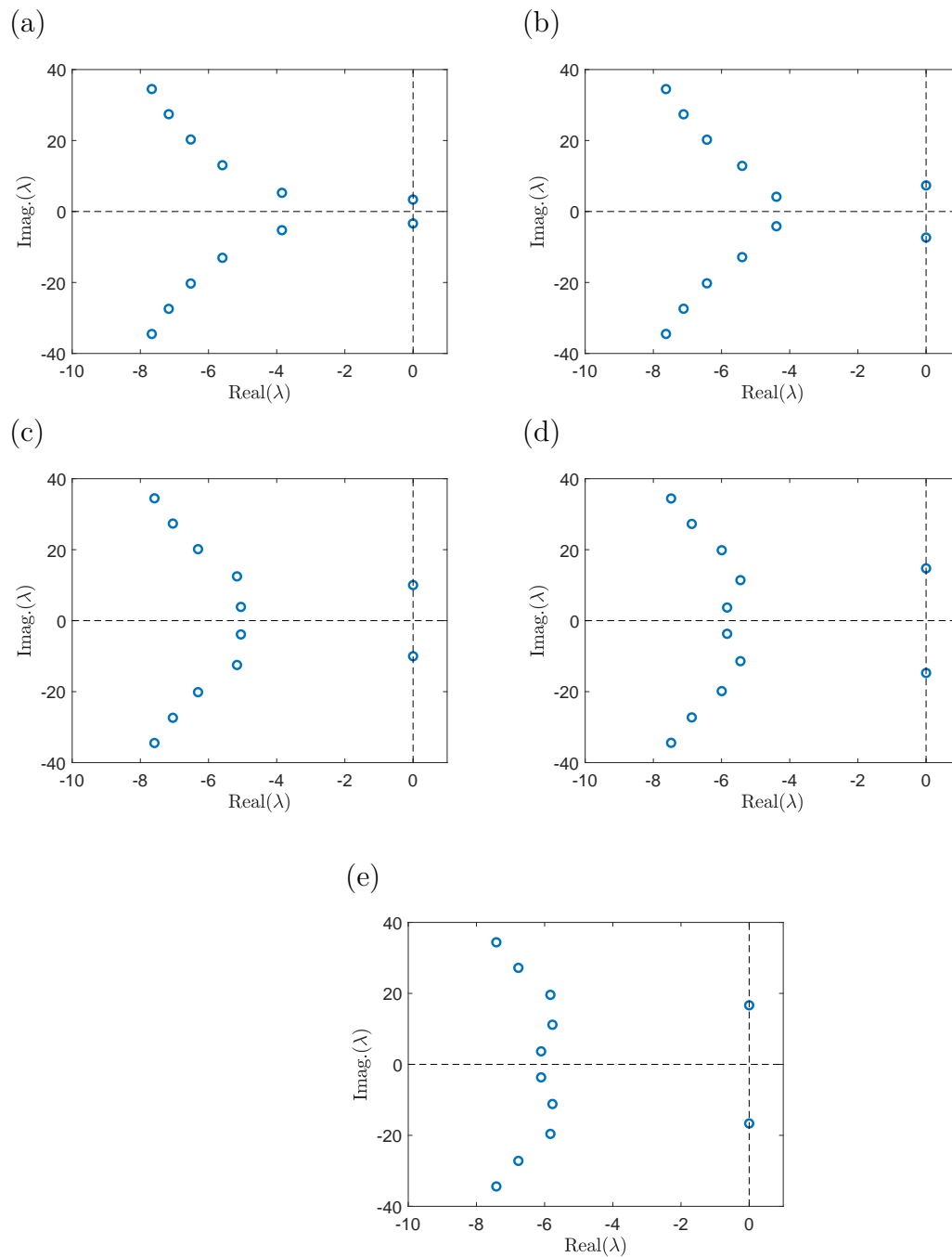


FIGURE 3.5: Characteristic roots of Eq. (3.21a) obtained using Galerkin approximations for  $U = 7$  and for (a)  $k_1 = 3.85$ , (b)  $k_1 = 17.05$ , (c)  $k_1 = 33.27$ , (d)  $k_1 = 70.55$ , and (e)  $k_1 = 91.6$ .

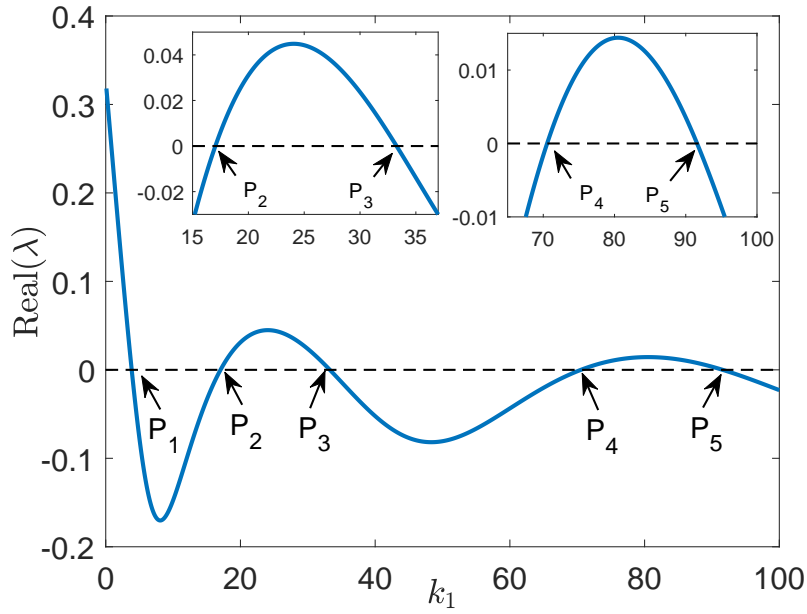


FIGURE 3.6: Variation of the real part of the rightmost characteristic root of Eq. (3.21a) for  $U = 7$  and for  $0 < k_1 \leq 100$ .

observed that the rightmost roots lie on the imaginary axis. This indicates the possibility of Hopf bifurcation, which is investigated in the next section.

### 3.4 Hopf bifurcation

The real part of the rightmost characteristic roots of Eq. (3.21a) along the line  $U = 7$  is plotted against the dimensionless linear stiffness ( $k_1$ ) in Fig. 3.6. To determine whether points  $P_1$  to  $P_5$  are those of Hopf bifurcation, the values of  $\bar{\Gamma}$  ( $= \text{Real} \left( \frac{d\lambda}{dk_1} \right) \Big|_{k_1=k_1^{cr}}$ ) at these points are obtained numerically.  $\bar{\Gamma}$  is approximated as  $\text{Real} \left( \frac{\lambda(k_1^{cr} + \delta k_1) - \lambda(k_1^{cr} - \delta k_1)}{2\delta k_1} \right)$ , where  $\delta k_1$  is the step size in Fig. 3.6. These are shown in the fourth column of Table 3.2. Here,  $\bar{\Gamma}$  represents the velocity at which the rightmost characteristic root crosses the imaginary axis, and is hence called the velocity of root-crossing. Figure 3.6 shows that the real part of the rightmost root crosses the imaginary axis at points  $P_1, P_2, P_3, P_4$  and  $P_5$  with a non-zero slope  $\bar{\Gamma}$  with respect to the parameter  $k_1$ . This clearly indicates the presence of a Hopf bifurcation at each of these points. We proceed to obtain the analytical values of the velocity of root-crossing for comparison. The following parameters are introduced into Eq. (3.17):

$$2\zeta = \alpha_1 + \alpha_2 U, \quad \vartheta = \alpha_5 U^2, \quad \kappa = \alpha_4 + k_2 \alpha_7, \quad \text{and} \quad \sigma = \alpha_3 + k_1 \alpha_6. \quad (3.35)$$

Hence, the zero equilibrium for the system (Eq. (3.17)) and its characteristic equation can be rewritten as:

$$\ddot{r}(t) + 2\zeta\dot{r}(t) + \sigma r(t) + \vartheta r(t - \tau) + \kappa r^3(t) = 0, \quad (3.36a)$$

$$D(\lambda, \sigma) = \lambda^2 + 2\zeta\lambda + \sigma + \frac{\vartheta}{e^{\lambda\tau}} = 0, \quad (3.36b)$$

where the nonlinear terms in  $r(t)$  have been dropped from Eq. (3.36a). Since  $\lambda$  is an implicit function of  $\sigma$ , from the chain rule of differentiation, we have:

$$dD(\lambda, \sigma) = \frac{\partial D}{\partial \lambda} d\lambda + \frac{\partial D}{\partial \sigma} d\sigma = 0, \quad (3.37a)$$

$$\frac{d\lambda}{d\sigma} = -\frac{\partial D}{\partial \sigma} / \frac{\partial D}{\partial \lambda} = -\frac{1}{2\lambda + 2\zeta - \frac{\vartheta\tau}{e^{\lambda\tau}}}. \quad (3.37b)$$

At a Hopf-bifurcation point,  $\text{Real}\left(\frac{d\lambda}{d\sigma}\Big|_{\sigma=\sigma_{cr}, \lambda=j\omega_{cr}}\right) \neq 0$ . Substituting  $\sigma = \sigma_{cr}$  and  $\lambda = j\omega_{cr}$  into Eq. (3.37b) and using the identity  $e^{-j\omega_{cr}\tau} = \cos(\omega_{cr}\tau) - j\sin(\omega_{cr}\tau)$ , we get:

$$\frac{d\lambda}{d\sigma}\Big|_{\sigma=\sigma_{cr}, \lambda=j\omega_{cr}} = \left(\frac{2\zeta - \cos(\omega_{cr}\tau)\vartheta\tau}{II}\right) - j\left(\frac{2\omega_{cr} + \sin(\omega_{cr}\tau)\vartheta\tau}{II}\right), \quad (3.38a)$$

$$II = -4(\omega_{cr}^2 + \zeta^2) - 4\omega_{cr}\vartheta\tau\sin(\omega_{cr}\tau) - \vartheta^2\tau^2 + 4\zeta\vartheta\tau\cos(\omega_{cr}\tau). \quad (3.38b)$$

From Eq. (3.35), we have  $\sigma = \alpha_3 + k_1\alpha_6$ , which gives  $d\sigma = \alpha_6 dk_1$ ; from the real part of Eq. (3.38a), we get:

$$\Gamma = \text{Real}\left(\frac{d\lambda}{dk_1}\right)\Big|_{k_1^{cr}, j\omega_{cr}} = \alpha_6 \left(\frac{2\zeta - \cos(\omega_{cr}\tau)\vartheta\tau}{II}\right). \quad (3.39)$$

From Eqs. (3.20a) and (3.20b), we have:

$$U^2\alpha_5\cos(\omega_{cr}\tau) = \vartheta\cos(\omega_{cr}\tau) = \omega_{cr}^2 - \alpha_3 - k_1^{cr}\alpha_6 \quad (3.40a)$$

$$U^2\alpha_5\sin(\omega_{cr}\tau) = \vartheta\sin(\omega_{cr}\tau) = 2\zeta\omega_{cr} \quad (3.40b)$$

Substituting for  $\vartheta\sin(\omega_{cr}\tau)$  and  $\vartheta\cos(\omega_{cr}\tau)$  into Eq. (3.38b), we get:

$$II = -4(\omega_{cr}^2 + \zeta^2) - \vartheta^2\tau^2 - 4\zeta\tau\omega_{cr}^2 - 4\zeta\tau\alpha_3 - 4\zeta\tau k_1^{cr}\alpha_6. \quad (3.41)$$

This gives

$$\Gamma = -\frac{\alpha_6(2\zeta - \tau\omega_{cr}^2 + \tau\alpha_3 + \tau k_1^{cr}\alpha_6)}{4\omega_{cr}^2 + 4\omega_{cr}^2\zeta\tau + 4\zeta^2 + 4\zeta\tau\alpha_3 + 4\zeta\tau k_1^{cr}\alpha_6 + \vartheta^2\tau^2}. \quad (3.42)$$

The value of  $\Gamma$  obtained from Eq. (3.42) is evaluated at the points  $P_1$  to  $P_5$  (see Fig. 3.4). These values are shown in Table 3.2. The table shows that the values of the velocity of root-crossing obtained from numerical approximations ( $\bar{\Gamma}$ ) are in close agreement with those predicted analytically ( $\Gamma$ ) for the points  $P_1$  to  $P_5$ . This corroborates the numerical procedure outlined above, which not only provides information on the damping present in the rightmost root in the stable region, but also regarding the presence of Hopf bifurcation at the stability boundary. Indeed, it can be also verified analytically, from Table 3.2, that  $\Gamma \neq 0$  at all the points  $P_1$  to  $P_5$ , which guarantees the presence of Hopf bifurcation.

Furthermore, it should be noted that at points  $P_2$  and  $P_4$ ,  $\Gamma > 0$  (Table 3.2) indicates that the rightmost roots are crossing from left to right in the complex plane, i.e., the system is transitioning from stable to unstable. Similarly, at points  $P_1$ ,  $P_3$  and  $P_5$ ,  $\Gamma < 0$ , which indicates the crossing of purely imaginary roots from right to left on the complex plane, i.e., the system is transitioning from unstable to stable. This can also be verified from Fig. 3.6.

### 3.5 Method of multiple scales

Since we are interested in studying the motions around the Hopf-bifurcation points, we perturb  $k_1^{cr}$ , such that  $k_1^{cr} = k_1^{cr} + \epsilon\Delta$  and  $\bar{\kappa} = \epsilon\kappa$ . Here,  $\epsilon \ll 1$  and  $\Delta$  are the bookkeeping parameter [56] and the detuning parameter, respectively, typically used in perturbation methods. By substituting  $\sigma_{cr} = \alpha_3 + k_1^{cr}\alpha_6$  and  $\bar{\kappa} = \epsilon\kappa$  in Eq. (3.36a), we get:

$$\frac{d^2}{dt^2}r(t) + 2\zeta\frac{d}{dt}r(t) + \sigma_{cr}r(t) + \vartheta r(t - \tau) + \epsilon\left(\Delta\alpha_6r(t) + \kappa r^3(t)\right) = 0. \quad (3.43)$$

By introducing the new time scale  $T_0 = \epsilon t$  (the slow time scale), and following the procedure of the method of multiple scales (MMS) proposed by Das and Chatterjee [57], the solution  $r(t)$  of Eq. (3.43) is expanded as follows:

$$r(t) = r(t, T_0) = r_0(t, T_0) + \epsilon r_1(t, T_0) + \mathcal{O}(\epsilon^2). \quad (3.44)$$

The time delay term  $r(t - \tau)$  in Eq. (3.43) is expanded as:

$$r(t - \tau) = r(t, T_0, \tau) = r_0(t - \tau, T_0) + \epsilon\left(r_1(t - \tau, T_0) - \tau\frac{\partial r_0(t - \tau, T_0)}{\partial T_0}\right). \quad (3.45)$$

By substituting Eq. (3.44) and Eq. (3.45) into Eq. (3.43), collecting the terms with coefficients  $\epsilon^0$  and  $\epsilon^1$ , and equating these terms to zero, we get:

$$\frac{\partial^2 r_0}{\partial t^2} + 2\zeta \frac{\partial r_0}{\partial t} + \sigma_{cr} r_0 + \vartheta r_0(t - \tau) = 0. \quad (3.46)$$

$$\frac{\partial^2 r_1}{\partial t^2} + 2\zeta \frac{\partial r_1}{\partial t} + \sigma_{cr} r_1 + \vartheta r_1 + 2 \frac{\partial^2 r_0}{\partial t \partial T_0} + 2\zeta \frac{\partial r_0}{\partial T_0} + \Delta\alpha_6 r_0 + \kappa r_0^3 - \vartheta \tau \frac{\partial r_0}{\partial T_0} = 0. \quad (3.47)$$

At a Hopf-bifurcation point, the transient solution of Eq. (3.46) due to the characteristic roots lying on the left half of the complex plane decays with time. The only solution that persists is due to the roots lying on the imaginary axis with frequency  $\omega_{cr}$ . The solution of Eq. (3.46) at a Hopf-bifurcation point can be written as:

$$r_0(t, T_0) = A(T_0) \sin(\omega_{cr} t) + B(T_0) \cos(\omega_{cr} t). \quad (3.48)$$

On substituting Eq. (3.48) into Eq. (3.47) and collecting the terms with similar trigonometric coefficients, we obtain:

$$\begin{aligned} \frac{\partial^2 r_1}{\partial t^2} + 2\zeta \frac{\partial r_1}{\partial t} + \sigma_{cr} r_1 + \vartheta r_1 + L_1 \sin(\omega_{cr} t) + L_2 \cos(\omega_{cr} t) \\ + L_3 \sin(3\omega_{cr} t) + L_4 \cos(3\omega_{cr} t) = 0. \end{aligned} \quad (3.49)$$

In Eq. (3.49), coefficients  $L_1$ ,  $L_2$ ,  $L_3$ , and  $L_4$  are given by

$$\begin{aligned} L_1 = -2 \frac{\partial B}{\partial T_0} \omega_{cr} + \frac{3}{4} \kappa A B^2 + \frac{3}{4} \kappa A^3 + \Delta\alpha_6 A + 2\zeta \frac{\partial A}{\partial T_0} \\ - \vartheta \tau \frac{\partial B}{\partial T_0} \sin(\omega_{cr} \tau) - \vartheta \tau \frac{\partial A}{\partial T_0} \cos(\omega_{cr} \tau), \end{aligned} \quad (3.50a)$$

$$\begin{aligned} L_2 = 2 \frac{\partial A}{\partial T_0} \omega_{cr} + 2\zeta \frac{\partial B}{\partial T_0} + \frac{3}{4} \kappa A^2 B + \Delta\alpha_6 B + \frac{3}{4} \kappa B^3 \\ + \vartheta \tau \frac{\partial A}{\partial T_0} \sin(\omega_{cr} \tau) - \vartheta \tau \frac{\partial B}{\partial T_0} \cos(\omega_{cr} \tau), \end{aligned} \quad (3.50b)$$

$$L_3 = \frac{3}{4} \kappa A B^2 - \frac{1}{4} \kappa A^3, \quad (3.50c)$$

$$L_4 = \frac{1}{4} \kappa B^3 - \frac{3}{4} \kappa A^2 B. \quad (3.50d)$$

Here,  $A(T_0)$  and  $B(T_0)$  are represented as  $A$  and  $B$  for simplicity. The terms  $L_1$  and  $L_2$  cause resonance in Eq. (3.49) and are known as secular terms. Since we know that the solution for  $r(t)$  is bounded, the secular terms in Eq. (3.50) must vanish.



Therefore, by equating  $L_1$  and  $L_2$  to zero, and solving for  $\frac{\partial A}{\partial T_0}$  and  $\frac{\partial B}{\partial T_0}$ , we get:

$$\frac{\partial A}{\partial T_0} = -\frac{1}{4} \left( \frac{C_1 \cos(\omega_{cr}\tau) + C_2 \sin(\omega_{cr}\tau) + C_3}{D_1} \right), \quad (3.51a)$$

$$\frac{\partial B}{\partial T_0} = \frac{1}{4} \left( \frac{C_4 \cos(\omega_{cr}\tau) + C_5 \sin(\omega_{cr}\tau) + C_6}{D_1} \right). \quad (3.51b)$$

Here,

$$D_1 = 4\omega_{cr}^2 + 4\omega_{cr}\vartheta\tau \sin(\omega_{cr}\tau) + \vartheta^2\tau^2 + 4\zeta^2 - 4\zeta\vartheta\tau \cos(\omega_{cr}\tau), \quad (3.52a)$$

$$C_1 = 3\kappa\vartheta\tau AB^2 + 3\kappa\vartheta\tau A^3 + 4A\Delta\alpha_6\vartheta\tau, \quad (3.52b)$$

$$C_2 = -3\vartheta\tau\kappa A^2B - 3\vartheta\tau\kappa B^3 - 4\vartheta\tau\Delta\alpha_6B, \quad (3.52c)$$

$$C_3 = -6\zeta\kappa AB^2 - 8\zeta\Delta\alpha_6A - 6\omega_{cr}\kappa A^2B - 6\zeta\kappa A^3 - 6\omega_{cr}\kappa B^3 - 8\omega_{cr}\Delta\alpha_6B, \quad (3.52d)$$

$$C_4 = 3\vartheta\tau\kappa A^2B + 3\vartheta\tau\kappa B^3 + 4\vartheta\tau\Delta\alpha_6B, \quad (3.52e)$$

$$C_5 = 3\kappa\vartheta\tau AB^2 + 3\kappa\vartheta\tau A^3 + 4\Delta\alpha_6\vartheta\tau A, \quad (3.52f)$$

$$C_6 = -6\kappa\zeta A^2B + 6\omega_{cr}\kappa AB^2 - 8\Delta\alpha_6\zeta B + 8\omega_{cr}\Delta\alpha_6A - 6\kappa\zeta B^3 + 6\omega_{cr}\kappa A^3. \quad (3.52g)$$

We now introduce the following polar transformations for  $A(t)$  and  $B(t)$ :

$$A = R(t) \sin(\theta(t)), \quad (3.53a)$$

$$B = R(t) \cos(\theta(t)). \quad (3.53b)$$

On substituting Eq. (3.53a) and Eq. (3.53b) into Eq. (3.51a) and Eq. (3.51b), and using the relations  $\frac{dA(T_0)}{dt} = \epsilon \frac{dA}{dT_0} + \mathcal{O}(\epsilon^2)$  and  $\frac{dB(T_0)}{dt} = \epsilon \frac{dB}{dT_0} + \mathcal{O}(\epsilon^2)$ , we solve for  $\dot{R}$  and  $\dot{\theta}$ :

$$\dot{R}(t) = \Upsilon(t) \left( \frac{2\zeta - \vartheta\tau \cos(\omega_{cr}\tau)}{\Pi} \right) R(t), \quad (3.54a)$$

$$\dot{\theta}(t) = \Upsilon(t) \left( \frac{2\omega_{cr} + \vartheta\tau \sin(\omega_{cr}\tau)}{\Pi} \right), \quad (3.54b)$$

$$\Upsilon(t) = \frac{\epsilon}{4} (3\kappa R^2(t) + 4\Delta\alpha_6). \quad (3.54c)$$

The approximate solution of the DDE given by Eq. (3.43), accurate to  $\mathcal{O}(\epsilon^0)$ , can now be written using the normal-form equations, Eqs. (3.54a) and (3.54b), as follows:

$$r(t) \approx R(t) \cos(\omega_{cr}t + \theta(t)), \quad (3.55a)$$

$$\dot{r}(t) \approx R(t) \sin(\omega_{cr}t + \theta(t))(\omega_{cr}t + \dot{\theta}(t)) - \dot{R}(t) \cos(\omega_{cr}t + \theta(t)). \quad (3.55b)$$

Equation (3.54a) has two fixed points:  $R_1^* = 0$  and  $R_2^* = \sqrt{-\frac{4\alpha_6\Delta}{3\kappa}}$ . The fixed point  $R_1^*$  corresponds to zero equilibrium, and the fixed point  $R_2^*$  corresponds to the steady-state amplitude of the limit cycle that exists at the Hopf bifurcation.

Upon analyzing the behavior of the system at the bifurcation points  $P_1$  to  $P_5$ , the nature of the bifurcation at those points can be determined. From Fig. 3.4, it is clear that points  $P_1$ ,  $P_3$ , and  $P_5$  exhibit a similar kind of bifurcation, with the system transitioning from an unstable regime to a stable regime. Also, at points  $P_1$ ,  $P_3$ , and  $P_5$ , the zero equilibrium given by  $R_1^* = 0$  is unstable for  $\epsilon\Delta < 0$  and stable for  $\epsilon\Delta > 0$ . This can be interpreted as follows. A dimensionless linear stiffness larger than  $k_1^{cr}$  at these points is required for the cantilever system to be stable at  $U = 7$ . Any decrease in  $k_1$  would take the cantilever into the unstable regime where it would vibrate with large amplitude. On the other hand, points  $P_2$  and  $P_4$  have the same kind of bifurcation, with the system transitioning from a stable regime to an unstable regime. At these points, the zero equilibrium given by  $R_1^* = 0$  is stable for  $\epsilon\Delta < 0$  and unstable for  $\epsilon\Delta > 0$ . Increasing  $k_1$  beyond  $k_1^{cr}$  at these points ( $k_1 = k_1^{cr} + \epsilon\Delta$ ) will push the cantilever into the unstable regime and cause it to vibrate with large amplitude, while decreasing  $k_1$  is more suitable to operate the system in a stable configuration. These inferences can also be drawn by traveling along the line  $U = 7$  in Fig. 3.4. The second equilibrium, corresponding to  $R_2^* = \sqrt{-\frac{4\alpha_6\Delta}{3\kappa}}$ , does not exist for  $\Delta > 0$  and is stable for  $\Delta < 0$ . In the next section, the nature of the Hopf bifurcation, whether supercritical or subcritical, at points  $P_1$  to  $P_5$  has been determined. It is assumed that  $k_2 = 50$  for the analysis that follows. In all the bifurcation diagrams reported in this chapter, solid lines are used to represent stable solutions, while dashed lines are used to represent unstable solutions. Also, non-zero equilibrium solutions ( $R \neq 0, R = R_2^*$ ) correspond to the amplitudes of the periodic solutions that arise from Hopf bifurcation.

### 3.5.1 Supercritical Hopf bifurcation at points $P_1, P_3, P_5$

Substituting the values of  $k_1^{cr}$  and  $\omega_{cr}$  at point  $P_1$  (see Table 3.2) in Eq. (3.54), we get:

$$\dot{R}(t) = -11.1654R(t)^3 - 0.0744(\epsilon\Delta)R(t), \quad (3.56a)$$

$$\dot{\theta}(t) = -64.6292R(t)^2 - 0.4309(\epsilon\Delta). \quad (3.56b)$$

Figure 3.7(a) shows the local bifurcation diagram (supercritical Hopf bifurcation) obtained from Eq. (3.56a). The blue circles in Fig. 3.7(a) are the amplitudes of the

periodic solutions obtained by integrating Eq. (3.43) using the *dde23* MATLAB solver. For numerically integrating Eq. (3.43), a history function must be defined. First, with the initial conditions  $R(0)$  and  $\theta(0)$ , the set of ODEs given by Eqs. (3.56a) and (3.56b) are solved. Then,  $r(t)$  (Eq. (3.55a)) and  $\dot{r}(t)$  (Eq. (3.55b)) obtained for the interval  $[0, \tau]$ , where  $\tau = \frac{2\pi}{U}$ , is given as the history function for Eq. (3.43). Figures 3.7(b) (for  $\epsilon\Delta = -1$ ) and 3.7(c) (for  $\epsilon\Delta = +1$ ) show  $R(t)$  obtained using Eq. (3.56) (red line) and the system response obtained by integrating Eq. (3.43) using the *dde23* MATLAB solver (blue line).

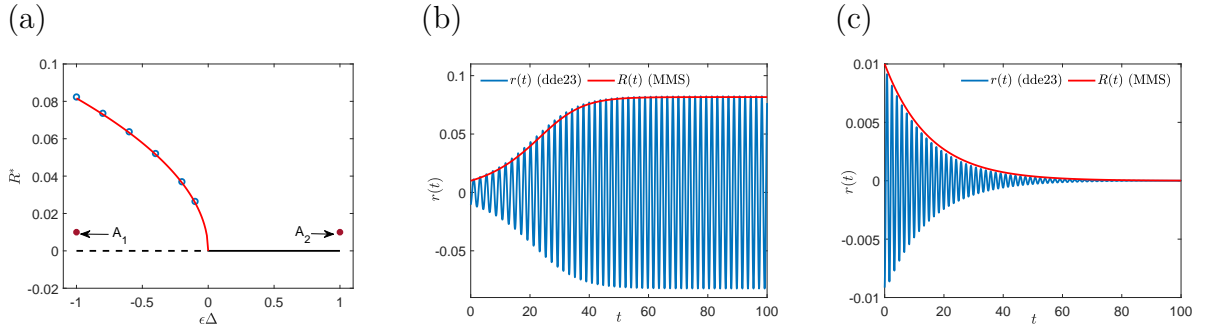


FIGURE 3.7: (a) Local bifurcation diagram at point  $P_1$ . System response at  $P_1$  for (b)  $\epsilon\Delta = -1$  with initial conditions for Eqs. (3.56a) and (3.56b) given by point  $A_1$  in Fig. 3.7(a) and (c)  $\epsilon\Delta = +1$  with initial conditions for Eqs. (3.56a) and (3.56b) given by point  $A_2$  in Fig. 3.7(a).

Next, substituting for the values of  $k_1^{cr}$  and  $\omega_{cr}$  at point  $P_3$  (see Table 3.2) in Eq. (3.54), we get:

$$\dot{R}(t) = -1.1840R(t)^3 - 0.0079(\epsilon\Delta)R(t), \quad (3.57a)$$

$$\dot{\theta}(t) = -22.1355R(t)^2 - 0.1476(\epsilon\Delta). \quad (3.57b)$$

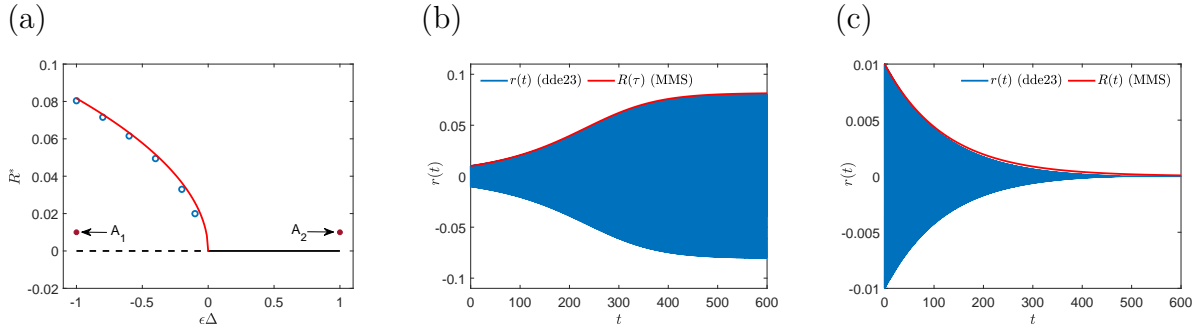


FIGURE 3.8: (a) Local bifurcation diagram at point  $P_3$ . System response at  $P_3$  for (b)  $\epsilon\Delta = -1$  with initial conditions for Eqs. (3.57a) and (3.57b) given by point  $A_1$  in Fig. 3.8(a) and (c)  $\epsilon\Delta = +1$  with initial conditions for Eqs. (3.57a) and (3.57b) given by point  $A_2$  in Fig. 3.8(a).

Figure 3.8(a) shows the local bifurcation diagram (supercritical Hopf bifurcation) obtained from Eq. (3.57a). Figures 3.8(a), 3.8(b) and 3.8(c) are similar to Figs. 3.7(a), 3.7(b) and 3.7(c), respectively, except that the results shown in Fig. 3.8 are for the bifurcation point  $P_3$ .

Finally, substituting the values of  $k_1^{cr}$  and  $\omega_{cr}$  for point  $P_5$  (see Table 3.2) in Eqs. (3.54a), (3.54b), and (3.54c), we get:

$$\dot{R}(t) = -0.3519R(t)^3 - 0.0023(\epsilon\Delta)R(t), \quad (3.58a)$$

$$\dot{\theta}(t) = -13.3505R(t)^2 - 0.0890(\epsilon\Delta). \quad (3.58b)$$

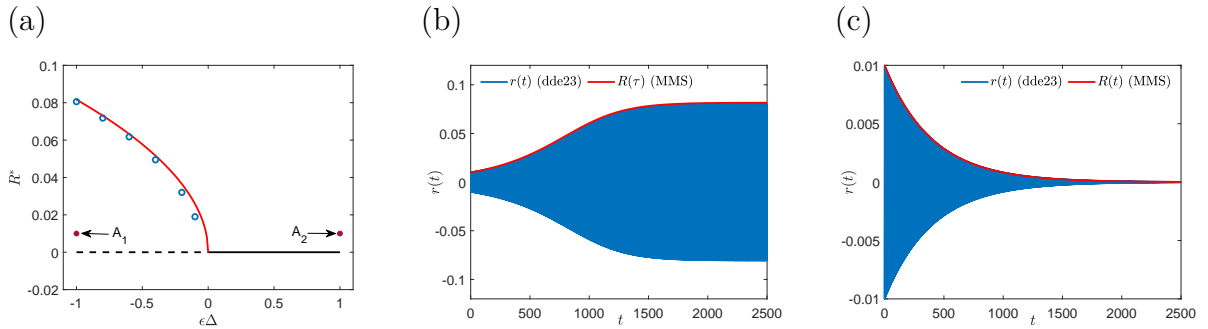


FIGURE 3.9: (a) Local bifurcation diagram at point  $P_5$ . System response at point  $P_5$  for (b)  $\epsilon\Delta = -1$  with initial conditions for Eqs. (3.58a) and (3.58b) given by point  $A_1$  in Fig. 3.9(a) and (c)  $\epsilon\Delta = +1$  with initial conditions for Eqs. (3.58a) and (3.58b) given by point  $A_2$  in Fig. 3.9(a).

Figure 3.9(a) shows the local bifurcation diagram (supercritical Hopf bifurcation) obtained from Eq. (3.58a). Figures 3.9(a), 3.9(b) and 3.9(c) are similar to

Figs. 3.8(a), 3.8(b) and 3.8(c), respectively, except that the results shown in Fig. 3.9 are for the bifurcation point  $P_5$ . It can be seen from Figs. 3.7, 3.8 and 3.9 that both, the transient and steady-state solutions of the normal-form equation, obtained using MMS, match closely with the results from direct numerical integration. This indicates that both the methods outlined above provide a relatively accurate estimate of the stability behavior around points  $P_1$ ,  $P_3$ , and  $P_5$ . These two methods give consistent results.

Figures 3.7, 3.8 and 3.9 indicate that  $P_1$ ,  $P_3$ , and  $P_5$  are points of supercritical Hopf bifurcation. For  $\epsilon\Delta < 0$ , the zero equilibrium is unstable as is expected (see Fig. 3.4). For an initial condition given by point  $A_1$ , the system will move away from zero equilibrium and settle into a stable limit cycle, where it will oscillate with an amplitude  $R^*$  that corresponds to that value of  $\epsilon\Delta$  (Figs. 3.7(b), 3.8(b), and 3.9(b)). For  $\epsilon\Delta > 0$ , the zero equilibrium is stable, as expected (see Fig. 3.4). For an initial condition given by point  $A_2$ , the system will settle back into zero equilibrium and the amplitude of oscillations will damp down to zero (Figs. 3.7(c), 3.8(c), and 3.9(c)). This is consistent with our observations from Fig. 3.4.

### 3.5.2 Subcritical Hopf bifurcation at points $P_2$ and $P_4$

Substituting for the values of  $k_1^{cr}$  and  $\omega_{cr}$  at point  $P_2$  (see Table 3.2) in Eq. (3.54), we get:

$$\dot{R}(t) = 2.0957R(t)^3 + 0.0140(\epsilon\Delta)R(t), \tag{3.59a}$$

$$\dot{\theta}(t) = -30.2325R(t)^2 - 0.2016(\epsilon\Delta). \tag{3.59b}$$

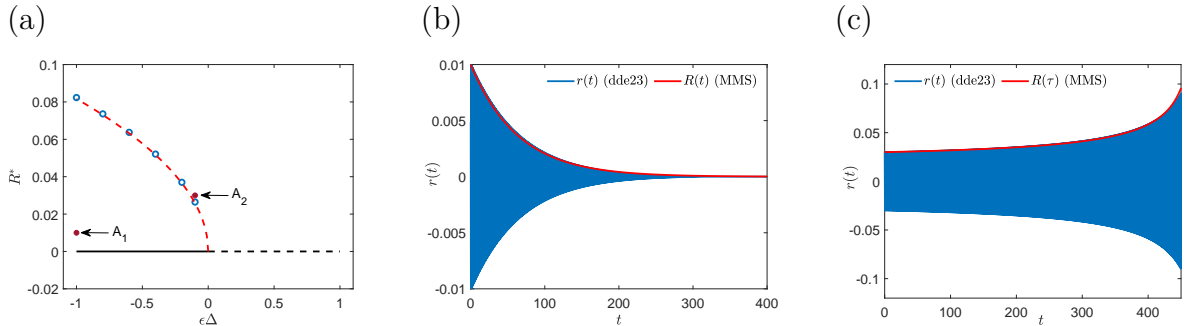


FIGURE 3.10: (a) Local bifurcation diagram at point  $P_2$ . System response at point  $P_2$  for (b)  $\epsilon\Delta = -1$  with initial conditions for Eqs. (3.59a) and (3.59b) given by point  $A_1$  in Fig. 3.10(a) and (c)  $\epsilon\Delta = -0.1$  with initial conditions for Eqs. (3.59a) and (3.59b) given by point  $A_2$  in Fig. 3.10(a).

Figure 3.10(a) shows the local bifurcation diagram (subcritical Hopf bifurcation) obtained from Eq. (3.59a). For a given  $\epsilon\Delta$ , the amplitude of unstable periodic solutions is obtained from Eq. (3.43) as follows. We numerically integrate Eq. (3.43) for increasing values of constant history function and track the equilibrium solution. The critical value of the magnitude of the history function, above which the equilibrium will not approach zero, is considered to be the magnitude of the unstable limit cycle (blue circle). Figure 3.10(b) shows  $R(t)$  obtained using Eq. (3.59a) (red line) and the system response ( $r(t)$ ) obtained by integrating Eq. (3.43) using the *dde23* MATLAB solver (blue line). Both cases are for  $\epsilon\Delta = 0.1$ , and for the magnitude of history function given by point  $A_1$  in Fig. 3.10(a). Figure 3.10(c) shows the same physical quantities as 3.10(b), except that the magnitude of the history function is given by point  $A_2$  in Fig. 3.10(a).

Next, substituting the values of  $k_1^{cr}$  and  $\omega_{cr}$  at point  $P_4$  (see Table 3.2) in Eq. (3.54), we get:

$$\dot{R}(t) = 0.4379R(t)^3 + 0.0029(\epsilon\Delta)R(t), \quad (3.60a)$$

$$\dot{\theta}(t) = -15.1416R(t)^2 - 0.1010(\epsilon\Delta). \quad (3.60b)$$

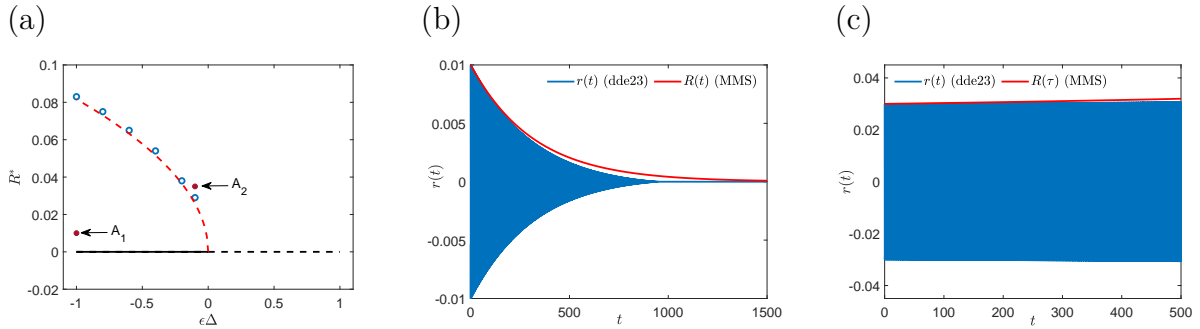


FIGURE 3.11: (a) Local bifurcation diagram at point  $P_4$ . System response at  $P_4$  for (b)  $\epsilon\Delta = -1$  with initial conditions for Eqs. (3.60a) and (3.60b) given by point  $A_1$  in Fig. 3.11(a) and (c)  $\epsilon\Delta = -0.1$  with initial conditions for Eqs. (3.60a) and (3.60b) given by point  $A_2$  in Fig. 3.11(a).

Figure 3.11(a) shows the local bifurcation diagram (subcritical Hopf bifurcation) obtained from Eq. (3.60a). Figures 3.11(a), 3.11(b) and 3.11(c) are similar to Figs. 3.10(a), 3.10(b) and 3.10(c), except that the results shown in Fig. 3.11 are for the bifurcation point  $P_4$ . It can be seen from Figs. 3.10 and 3.11 that both, the transient and steady-state solutions of the normal-form equation, obtained using MMS, match closely with the results from direct numerical integration. Furthermore, it is observed

that both  $P_2$  and  $P_4$  are points of subcritical Hopf bifurcation. For  $\epsilon\Delta < 0$ , the zero equilibrium is stable, as expected (Fig. 3.4). For an initial condition given by point  $A_1$ , the system will settle back into zero equilibrium and the amplitude of oscillations will damp down to zero (Figs. 3.10(b) and 3.11(b)). For an initial condition given by point  $A_2$ , the system will move away from the unstable equilibrium and further away from the stable zero equilibrium. Again, for  $\epsilon\Delta > 0$ , the zero equilibrium is unstable, as expected (from Fig. 3.4).

At this point, the response of the system in the unstable regions (white regions in Fig. 3.4) is still unknown. Furthermore, the MMS only provides information about the system behavior in the proximity of the bifurcation points. In order to assess the behavior of the cantilever farther away from points  $P_1$  to  $P_5$ , a global bifurcation analysis is required. This shall be discussed in Section 3.6.

### 3.6 Global bifurcation analysis

In this section, the global bifurcation diagram and limit cycles for the system described by Eq. (3.17) are developed. The system response is obtained by integrating Eq. (3.17) using the *dde23* MATLAB solver for a fixed value of  $k_1$ , at  $U = 7$ , where  $k_1 \in (0, 100]$ . The maximum value of the amplitude of the response is tracked. The process is repeated for the entire range of  $k_1$  considered here. The global bifurcation diagram is presented in Fig. 3.12(a). Solid black lines represent stable equilibria and dashed black lines represent unstable equilibria. The red, blue, and green solid lines represent the

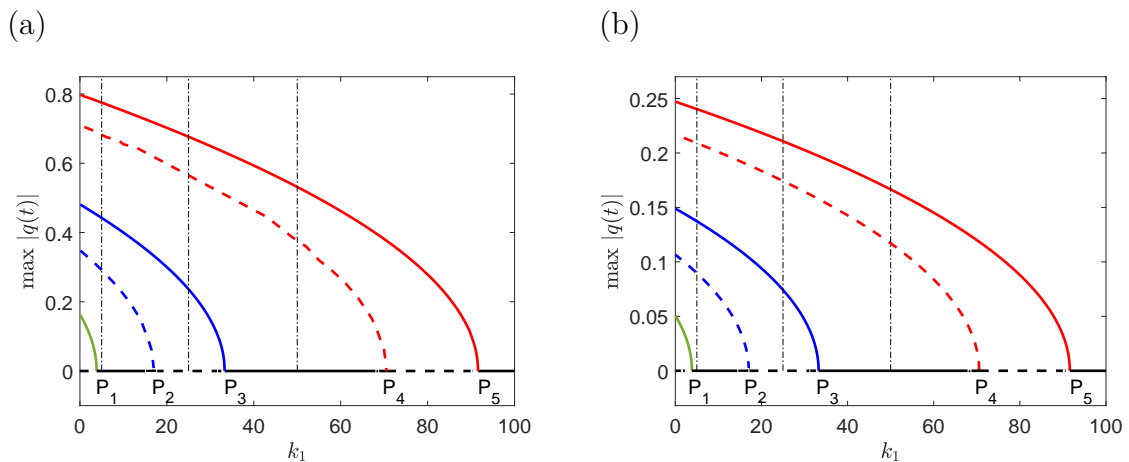


FIGURE 3.12: Global bifurcation diagram obtained from Eq. (3.17) for  $U = 7$  and  $k_1 \in (0, 100]$ , for (a)  $k_2 = 50$  and (b)  $k_2 = 500$ ; vertical dash-dotted lines represent  $k_1 = 5$ ,  $k_1 = 25$ , and  $k_1 = 50$ .

stable solutions originating from the supercritical Hopf bifurcation at points  $P_5$ ,  $P_3$ , and  $P_1$ , respectively. The red and blue dashed lines represent the unstable solutions originating from the subcritical Hopf bifurcation at points  $P_4$  and  $P_2$ , respectively. The stable limit cycles are obtained by directly integrating the DDE given by Eq. (3.13) and the unstable limit cycles are obtained using the bisection method [58].

The following important observations can be made from Fig. 3.12(a). For the parameters considered, there exists no cyclic-fold bifurcation (see Fig. 3.12(a)). This essentially implies that the stable and unstable periodic solutions emerging from the supercritical and subcritical Hopf bifurcation points do not meet. Next, it must be noted that the zero equilibrium is stable between  $P_1$  and  $P_2$ , between  $P_3$  and  $P_4$ , and beyond  $P_5$ . These regions correspond to  $k_1 \in [3.85, 17)$ ,  $k_1 \in [33, 70)$ , and  $k_1 \in [90, 100]$ , respectively. From a design standpoint,  $k_1 \in [33, 70)$  seems most desirable, which can be explained as follows. At a certain point in time, if the cantilever is vibrating with a sufficiently small amplitude (the initial condition) in this range of  $k_1$ , the system will fall back to zero equilibrium (solid black lines in Fig. 3.12(a)) and the oscillations will die out. For instance, at  $k_1 = 50$ , if the cantilever is vibrating with an initial amplitude of around 0.3, the system will settle into the stable zero equilibrium and the oscillations will die out. If it is vibrating with an initial amplitude greater than 0.4, it will settle into the stable limit cycle (solid red line in Fig. 3.12) originating at point  $P_5$  and will vibrate with the corresponding amplitude. If the system is vibrating with an initial amplitude that corresponds exactly to the unstable limit cycle for  $k_1 = 50$ , a small fluctuation in  $U$  will take it either to zero equilibrium, or to the periodic motion associated with the aforementioned stable limit cycle. Even if the initial amplitude is greater than or equal to 0.7, the beam will settle into the stable limit cycle and take on periodic motion.

Let us now consider more extreme values of  $k_1$ . For example, when  $k_1 = 100$ , if the system is vibrating at a sufficiently small amplitude, it will settle into the zero equilibrium state (solid black line in Fig. 3.12(a)). However, the linear stiffness ( $K_1$ ) is required to be relatively high, which would introduce high stresses on the tube, as mentioned in Section 3.1. Furthermore, a high cladding stiffness may not be viable for multiple tubes. For extremely low values of  $k_1$ , for instance  $k_1 = 5$ , the system can settle into periodic motion corresponding to two stable limit cycles depending on its initial amplitude of oscillation. If the initial amplitude is greater than or equal to 0.7, the beam will settle into the stable limit cycle originating from point  $P_5$  (solid red line in Fig. 3.12(a)). The amplitude of oscillation in this limit cycle at  $k_1 = 5$  is much larger than the amplitude in the same limit cycle for  $k_1 = 50$ , which makes operating at  $k_1 = 50$  more favorable. Furthermore, while an initial amplitude less than or equal



to 0.4 will take the system to the more desirable stable, zero equilibrium for  $k_1 = 50$ , it will take the system to the relatively less desirable periodic motion associated with a stable limit cycle (solid blue line in Fig. 3.12(a)) for  $k_1 = 5$ .

Limit cycles for  $k_1 = 5$ ,  $k_1 = 25$  and  $k_1 = 50$  are shown in Figs. 3.13(a), 3.13(b) and 3.13(c), respectively. Four coexisting limit cycles are present for  $k_1 = 5$  (Fig. 3.13(a)). Of these, two unstable limit cycles arise from the subcritical Hopf bifurcation originating at points  $P_2$  (dashed blue line) and  $P_4$  (dashed red line), and two stable limit cycles arise from the supercritical Hopf bifurcation originating at points  $P_3$  (solid blue line) and  $P_5$  (solid red line). For  $k_1 = 25$ , three limit cycles coexist (see Fig. 3.13(b)). Of these, two stable limit cycles arise from the supercritical Hopf bifurcation originating at points  $P_3$  (solid blue line) and  $P_5$  (solid red line), and one unstable limit cycle arises from the subcritical Hopf bifurcation originating at point  $P_4$  (dashed red line). For  $k_1 = 50$ , only two coexisting limit cycles are present (Fig. 3.13(c)): one is an unstable limit cycle arising from the subcritical Hopf bifurcation originating at point  $P_4$  (dashed red line) and the other is a stable limit cycle arising from the supercritical Hopf bifurcation originating at point  $P_5$  (solid red line). This can be easily verified by comparing Fig. 3.13 with Fig. 3.12(a).

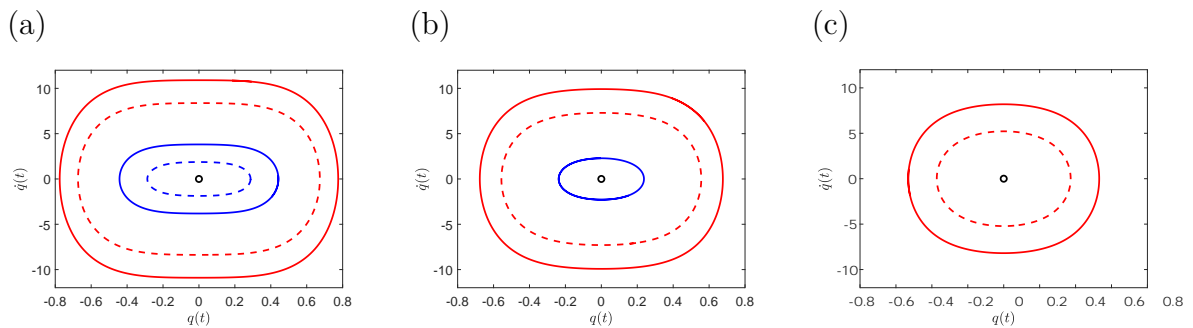


FIGURE 3.13: Limit cycles for  $U = 7$  with (a)  $k_1 = 5$ , (b)  $k_1 = 25$  and (c)  $k_1 = 50$ .

The number of limit cycles decreases with increasing values of  $k_1$ . From the discussion regarding Fig. 3.12(a), it is clear that up to  $k_1 = 70$ , fewer limit cycles are more favorable. An example of this is seen by comparing Figs. 3.13(c) and 3.13(a). For an initial amplitude of approximately 0.3 for  $k_1 = 50$  (Fig. 3.13(c)), the oscillations will die out, while for  $k_1 = 5$  (Fig. 3.13(a)), the system will settle into periodic motion associated with a stable limit cycle (solid blue line in Fig. 3.13(a)). Similarly, for an initial amplitude of approximately 0.2 for  $k_1 = 50$  (Fig. 3.13(c)), the oscillations will likewise die out, while for  $k_1 = 25$ , the system will settle into periodic motion associated with the nearest stable limit cycle (solid blue line in Fig. 3.13(a)). Finally, for an initial amplitude of greater than or equal to 0.7, the system settles into periodic

motion of a lower amplitude for  $k_1 = 50$  (Fig. 3.13(c)) compared to that for  $k_1 = 5$  (Fig. 3.13(a)) and  $k_1 = 25$  (Fig. 3.13(b)).

The discussion above is for  $k_2 = 50$ . The effect of change in  $k_2$  is investigated next. The bifurcation diagrams for  $k_2 = 50$  and  $k_2 = 500$  are compared in Fig. 3.12. Figure 3.12 shows that the only difference between the two cases is that the limit-cycle amplitudes decrease when  $k_2 = 500$ ; all other characteristics of the system remain the same. This suggests that there are no qualitative differences in the behavior of the system with change in the dimensionless cubic-spring stiffness ( $k_2$ ). Furthermore, it is evident that  $k_2 = 50$  is a stronger choice for our analysis since it corresponds to larger limit-cycle amplitudes, i.e., the worse case between the two.

It must be noted that our deductions are based on dimensionless parameters that can be used to back-calculate physically measurable quantities (see Eq. (3.11b)). The advantage of using dimensionless parameters is that it gives us the flexibility of adjusting several dimensional quantities for a fixed value of the dimensionless parameter, with minimal computational overhead. It can be seen that once  $k_1$  and  $k_2$  are chosen, the engineer can adjust the dimensional design parameters ( $K_1, K_2, I, L, D$ ) to get the desired values of  $k_1$  and  $k_2$  that correspond to the region of fewer limit cycles or a region of high damping.

## 3.7 Chapter Summary

Much of the work in this study is new and pertinent to emerging studies on heat-exchanger tubes. This is the first time that the MMS technique has been employed to investigate Hopf bifurcation for a single-span heat-exchanger tube supported by baffle-claddings. The results obtained are consistent with those obtained from direct numerical integration of the DDE, which makes the MMS a suitable tool for application to this problem and its counterparts.

Additionally, the stability and spectrum in the parametric space of cladding stiffness and flow velocity has also been obtained for the first time. Stable regions of the spectrum have been clearly delineated from the unstable ones, so that a definitive stability boundary is obtained. The knowledge of damping in the dimensionless parametric space is useful for the control of large-amplitude vibrations. For a given value of operational flow velocity, the value of  $k_1$  can be traced back from a region where the damping is high. The linear spring stiffness ( $K_1$ ) can then be back-calculated (Eq. (3.11b)). In this manner, the system can be designed with a  $K_1$ , so as to operate

it in a region where the damping is high, thereby guaranteeing maximum stability for a given operational flow velocity.

Another contribution of this chapter is its relevance to fatigue life calculations of heat-exchanger tubes. Fatigue life calculations are dependent on the amplitude and frequency of tube vibrations [59]. Multiple limit cycles (both stable and unstable) are found to exist for  $k_1 \in (0, 100]$ . In the case of a stable zero equilibrium and a single stable limit cycle ( $k_1 \in (33, 70]$ ), fatigue life calculations are easier. When there are multiple periodic solutions, fatigue life calculations must be based on the worst-case scenario, i.e., the largest limit-cycle amplitude. Therefore, this study is expected to be very useful at the design stage of heat-exchanger tubes. Furthermore,  $k_1 \in (33, 70]$  provides a range for optimal design values of  $k_1$ . High values of  $k_1$  can induce high stresses on the tube in response to tube thermal expansion. Moreover, the analysis above also indicates that high values of  $k_1$ , i.e., stiffer claddings, do not necessarily guarantee a more stable system. On the other hand, low values of  $k_1$  may not be effective against impact with baffles, while also subjecting the system to the risk of multiple periodic solutions. The range  $k_1 \in (33, 70]$  is most desirable for design purposes since the zero equilibrium is stable and there is only one stable limit cycle in this range. Finally, it must be noted that increasing the cubic spring stiffness is found to decrease the limit-cycle amplitudes. However, the qualitative behavior of the system remains the same.

In the past, Sadath et al. [39] had modeled the impact load on a cantilevered heat-exchanger tube using a cubic spring. Beyond the critical velocity, limit cycle motion was observed, similar to the above analysis. After the first Hopf bifurcation, the tube impacts with the baffle and oscillates locally, before chaotic motion that sets in beyond a certain value of the flow velocity. Similarly, Wang and Ni [29] found that the amplitude of their vibrating cantilevered tube increased until impact with the loose support at the tip, which led to quasi-periodic and chaotic motions at high velocities. In the sequence of events that transpire when a heat-exchanger tube undergoes cross-flow-induced oscillations, the current study precedes that of refs. [29, 39] in the following manner. The system first oscillates with limit cycle motion; the cladding deforms in time creating a clearance between the tube and the cladding; the clearance then allows for there to be impact between the tube and the cladding, which can be investigated using ref. [29, 39].

## Chapter 4

# Supercritical and Subcritical Hopf Bifurcations in a Delay Differential Equation Model of a Heat-Exchanger Tube Under Cross-flow

### 4.1 Introduction

Nonlinear vibrations of a heat-exchanger tube modeled as a simply-supported Euler-Bernoulli beam under axial load and cross-flow have been studied. The compressive axial loads are a consequence of thermal expansion and tensile axial loads can be induced by design (prestress). The fluid forces are represented using an added mass, damping, and a time-delayed displacement term. Due to the presence of the time-delayed term, the equation governing the dynamics of the tube becomes a partial delay differential equation (PDDE). Using the modal-expansion procedure, the PDDE is converted into a nonlinear delay differential equation (DDE). The fixed points (zero and buckled equilibria) of the nonlinear DDE are found, and their linear stability is analyzed. It is found that stability can be lost either via supercritical or subcritical Hopf bifurcation. Using Galerkin approximations, the characteristic roots (spectrum) of the DDE are found and reported in the parametric space of fluid velocity and axial load. Furthermore, the stability chart obtained from the Galerkin approximations is compared with the critical curves obtained from analytical calculations. Next, the method of multiple scales (MMS) is used to derive the normal-form equations near the supercritical and subcritical Hopf bifurcation points for both zero and buckled equilibrium configurations. The steady-state amplitude response equation, obtained from the MMS, at Hopf bifurcation points is compared with the numerical solution.

The coexistence of multiple limit-cycles in the parametric space is found, and has implications in the fatigue life calculations of the heat-exchanger tubes.

In this chapter, the tube is modeled as an Euler-Bernoulli beam with simply-supported boundary conditions [30], as explained in Section 4.2. Heat-exchanger tubes undergo thermal expansion, and are consequently subject to thermal loads acting along the axial direction. Further, external tensile loads can be induced by design. The model includes the effect of this axial load ( $P_0$ ) and nonlinear effects due to large deformations. The quasi-steady model developed by Paidoussis and Li [37] is employed to obtain a partial integro-delay differential equation that governs the tube motion. This partial delay differential equation (PDDE) is converted into a single nonlinear delay differential equation (DDE) using modal truncation, and its linear stability is analyzed in Section 4.3. It should be noted that a DDE is an infinite-dimensional system and therefore, its characteristic equation has infinitely many eigenvalues. Using Galerkin approximations [49, 55], the spectrum at different flow velocities and axial loads is obtained in Section 4.3.3. The spectrum contains information on the dominant frequencies (and their damping) that will be present in the transient solution. Dominant eigenvalues from the spectrum are used to generate the stability chart. Furthermore, the normal forms for Hopf bifurcation are derived using the method of multiple scales (MMS) [57] in Section 4.4. These normal forms give insights into the nature of Hopf bifurcation (subcritical or supercritical). The approximate amplitude obtained from the normal-form equations, is compared to that from the numerical simulation. From a global bifurcation analysis (Section 4.5), the coexistence of multiple stable and unstable periodic solutions in the parametric space of flow velocity and axial load is shown. Finally, in Section 4.6, the contribution of this chapter is summarized. The presence of multiple periodic solutions bears significance for fatigue life calculations on the tube. Moreover, as explained later in this chapter, tensile axial loads can be induced to control the dynamic response of the tube. Therefore, we expect this study on the tube modeled as a beam to be directly linked to design considerations for heat-exchanger tubes.

## 4.2 Mathematical modeling

Figure 4.1(a) shows the schematic of the heat-exchanger tube bundle with its isometric view along with the coordinate axes. In Fig. 4.1(b), the cross-sectional view of the tube bundle is shown. Figure 4.1(c) shows the idealized model of the heat-exchanger tube as a simply supported beam under axial loads and cross flow fluid forces.

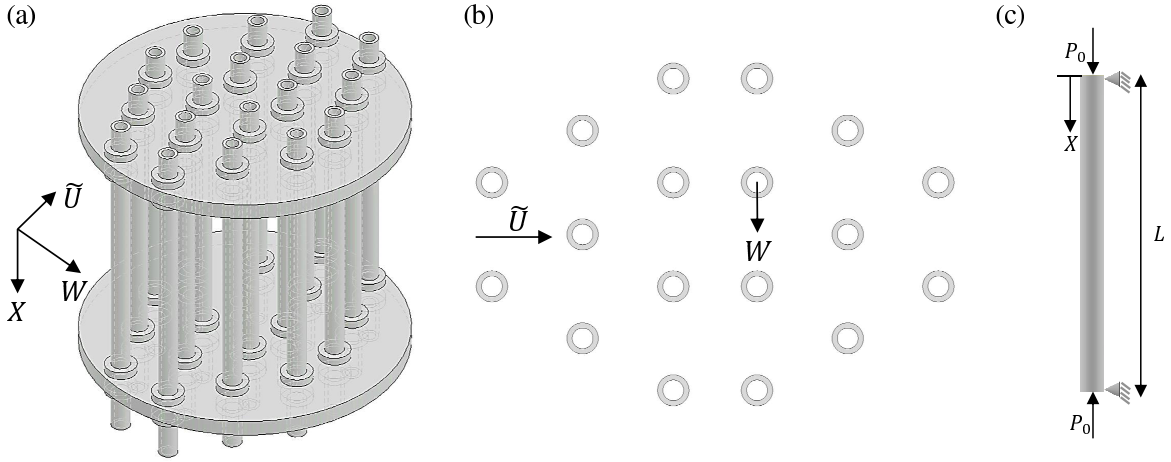


FIGURE 4.1: (a) Schematic of the heat-exchanger tube bundle with its isometric view along with the coordinate axes, (b) the cross-sectional view of the tube bundle, and (c) idealized model of the heat-exchanger tube as a simply supported beam under axial loads and cross flow fluid forces.

The tube is assumed to be of length  $L$ , diameter  $D$ , and cross-sectional area  $A$ , subjected to cross-flow and axial load  $P_0$ , and is modeled in this section using the Euler–Bernoulli beam theory. The governing equation of the transverse displacement  $W(x, t)$  of the tube is written as [30]:

$$EI \frac{\partial^4 W}{\partial X^4} + C \frac{\partial W}{\partial T} + M \frac{\partial^2 W}{\partial T^2} - \frac{EA}{2L} \frac{\partial^2 W}{\partial X^2} \int_0^L \left( \frac{\partial W}{\partial X} \right)^2 dX + P_0 \frac{\partial^2 W}{\partial X^2} = F, \quad (4.1)$$

where  $EI$  and  $C$  are, respectively, the flexural rigidity and damping coefficient of the tube,  $X$  is the spatial coordinate, and  $T$  is time. As the beam is simply-supported, the boundary conditions are written as  $W(0, T) = W(L, T) = 0$  and  $\frac{\partial^2 W}{\partial X^2} \Big|_{X=0} = \frac{\partial^2 W}{\partial X^2} \Big|_{X=L} = 0$ . The axial loads  $P_0$  on the tube are a consequence of the applied tensile axial load  $P_A$  due to prestress and thermal expansion. Defining  $\alpha$  as the thermal expansion coefficient of the heat-exchanger tube material, and  $\Delta\theta$  as the temperature differential for the heat-exchanger tube,  $P_0$  can be written as  $P_0 = EA\alpha\Delta\theta - P_A$ . The motion dependent cross-flow induced forces  $F(W, \dot{W}, \ddot{W})$  acting on the tube are given by [37]:

$$F(W, \dot{W}, \ddot{W}) = -M_f \frac{\partial^2 W}{\partial T^2} - C_f \frac{\partial W}{\partial T} + K_f W(X, T - \Delta T), \quad (4.2)$$

where

$$M_f = \frac{\pi}{4} \rho D^2 C_{ma}, \quad C_f = \frac{1}{2} \rho \tilde{U} D C_D, \quad K_f = \frac{1}{2} \rho \tilde{U}^2 D \frac{\partial C_L}{\partial W}, \quad \text{and} \quad \Delta T = \mu \frac{D}{\tilde{U}}. \quad (4.3)$$

In Eq. (4.3),  $\rho$  and  $\tilde{U}$  are, respectively, the density of the fluid and the free-stream velocity.  $C_D$ ,  $C_L$ , and  $C_{ma}$  are, respectively, the drag, lift, and added-mass coefficients;  $\mu$  is a parameter which relates to the tube-array pattern;  $D$  is the diameter of the heat-exchanger tube; and  $\Delta T$  is the time-delay that arises due to the phase lag between cylinder motion and fluid dynamic forces. By introducing the following non-dimensional quantities in Eq. (4.1):

$$w = \frac{W}{D}, \quad x = \frac{X}{L}, \quad t = \lambda_1^2 \sqrt{\frac{EI}{ML^4}} T = \Omega_1 T, \quad \xi = \frac{C}{\Omega_1 M}, \quad m = \frac{M}{\rho D^2}, \quad (4.4a)$$

$$U = \frac{2\pi\tilde{U}}{D\Omega_1}, \quad p_0 = \frac{P_0 L^2}{EI}, \quad \beta = \frac{\pi C_{ma}}{\pi C_{ma} + 4m}, \quad \text{and} \quad \gamma = \frac{AD^2}{2I\lambda_1^4}. \quad (4.4b)$$

we obtain:

$$\begin{aligned} & \frac{1}{1-\beta} \frac{\partial^2 w}{\partial t^2} + \left( \xi + \frac{UC_D}{4\pi m} \right) \frac{\partial w}{\partial t} + \frac{1}{\lambda_1^4} \frac{\partial^4 w}{\partial x^4} + \frac{p_0}{\lambda_1^2} \frac{\partial^2 w}{\partial x^2} \\ & - \gamma \frac{\partial^2 w}{\partial x^2} \int_0^1 \left( \frac{\partial w}{\partial x} \right)^2 dx - \frac{U^2}{8\pi^2 m} \frac{\partial C_L}{\partial w} w(x, t - \tau) = 0, \end{aligned} \quad (4.5)$$

where  $\lambda_1 = \pi$  is the first non-dimensional natural frequency of the tube and the dimensionless time-delay  $\tau$  is given by  $\tau = 2\pi/U$ , for  $\mu = 1$  [37]. By considering only the first vibrational mode, the solution  $w(x, t)$  of Eq. (4.5) can be written as:

$$w(x, t) = \sqrt{2} \sin(\pi x) q(t). \quad (4.6)$$

Substituting Eq. (4.6) into Eq. (4.5), pre-multiplying the resulting equation by  $\sqrt{2} \sin(\pi x)$ , and then integrating with respect to  $x$  over the domain  $[0, 1]$  results in the following DDE:

$$\frac{1}{1-\beta} \ddot{q}(t) + \left( \xi + \frac{UC_D}{4\pi m} \right) \dot{q}(t) + \left[ 1 - \frac{p_0}{\pi^2} \right] q(t) + \gamma \pi^4 q^3(t) - \frac{U^2}{8\pi^2 m} \frac{\partial C_L}{\partial w} q(t - \tau) = 0. \quad (4.7)$$

Following the procedure outlined in [30], substituting  $\alpha_1 = (1-\beta)\xi$ ,  $\alpha_2 = \frac{(1-\beta)C_D}{4\pi m}$ ,  $\alpha_3 = (1-\beta)$ ,  $\alpha_4 = (1-\beta)\gamma\pi^4$ , and  $\alpha_5 = -\frac{(1-\beta)}{8\pi^2 m} \frac{\partial C_L}{\partial w}$  into Eq. (4.7), we get:

$$\ddot{q}(t) + (\alpha_1 + \alpha_2 U) \dot{q}(t) + \alpha_3 \left[ 1 - \frac{p_0}{\pi^2} \right] q(t) + \alpha_4 q^3(t) + \alpha_5 U^2 q(t - \tau) = 0. \quad (4.8)$$

In Eq. (4.8),  $p_0$  and  $U$  are the parameters of interest, as shall be seen in the next section. It should be noted that the dimensionless time-delay is a derived quantity and is given by  $\tau = 2\pi/U$ . In this chapter, the following numerical values are used for the parameters in Eq. (4.8):  $\alpha_1 = 0.0145$ ,  $\alpha_2 = 0.00524$ ,  $\alpha_3 = 0.76$ ,  $\alpha_4 = 1.1105$ , and  $\alpha_5 = 0.026$ . These parameters are the same as those used by Wang et al. in [30].

### 4.3 Linear stability

In this section, the fixed points of Eq. (4.8) are determined and their linear stability is analyzed. To find the fixed points, we substitute  $q(t) = q(t - \tau) = \bar{q}$  into Eq. (4.8). Next, by dropping the rate-dependent terms at the fixed points, we get:

$$\alpha_3 \left[ 1 - \frac{p_0}{\pi^2} \right] \bar{q} + \alpha_4 \bar{q}^3 + \alpha_5 U^2 \bar{q} = 0. \quad (4.9)$$

Solving for  $\bar{q}$  in Eq. (4.9), we get:

$$\bar{q}_1 = 0, \quad \text{and} \quad \bar{q}_2 = \pm \sqrt{\frac{-\alpha_3 \left[ 1 - \frac{p_0}{\pi^2} \right] - \alpha_5 U^2}{\alpha_4}}. \quad (4.10)$$

In Eq. (4.10), fixed points  $\bar{q}_2$  will be real only if the following condition is satisfied:

$$p_0 > \frac{\alpha_5 \pi^2 U^2 + \alpha_3 \pi^2}{\alpha_3}. \quad (4.11)$$

To study the stability around these fixed points, we substitute  $q(t) = r(t) + \bar{q}$  in Eq. (4.8), which results in

$$\ddot{r}(t) + (\alpha_1 + \alpha_2 U) \dot{r}(t) + \alpha_3 \left[ 1 - \frac{p_0}{\pi^2} \right] r(t) + 3\alpha_4 \bar{q}^2 r(t) + 3\alpha_4 \bar{q} r^2(t) + \alpha_4 r(t)^3 + \alpha_5 U^2 r(t - \tau) = 0. \quad (4.12)$$

By retaining only the linear terms in Eq. (4.12), we obtain the following equation:

$$\ddot{r}(t) + (\alpha_1 + \alpha_2 U) \dot{r}(t) + \alpha_3 \left[ 1 - \frac{p_0}{\pi^2} \right] r(t) + 3\alpha_4 \bar{q}^2 r(t) + \alpha_5 U^2 r(t - \tau) = 0. \quad (4.13)$$

The stability of Eq. (4.13) depends on the roots of its characteristic equation. By substituting  $r(t) = e^{\lambda t}$  in Eq. (4.13), we obtain the following characteristic equation:

$$D(\lambda, U, p_0) = \lambda^2 + (\alpha_1 + \alpha_2 U) \lambda + \alpha_3 \left[ 1 - \frac{p_0}{\pi^2} \right] + 3\alpha_4 \bar{q}^2 + \alpha_5 U^2 e^{-\lambda \tau} = 0. \quad (4.14)$$

The above Eq. (4.14) is a quasipolynomial (due to the presence of the  $e^{-\lambda \tau}$  term) and has infinitely many roots. If the real parts of all the characteristic roots of Eq. (4.14) are negative, then the equilibrium at  $\bar{q}$  is stable. It is generally not possible to obtain the rightmost characteristic roots of Eq. (4.13) in closed form. However, we can get information about the critical curves that separate the stable and unstable regions in the parametric space of  $p_0$  and  $U$ . The stability of Eq. (4.13) around  $\bar{q}$  is lost through Hopf bifurcation when its rightmost characteristic roots cross the imaginary axis (see Fig. 4.2(a)). Alternatively, stability can be lost through a static bifurcation, when the rightmost root crosses the imaginary axis along the real line (see Fig. 4.2(b)).



Therefore, to get the stability boundary, we substitute  $\lambda = j\omega_{cr}$  and  $p_0 = p_{cr}$  in Eq. (4.14) to obtain the following:

$$\left[ -\omega_{cr}^2 + \alpha_3 \left( 1 - \frac{p_{cr}}{\pi^2} \right) + 3\alpha_4 \bar{q}^2 + \alpha_5 U^2 \cos(\omega_{cr}\tau) \right] + j \left[ (\alpha_1 + \alpha_2 U)\omega_{cr} - \alpha_5 U^2 \sin(\omega_{cr}\tau) \right] = 0. \quad (4.15)$$

Equation (4.15) will now be used to obtain the critical curves for different equilibrium points.

### 4.3.1 Critical curves for the equilibrium at $\bar{q} = \bar{q}_1 = 0$

Substituting  $\bar{q} = \bar{q}_1 = 0$  in Eq. (4.15) and setting the real and imaginary parts to zero, the following equations are obtained:

$$-\omega_{cr}^2 + \alpha_3 \left[ 1 - \frac{p_{cr}}{\pi^2} \right] + \alpha_5 U^2 \cos(\omega_{cr}\tau) = 0, \quad (4.16a)$$

$$(\alpha_1 + \alpha_2 U)\omega_{cr} - \alpha_5 U^2 \sin(\omega_{cr}\tau) = 0. \quad (4.16b)$$

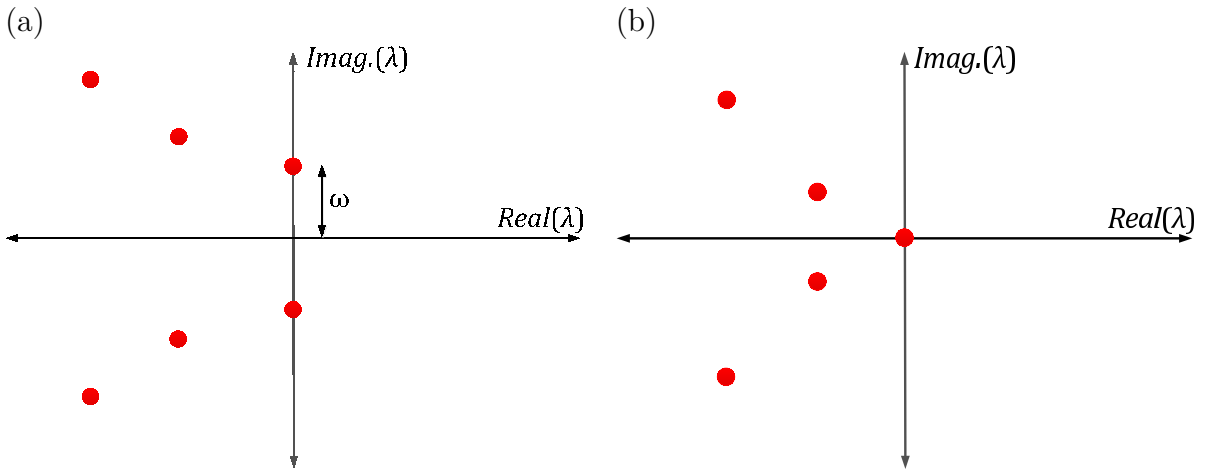


FIGURE 4.2: Two ways in which the rightmost characteristic roots of Eq. (4.13) can cross the imaginary axis, leading to the loss of stability of equilibrium at  $\bar{q}$ : (a)  $\omega_{cr} \neq 0$  (Hopf bifurcation) and (b)  $\omega_{cr} = 0$  (static bifurcation). It should be noted that in both (a) and (b), only the first few rightmost roots of the infinite spectrum of the DDE given by Eq. (4.13) are shown.

For various values of the axial load  $p_{cr}$ , Eqs. (4.16a) and (4.16b) can be solved numerically to determine the variables  $U$  and  $\omega_{cr}$  along the stability boundary. The stability boundary so obtained is represented by curves 1 and 2 in Fig. 4.3. As discussed earlier, the stability at  $\bar{q}_1 = 0$  can also be lost through a static bifurcation

(buckling). To determine the critical curve along which the static bifurcation may occur, we substitute  $\omega_{cr} = 0$  in Eq. (4.16a). Then, the expression relating  $p_{cr}$  and  $U$  is obtained as follows:

$$p_{cr} = \frac{\alpha_5 \pi^2 U^2 + \alpha_3 \pi^2}{\alpha_3}. \quad (4.17)$$

The relationship between  $p_{cr}$  and  $U$ , given by Eq. (4.17) with  $\omega_{cr} = 0$ , is graphically shown by curve 3 in Fig. 4.3. It should be noted that the equilibrium at  $\bar{q}_2$  exists only above curve 3 (see Eq. (4.11)) in the  $p_0$  and  $U$  parameter space.

### 4.3.2 Critical curves for the equilibrium at $\bar{q} = \bar{q}_2$

In this section, the stability boundary for equilibrium at  $\bar{q}_2$  is discussed. Substituting  $\bar{q} = \bar{q}_2$  (Eq. (4.10)) in Eq. (4.15), and setting the real and imaginary parts of the resulting expression to zero, we get:

$$-\omega_{cr}^2 - 2\alpha_3 \left(1 - \frac{p_{cr}}{\pi^2}\right) - 3\alpha_5 U^2 + \alpha_5 U^2 \cos(\omega_{cr} \tau) = 0, \quad (4.18a)$$

$$\left(\alpha_1 + \alpha_2 U\right) \omega_{cr} - \alpha_5 U^2 \sin(\omega_{cr} \tau) = 0. \quad (4.18b)$$

For different values of  $U$ , one can solve Eqs. (4.18a) and (4.18b) numerically for the values of  $p_{cr}$  and  $\omega_{cr}$  on the stability boundary. This boundary is shown by curves 4 and 5 in Fig. 4.3. The stability of the equilibrium at  $\bar{q} = \bar{q}_2$  can also be lost through a static bifurcation (see Fig. 4.2(b)), where  $\omega_{cr} = 0$ . Substituting  $\omega_{cr} = 0$  in Eq. (4.18a), the equation relating  $p_{cr}$  and  $U$  is obtained as follows:

$$p_{cr} = \frac{\alpha_5 \pi^2 U^2 + \alpha_3 \pi^2}{\alpha_3}. \quad (4.19)$$

Equation (4.19) is the same as Eq. (4.17) and hence the stability boundary is given by curve 3 in Fig. 4.3.

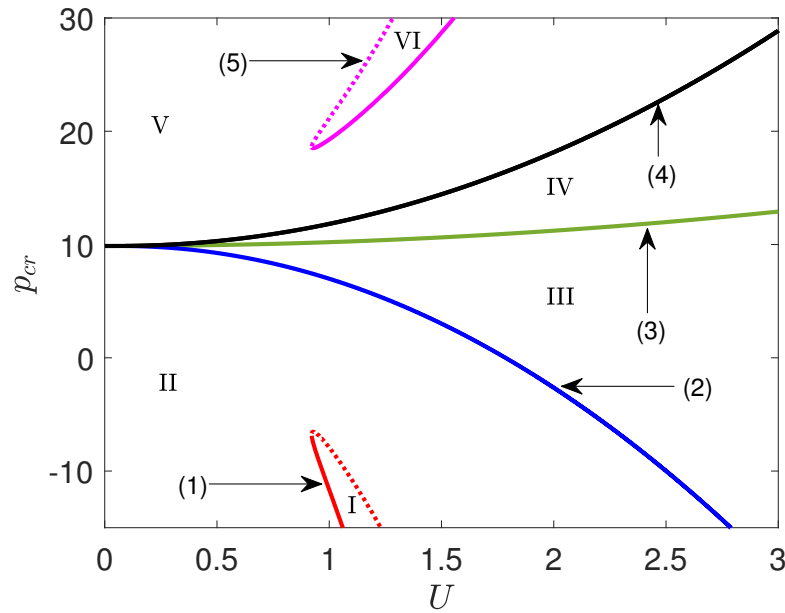


FIGURE 4.3: Critical curves for Hopf and static bifurcation for equilibrium points  $\bar{q}_1 = 0$  and  $\bar{q}_2$ . Curves 1, 2, 4, and 5 correspond to Hopf bifurcation ( $\omega_{cr} \neq 0$ ) and curve 3 corresponds to static bifurcation ( $\omega_{cr} = 0$ ). Six regions are labeled (I to VI) for later discussion.

In Fig. 4.3, all the stability boundaries are shown. However, one must exercise caution when determining the stable and unstable regions from Fig. 4.3. For example, the conditions for Hopf bifurcation given by Eqs. (4.16a) and (4.16b) or by Eqs. (4.18a) and (4.18b) are satisfied as long as a pair of roots lie on the imaginary axis. In Fig. 4.4(a), although the system is unstable, the second pair of eigenvalues lie exactly on the imaginary axis and satisfy the analytical conditions imposed on the stability boundary. Similarly, the condition  $\omega_{cr} = 0$ , imposed on the characteristic roots for the case of static bifurcation, is satisfied even for the case shown in Fig. 4.4(b) for which the system is unstable. Therefore, it is difficult to determine the stable and unstable regions directly from Fig. 4.3. For understanding the stability behavior of the tube, we divide the stability chart into six regions, shown as I-VI in Fig. 4.3. In the next section, we shall develop Galerkin approximations for the linear DDE given by Eq. (4.13) and numerically obtain its characteristic roots, after which it is straightforward to comment on stability. The distribution of the characteristic roots (spectrum) of Eq. (4.13) for different flow velocities and axial loads will also be studied. The spectrum will also give us insights into the regions of maximum damping in the  $p_0$  and  $U$  space.

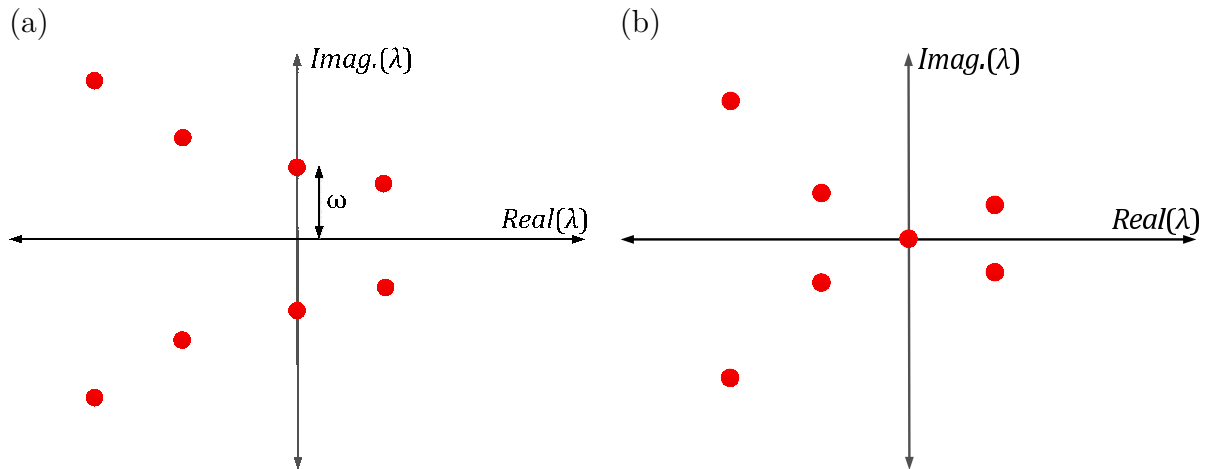


FIGURE 4.4: Possible locations of the characteristic roots on the critical curves for the case of (a)  $\omega_{cr} \neq 0$  and (b)  $\omega_{cr} = 0$ . It should be noted that in both (a) and (b), only the first few rightmost roots of the infinite spectrum of the DDE given by Eq. (4.13) are shown.

### 4.3.3 Spectrum

Several methods exist in the literature to study the stability of time-delayed systems (TDS) by obtaining their characteristic roots. Some of these methods are Lambert W function [60–63], Galerkin approximations [64–66], semi-discretization [67], pseudospectral collocation [68–70], continuous-time approximation [71, 72], and quasipolynomial root finder algorithm (QPmR) [73]. Cluster treatment of characteristic roots approach is another powerful tool to obtain accurate stability charts for TDS [74]. Pekař and Gao have recently presented an exhaustive list of various methods to study the stability of DDEs [75]. In this section, using a Galerkin method [49, 55], we derive an ODE-based approximation for Eq. (4.13), thereby converting the DDE into a finite-dimensional ODE system. Equation (4.13) is converted into the following form:

$$\ddot{r}(t) + A_1\dot{r}(t) + A_2r(t) + A_3r(t - \tau) = 0. \quad (4.20)$$

The procedure for converting a DDE into a system of ODEs has already been reported in the literature [49, 55]; however, the procedure is repeated here for completeness. By defining the state variables  $\mathbf{r}(t) = [r(t), \dot{r}(t)]^T$  in Eq. (4.20), we get:

$$\dot{\mathbf{r}}(t) = \mathbf{A}\mathbf{r}(t) + \mathbf{B}\mathbf{r}(t - \tau). \quad (4.21)$$

In Eq. (4.21), the following time-shift transformation is introduced:

$$\mathbf{r}(t + s) = \mathbf{y}(s, t). \quad (4.22)$$

Differentiating Eq. (4.22) with respect to  $s$  and  $t$ , and using the chain rule, we obtain:

$$\frac{\partial \mathbf{y}(s, t)}{\partial t} = \frac{\partial \mathbf{y}(s, t)}{\partial s}, \quad -\tau \leq s \leq 0. \quad (4.23)$$

From Eq. (4.22), we have  $\mathbf{r}(t) = \mathbf{y}(0, t)$  and  $\mathbf{r}(t - \tau) = \mathbf{y}(-\tau, t)$ . Substituting these relations in Eq. (4.21), we get:

$$\left. \frac{\partial \mathbf{y}(s, t)}{\partial t} \right|_{s=0} = \mathbf{A}\mathbf{y}(0, t) + \mathbf{B}\mathbf{y}(-\tau, t). \quad (4.24)$$

In essence, we have converted the DDE given by Eq. (4.20) into an equivalent PDE (Eq. (4.23)) and its boundary condition (Eq. (4.24)). Now, we approximate the solution of Eq. (4.23) as follows:

$$y_i(s, t) = \sum_{j=1}^N \psi_j(s) z_{ij}(t) = \boldsymbol{\psi}(s)^T \mathbf{z}_i(t), \quad i = 1, 2. \quad (4.25)$$

Here  $\boldsymbol{\psi}(s) = [\psi_1(s), \psi_2(s), \dots, \psi_N(s)]^T$  and  $\mathbf{z}_i(t) = [z_{i1}(t), z_{i2}(t), \dots, z_{iN}(t)]^T$  are the basis functions and the independent coordinates, respectively. By defining  $\boldsymbol{\Psi}(s) \in \mathbb{R}^{2N \times 2}$  and  $\boldsymbol{\beta}(t) \in \mathbb{R}^{2N \times 1}$  as follows:

$$\boldsymbol{\Psi}(s) = \begin{bmatrix} \boldsymbol{\psi}(s) & \mathbf{0} \\ \mathbf{0} & \boldsymbol{\psi}(s) \end{bmatrix}, \quad \boldsymbol{\beta}(t) = [\mathbf{z}_1^T(t), \mathbf{z}_2^T(t)]^T, \quad (4.26)$$

Eq. (4.25) can be written as:

$$\mathbf{y}(s, t) = [\boldsymbol{\psi}^T(s) \mathbf{z}_1(t), \boldsymbol{\psi}^T(s) \mathbf{z}_2(t)]^T = \boldsymbol{\Psi}^T(s) \boldsymbol{\beta}(t). \quad (4.27)$$

Substituting Eq. (4.27) into Eq. (4.23), we get:

$$\boldsymbol{\Psi}^T(s) \dot{\boldsymbol{\beta}}(t) = \boldsymbol{\Psi}'(s)^T \boldsymbol{\beta}(t), \quad (4.28)$$

where  $\boldsymbol{\Psi}'(s)$  is the derivative of  $\boldsymbol{\Psi}(s)$  with respect to  $s$ . Pre-multiplying Eq. (4.28) by  $\boldsymbol{\Psi}(s)$  and integrating with respect to  $s$  over the domain  $[-\tau, 0]$ , we obtain the following:

$$\left( \int_{-\tau}^0 \boldsymbol{\Psi}(s) \boldsymbol{\Psi}^T(s) ds \right) \dot{\boldsymbol{\beta}}(t) = \left( \int_{-\tau}^0 \boldsymbol{\Psi}(s) \boldsymbol{\Psi}'(s)^T ds \right) \boldsymbol{\beta}(t). \quad (4.29)$$

Equation (4.29) can be rewritten as:

$$\mathbf{C}\dot{\boldsymbol{\beta}}(t) = \mathbf{D}\boldsymbol{\beta}(t), \quad (4.30)$$

where  $\mathbf{C}$  and  $\mathbf{D}$  are square, block-diagonal matrices of dimension  $2N$ , given by:

$$\mathbf{C} = \begin{bmatrix} \mathbf{C}^{(1)} & \mathbf{0} \\ \mathbf{0} & \mathbf{C}^{(2)} \end{bmatrix}^T, \quad \mathbf{D} = \begin{bmatrix} \mathbf{D}^{(1)} & \mathbf{0} \\ \mathbf{0} & \mathbf{D}^{(2)} \end{bmatrix}^T. \quad (4.31)$$

Submatrices  $\mathbf{C}^{(i)}$  and  $\mathbf{D}^{(i)}$  are defined as follows:

$$\mathbf{C}^{(i)} \triangleq \int_{-\tau}^0 \boldsymbol{\psi}_i(s) \boldsymbol{\psi}_i^T(s) ds, \quad \mathbf{D}^{(i)} \triangleq \int_{-\tau}^0 \boldsymbol{\psi}_i(s) \boldsymbol{\psi}_i'(s)^T ds, \quad i = 1, 2. \quad (4.32)$$

The matrix of boundary conditions, of dimension  $2 \times 2N$ , can be derived by substituting Eq. (4.27) into Eq. (4.24) as follows:

$$\boldsymbol{\Psi}^T(0) \dot{\boldsymbol{\beta}}(t) = [\mathbf{A}\boldsymbol{\Psi}^T(0) + \mathbf{B}\boldsymbol{\Psi}^T(-\tau)] \boldsymbol{\beta}(t). \quad (4.33)$$

Equations (4.30) and (4.33) can be combined as follows:

$$\mathbf{M}\dot{\boldsymbol{\beta}}(t) = \mathbf{K}\boldsymbol{\beta}(t). \quad (4.34)$$

Matrices  $\mathbf{M}$  and  $\mathbf{K}$  are of dimension  $2N \times 2N$ , and are obtained by replacing the  $N^{\text{th}}$  and  $2N^{\text{th}}$  rows of Eq. (4.30) with the  $1^{\text{st}}$  and  $2^{\text{nd}}$  rows of Eq. (4.33), respectively. Defining  $\mathbf{G} \triangleq \mathbf{M}^{-1}\mathbf{K}$ , Eq. (4.34) can be written as follows:

$$\dot{\boldsymbol{\beta}}(t) = \mathbf{G}\boldsymbol{\beta}(t). \quad (4.35)$$

The system of ODEs given by Eq. (4.35) approximate the DDE given by Eq. (4.20), and the eigenvalues ( $\hat{\lambda}_i$ ) of  $\mathbf{G}$  approximate the characteristic roots of Eq. (4.14). As  $N$  is increased, the eigenvalues of  $\mathbf{G}$  converge to the rightmost characteristic roots of Eq. (4.14) [49, 55]. The error  $E_i$ ,  $\forall i = \{1, 2, \dots, 2N\}$ , is defined as the absolute value of  $D(\hat{\lambda}_i)$  (Eq. (4.14)), obtained by substituting the eigenvalues of  $\mathbf{G}$  into Eq. (4.14). All  $\hat{\lambda}_i$  for which  $E_i < 10^{-4}$  are considered to be converged to the characteristic roots of Eq. (4.14). In this chapter, shifted Legendre polynomials are used to approximate

the solution (Eq. (4.25)) and are defined as follows:

$$\psi_1(s) = 1 \tag{4.36a}$$

$$\psi_2(s) = 1 + \frac{2s}{\tau} \tag{4.36b}$$

$$\psi_k(s) = \frac{(2k-3)\psi_2(s)\psi_{k-1}(s) - (k-2)\psi_{k-2}(s)}{k-1}, \quad k = 3, 4, \dots, N. \tag{4.36c}$$

In the literature, it is reported that shifted Legendre polynomials have shown good convergence properties [49]. The entries of matrices  $\mathbf{C}^{(p)}$  and  $\mathbf{D}^{(p)}$  can be expressed in closed form as follows:

$$\mathbf{C}_{ij}^{(p)} = \begin{cases} \frac{\tau}{2i-1}, & \text{if } i = j \\ 0, & \text{otherwise} \end{cases}, \quad \mathbf{D}_{ij}^{(p)} = \begin{cases} 2, & \text{if } i < j \text{ and } i + j \text{ is odd} \\ 0, & \text{otherwise} \end{cases}, \quad p = 1, 2. \tag{4.37}$$

where  $i = 1, 2, \dots, N$  and  $j = 1, 2, \dots, N$ . If we consider  $N$  terms in the series solution given by Eq. (4.25), approximately  $N/2$  eigenvalues of matrix  $\mathbf{G}$  converge to the rightmost roots of the characteristic polynomial (Eq. (4.14)). In this chapter, we use  $N = 100$  and this value of  $N$  was found to be sufficient for generating an accurate stability chart for Eq. (4.20).

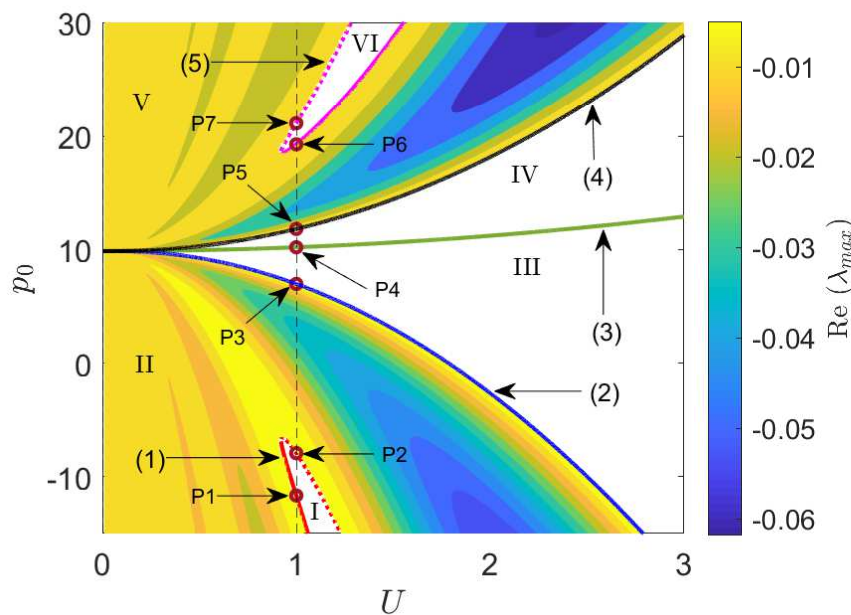


FIGURE 4.5: Stability chart in the  $[U, p_0]$  plane, generated using the Galerkin approximation method, with  $N = 100$ . Color contours indicate the damping present in the rightmost root.

Figure 4.5 shows the stability chart for Eq. (4.14) in the  $[U, p_0]$  plane, obtained

using the Galerkin approximation method. To generate the stability chart, the region of Fig. 4.5 has been discretized into  $300 \times 4500$  points. At each of these points, the eigenvalues of matrix  $\mathbf{G}$  (see Eq. (4.35)) are evaluated. If all the eigenvalues fall on the left half of complex plane, the system is considered to be stable; otherwise, it is considered unstable. All the white regions shown in Fig. 4.5 (i.e., I, III, IV, and VI) are unstable. The color contours in Fig. 4.5 indicate the damping present in the rightmost root in the stable region. It should be noted that for a retarded delay differential equation (RDDE), the decay rate will depend on the real parts of all the infinite roots. However, the contribution to the solution from the rightmost root is the highest and is the last to decay. Therefore, we have assumed the real part of rightmost root to be the damping in the system. The highest damping ( $\lambda$  furthest into the left half-plane) is present around  $U = 2.34$  and for  $p_0 = 30$ . Figure 4.5 must be contrasted with Fig. 4.3 as the boundary curves shown in these figures are same. From the stability chart, we can conclude that the zero equilibrium ( $\bar{q} = \bar{q}_1 = 0$ ) is stable only in region II. The buckled equilibrium at  $\bar{q} = \bar{q}_2$  exists in regions IV, V, and VI, but it is stable only in region V. An important observation from the stability chart is that curve 3, which separates regions III and IV, does not represent the critical curve for static bifurcation since the system is unstable in both regions III and IV.

TABLE 4.1: Values of  $p_{cr}$ ,  $\omega_{cr}$ ,  $\bar{\Gamma}$  (numerical),  $\Gamma$  (analytical), and relative error between the latter  $\hat{e} = \left(\frac{\bar{\Gamma}-\Gamma}{\Gamma}\right)$  expressed as a percentage, for different bifurcation points as shown in the stability chart (see Fig. 4.5).

| Point | $p_{cr}$ | $\omega_{cr}$ | $\bar{\Gamma} (\times 10^{-4})$ | $\Gamma (\times 10^{-4})$ | $\hat{e} (\%)$ |
|-------|----------|---------------|---------------------------------|---------------------------|----------------|
| $P_1$ | -11.652  | 1.285         | 5.7416                          | 5.7274                    | 0.2479         |
| $P_2$ | -7.923   | 1.175         | -6.6533                         | -6.6375                   | 0.2380         |
| $P_3$ | 6.978    | 0.445         | 144.5214                        | 144.5937                  | 0.0500         |
| $P_5$ | 11.822   | 0.445         | -289.5746                       | -288.7426                 | 0.2881         |
| $P_6$ | 19.273   | 1.175         | 13.2800                         | 13.2417                   | 0.2892         |
| $P_7$ | 21.137   | 1.285         | -11.3442                        | -11.3089                  | 0.3121         |

As discussed in Section 4.2, for a given flow velocity, from the stability chart, the axial tension  $P_A$  can be adjusted for maximum damping. For example, if the heat exchanger is operated at  $U = 2$ , the induced axial load can be selected to  $p_0 = -15$  for optimal damping of vibrations. It should be noted that with  $p_0 = -15$ , the beam settles at zero equilibrium.



Now, we study the distribution of the characteristic roots for different critical points in Fig. 4.5 along  $U = 1$ , shown by the dashed vertical line. Points  $P_1$ ,  $P_2$ , and  $P_3$  in Fig. 4.5 are the bifurcation points of zero equilibrium. Similarly,  $P_5$ ,  $P_6$ , and  $P_7$  are the bifurcation points of buckled equilibrium. The value of critical axial load  $p_{cr}$  and frequency  $\omega_{cr}$  at these points is shown in the second and third columns of Table 4.1, respectively.

Figures 4.6(a) – 4.6(f) show the 12 rightmost characteristic roots of Eq. (4.14) corresponding to points  $P_1$ ,  $P_2$ ,  $P_3$ ,  $P_5$ ,  $P_6$ , and  $P_7$ . It can be seen from Figs. 4.6(a) – 4.6(f) that the rightmost roots are purely imaginary indicating the possibility of Hopf bifurcation. In Fig. 4.7, the spectrum corresponding to point  $P_4$  is shown. It can be seen that there is a characteristic root at the origin, which is expected as this point falls on curve 3 in Fig. 4.5. However, the system is already unstable (see Fig. 4.7). Therefore,  $P_4$  is not a bifurcation point.

In Fig. 4.8, we show the real part of the rightmost root in the region  $-15 \leq p_0 \leq 10.207$  for the zero equilibrium ( $\bar{q} = \bar{q}_1 = 0$ ), represented by the red line. The blue dotted-line shows the real part of the rightmost root in the region  $10.207 \leq p_0 \leq 30$  for the buckled equilibrium ( $\bar{q} = \bar{q}_2$ ). We can clearly see from Fig. 4.8 that the real part of the rightmost root crosses the imaginary axis at points  $P_1$ ,  $P_2$ ,  $P_3$ ,  $P_5$ ,  $P_6$ , and  $P_7$  with non-zero slope ( $\bar{\Gamma}$ ) with respect to the parameter  $p_0$ . This clearly indicates the presence of a Hopf bifurcation. The value of  $\bar{\Gamma} = \text{Real}\left(\frac{d\lambda}{dp_0}\right)\Big|_{p_0=p_{cr}} \approx \text{Real}\left(\frac{\lambda|_{(p_{cr}+\sigma)} - \lambda|_{(p_{cr}-\sigma)}}{2\sigma}\right)$  at these points is shown in the fourth column of Table 4.1.

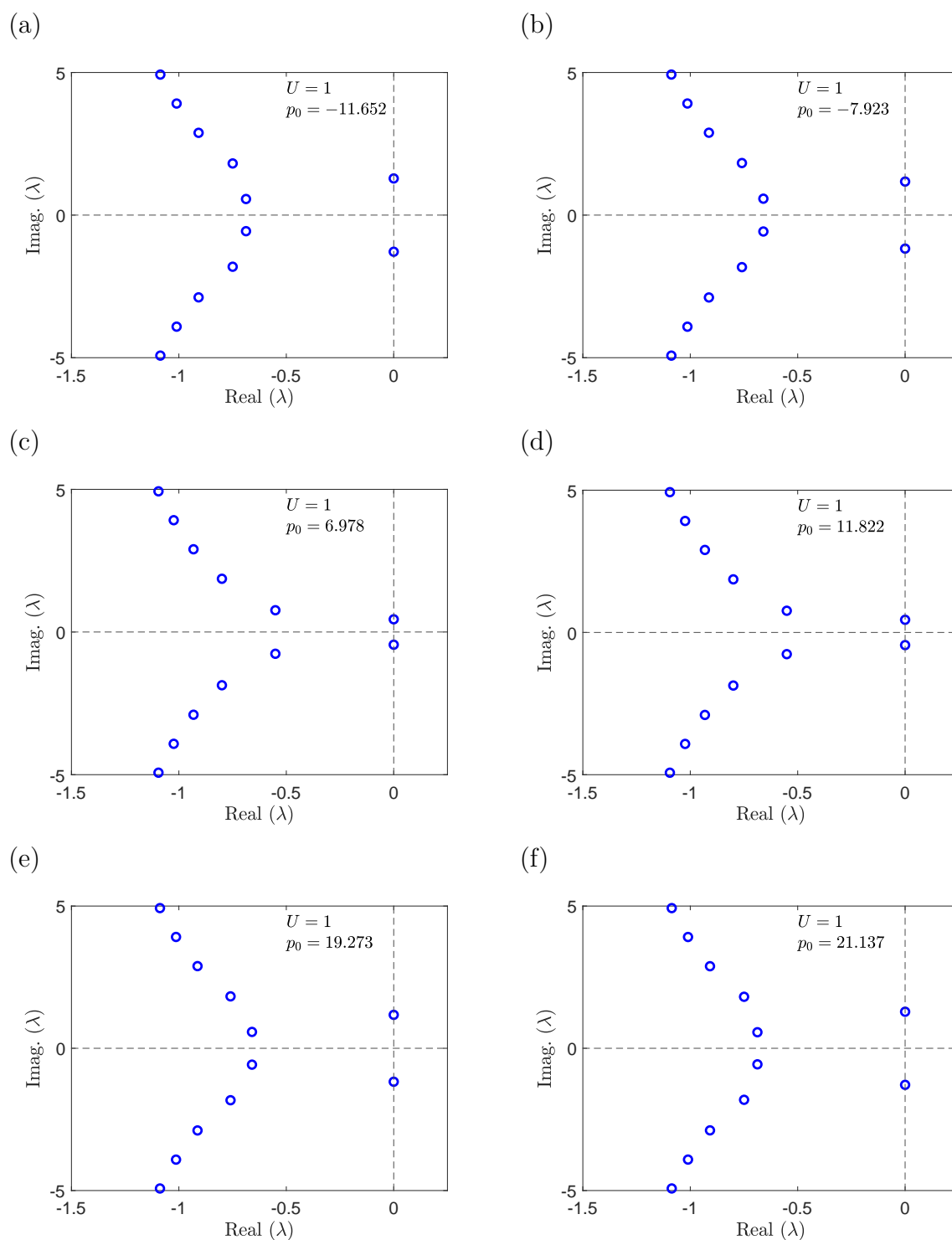


FIGURE 4.6: Characteristic roots of Eq. (4.14), obtained using Galerkin approximations for  $U = 1$  and for (a)  $p_0 = -11.652$ , (b)  $p_0 = -7.923$ , (c)  $p_0 = 6.978$ , (d)  $p_0 = 11.822$ , (e)  $p_0 = 19.273$ , and (f)  $p_0 = 21.137$ .

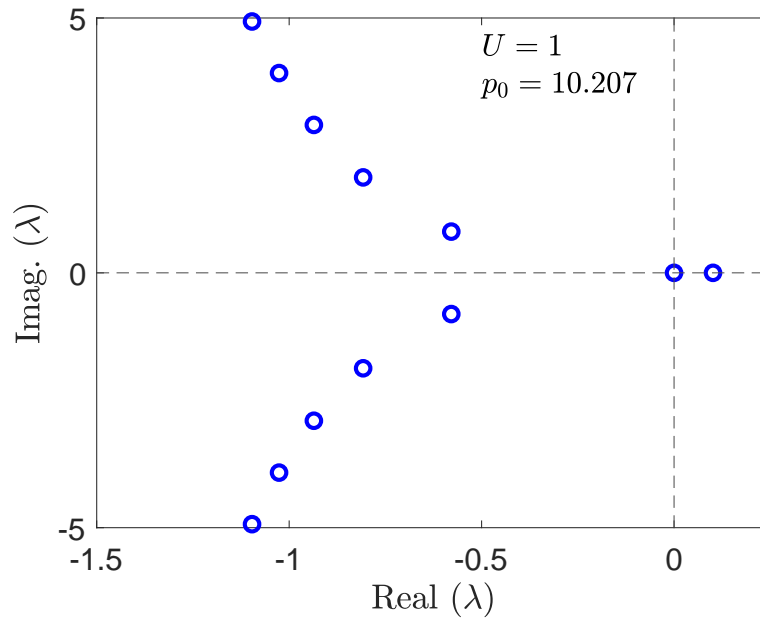


FIGURE 4.7: Characteristic roots of Eq. (4.14) obtained using Galerkin approximations for  $U = 1$  and for  $p_0 = 10.207$ .

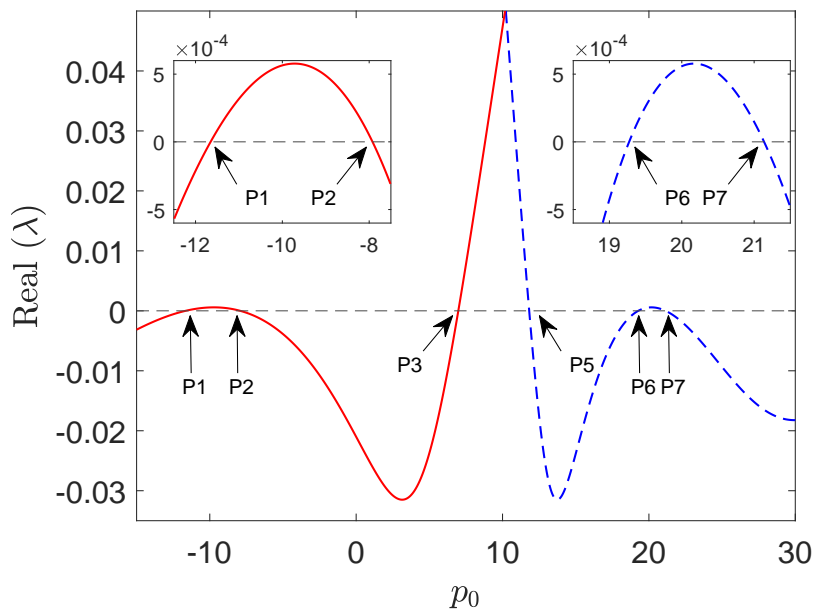


FIGURE 4.8: Variation of the real part of rightmost characteristic root of Eq. (4.14) for  $U = 1$  and for  $-15 \leq p_0 \leq 30$ .

## 4.4 Hopf bifurcation

In this section, the Hopf bifurcation of Eq. (4.12) is studied. Equation (4.12) is rewritten here for reference:

$$\ddot{r}(t) + (\alpha_1 + \alpha_2 U) \dot{r}(t) + \alpha_3 \left[ 1 - \frac{p_0}{\pi^2} \right] r(t) + 3\alpha_4 \bar{q}^2 r(t) + 3\alpha_4 \bar{q} r^2(t) + \alpha_4 r(t)^3 + \alpha_5 U^2 r(t - \tau) = 0. \quad (4.38)$$

From the stability chart (see Fig. 4.5), we can see that by fixing  $U$  (at 1) and increasing  $p_0$ , the stability of the equilibrium at  $r = 0$  switches when we cross curves 1 and 2. It should be noted that curves 1 and 2 in the stability chart correspond to the stability boundary for  $\bar{q} = \bar{q}_1 = 0$  in Eq. (4.12). Similarly, for a fixed value of  $U$ , the stability of the equilibrium at  $r = 0$  switches when we cross curves 4 and 5 in the stability chart. It should be noted that curves 4 and 5 in the stability chart correspond to the stability boundary for  $\bar{q} = \bar{q}_2$ , i.e., for the buckled equilibrium case of Eq. (4.12). In order to determine the nature of Hopf bifurcation (supercritical or subcritical), one must obtain the normal forms of Eq. (4.38) at the Hopf bifurcation points. The normal forms near the Hopf bifurcation can be obtained using the MMS [57] or the method of averaging [76, 77] or center manifold reduction [78]. These normal forms can be used to study the stability of the limit-cycles born out of Hopf bifurcation. In this section, the normal-form equations are obtained using the MMS.

### 4.4.1 Hopf bifurcation for the case of $\bar{q} = \bar{q}_1 = 0$

Substituting  $\bar{q} = \bar{q}_1 = 0$  into Eq. (4.38), we get:

$$\ddot{r}(t) + (\alpha_1 + \alpha_2 U) \dot{r}(t) + \alpha_3 \left[ 1 - \frac{p_0}{\pi^2} \right] r(t) + \alpha_4 r(t)^3 + \alpha_5 U^2 r(t - \tau) = 0. \quad (4.39)$$

The following parameters are now introduced into Eq. (4.39):

$$2\zeta = \alpha_1 + \alpha_2 U, \quad k_1 = \alpha_3, \quad k_2 = \frac{\alpha_3}{\pi^2}, \quad k_4 = \alpha_5 U^2. \quad (4.40)$$

Equation (4.39) now becomes:

$$\ddot{r}(t) + 2\zeta \dot{r}(t) + k_1 r(t) - k_2 p_0 r(t) + \alpha_4 r^3(t) + k_4 r(t - \tau) = 0. \quad (4.41)$$

Dropping the nonlinear term in Eq. (4.41) and introducing the parameters  $\zeta$ ,  $k_1$ ,  $k_2$  and  $k_4$  (Eq. (4.40)) into the characteristic equation of the linearized problem, we have:

$$D(\lambda, p_0) \equiv \lambda^2 + 2\zeta\lambda + k_1 - k_2p_0 + \frac{k_4}{e^{\lambda\tau}} = 0, \quad (4.42)$$

where  $\lambda$  is an implicit function of  $p_0$ . From the chain rule of differentiation, we have:

$$\frac{dD}{dp_0} = \frac{\partial D}{\partial p_0} + \frac{\partial D}{\partial \lambda} \frac{d\lambda}{dp_0} = 0. \quad (4.43)$$

Solving Eq. (4.43) for  $\frac{d\lambda}{dp_0}$ , we get

$$\frac{d\lambda}{dp_0} = -\frac{\partial D}{\partial p_0} \left( \frac{\partial D}{\partial \lambda} \right)^{-1} = \frac{k_2}{2\lambda + 2\zeta - k_4 e^{-\lambda\tau}}. \quad (4.44)$$

At a Hopf bifurcation, we have to show that  $\Gamma = \text{Real} \left( \frac{d\lambda}{dp_0} \right) \Big|_{p_0=p_{cr}, \lambda=j\omega_{cr}} \neq 0$ . Substituting  $p_0 = p_{cr}$  and  $\lambda = j\omega_{cr}$  in Eq. (4.44) and using the identity  $e^{-j\omega_{cr}\tau} = \cos(\omega_{cr}\tau) - j\sin(\omega_{cr}\tau)$ , we get:

$$\Gamma = \frac{k_2(-2\zeta + k_4\tau \cos(\omega_{cr}\tau))}{-4\zeta^2 + 4\zeta k_4\tau \cos(\omega_{cr}\tau) - k_4^2\tau^2 - 4\omega_{cr}^2 - 4\omega_{cr}k_4\tau \sin(\omega_{cr}\tau)}. \quad (4.45)$$

Substituting  $\sin(\omega_{cr}\tau)$  and  $\cos(\omega_{cr}\tau)$  obtained from Eqs. (4.16a) and (4.16b) in Eq. (4.45), we get:

$$\Gamma = \frac{k_2(2\zeta - \tau\omega_{cr}^2 + \tau k_1 - \tau k_2 p_{cr})}{4(\zeta\tau + 1)\omega_{cr}^2 + 4\zeta^2 + 4\zeta\tau k_1 - 4\zeta\tau k_2 p_{cr} + k_4^2\tau^2}. \quad (4.46)$$

It can be seen from Table 4.1 that the analytically predicted values of  $\Gamma$  (velocity of root crossing) at the Hopf bifurcation points are in close agreement with those obtained numerically from Galerkin approximations. At points  $P_1$ ,  $P_2$ , and  $P_3$ , we have  $\Gamma \neq 0$ . This guarantees the occurrence of the Hopf bifurcation at these points. It should be noted that  $\Gamma > 0$  indicates the crossing of purely imaginary roots from left to right (stable to unstable) in the complex plane. Conversely,  $\Gamma < 0$  indicates the crossing of purely imaginary roots from right to left (unstable to stable) in the complex plane.

As the focus of this section is to study the motion around the Hopf bifurcation points, we perturb the parameter  $p_0$  using a detuning parameter  $\Delta$ . Substituting  $p_0 = p_{cr} + \epsilon\Delta$ ,  $\kappa = k_1 - k_2p_{cr}$  and  $k_3 = \alpha_4/\epsilon$  in Eq. (4.41), we get:

$$\ddot{r}(t) + 2\zeta\dot{r}(t) + \kappa r(t) + k_4 r(t - \tau) + \epsilon[k_3 r^3(t) - k_2\Delta r(t)] = 0. \quad (4.47)$$

Using the MMS for DDEs as proposed by Das and Chatterjee [57], the solution  $r(t)$  of Eq. (4.47) is expanded as follows:

$$r(t) = r(t, T_0) = r_0(t, T_0) + \epsilon r_1(t, T_0) + \dots \quad (4.48)$$

In Eq. (4.48),  $t = \epsilon^0 t$  is the actual time-scale, and  $T_0 = \epsilon^1 t$  is the slow time-scale. The time-delay term  $r(t - \tau)$  is expanded as follows:

$$r(t - \tau) = r_0(t - \tau, T_0) + \epsilon \left( r_1(t - \tau, T_0) - \tau \frac{\partial r_0(t - \tau, T_0)}{\partial T_0} \right) + \dots \quad (4.49)$$

Upon substituting Eqs. (4.48) and (4.49) into Eq. (4.47), the terms with coefficients  $\epsilon^0$  and  $\epsilon^1$  respectively are collected. Equating them each to zero, the following equations are obtained:

$$\mathcal{O}(\epsilon^0) : \frac{\partial^2 r_0}{\partial t^2} + 2\zeta \frac{\partial r_0}{\partial t} + \kappa r_0 + k_4 r_0(t - \tau) = 0, \quad (4.50a)$$

$$\begin{aligned} \mathcal{O}(\epsilon^1) : \frac{\partial^2 r_1}{\partial t^2} + 2\zeta \frac{\partial r_1}{\partial t} + \kappa r_1 + k_4 r_1(t - \tau) - k_2 \Delta r_0 \\ + 2\zeta \frac{\partial r_0}{\partial T_0} - k_4 \tau \frac{\partial r_0(t - \tau)}{\partial T_0} + 2 \frac{\partial^2 r_0}{\partial T_0 \partial t} + k_3 r_0^3 = 0. \end{aligned} \quad (4.50b)$$

At the Hopf bifurcation point, the transient solution of Eq. (4.50a) decays with time since the characteristics roots lie on the left half of the complex plane (see Figs. 4.6(a), 4.6(b), and 4.6(c)). The only solution that persists is the one due to the roots lying on the imaginary axis, with frequency  $\omega_{cr}$ . Therefore, the solution of Eq. (4.50a) is assumed as follows:

$$r_0(t, T_0) = A(T_0) \sin(\omega_{cr} t) + B(T_0) \cos(\omega_{cr} t). \quad (4.51)$$

Substituting Eq. (4.51) in Eq. (4.50b), we get:

$$\begin{aligned} \frac{\partial^2 r_1}{\partial t^2} + 2\zeta \frac{\partial r_1}{\partial t} + \kappa r_1 + k_4 r_1(t - \tau) + Z_1 \cos(3\omega_{cr} t) + Z_2 \sin(3\omega_{cr} t) \\ + Z_3 \cos(\omega_{cr} t) + Z_4 \sin(\omega_{cr} t) = 0, \end{aligned} \quad (4.52)$$

where  $Z_1$ ,  $Z_2$ ,  $Z_3$ , and  $Z_4$  are given as follows:

$$Z_1 = \frac{1}{4}k_3B^3 - \frac{3}{4}k_3A^2B, \quad (4.53a)$$

$$Z_2 = \frac{1}{4}k_3A^3 + \frac{3}{4}k_3AB^2, \quad (4.53b)$$

$$Z_3 = (k_4\tau \sin(\omega_{cr}\tau) + 2\omega) \frac{\partial A}{\partial T_0} + (2\zeta - k_4\tau \cos(\omega_{cr}\tau)) \frac{\partial B}{\partial T_0} + \frac{3}{4}k_3A^2B + \frac{3}{4}k_3B^3 - k_2\Delta B, \quad (4.53c)$$

$$Z_4 = (2\zeta - k_4\tau \cos(\omega_{cr}\tau)) \frac{\partial A}{\partial T_0} - (2\omega_{cr} + k_4\tau \sin(\omega_{cr}\tau)) \frac{\partial B}{\partial T_0} + \frac{3}{4}k_3AB^2 + \frac{3}{4}k_3A^3 - k_2\Delta A. \quad (4.53d)$$

The terms with coefficients  $Z_3$  and  $Z_4$  cause resonance in Eq. (4.52) and are known as secular terms. Since the solution of  $r(t)$  is bounded, these terms should vanish. Setting  $Z_3 = 0$  and  $Z_4 = 0$ , the expressions for  $\frac{\partial A}{\partial T_0}$  and  $\frac{\partial B}{\partial T_0}$  are obtained. Then, using the relations  $\dot{A} = \epsilon \frac{\partial A}{\partial T_0} + \mathcal{O}(\epsilon^2)$  and  $\dot{B} = \epsilon \frac{\partial B}{\partial T_0} + \mathcal{O}(\epsilon^2)$ , the complex amplitude modulation relations are obtained as follows:

$$\dot{A}(t) = \epsilon \left( \frac{A_1 \sin(\omega_{cr}\tau) + A_2 \cos(\omega_{cr}\tau) + A_3}{4A_4} \right), \quad (4.54a)$$

$$\dot{B}(t) = \epsilon \left( \frac{B_1 \sin(\omega_{cr}\tau) + B_2 \cos(\omega_{cr}\tau) + B_3}{4B_4} \right). \quad (4.54b)$$

In Eq. (4.54a), the variables  $A_1$  to  $A_4$  are given by:

$$A_1 = 3k_4\tau k_3B^3 - 4Bk_4\tau k_2\Delta + 3Bk_4\tau k_3A^2, \quad (4.55a)$$

$$A_2 = -3k_3AB^2k_4\tau - 3k_3A^3k_4\tau + 4k_2\Delta Ak_4\tau, \quad (4.55b)$$

$$A_3 = 6k_3AB^2\zeta + 6k_3A^3\zeta - 8k_2\Delta A\zeta + 6\omega_{cr}k_3B^3 - 8B\omega_{cr}k_2\Delta + 6B\omega_{cr}k_3A^2, \quad (4.55c)$$

$$A_4 = -k_4^2\tau^2 + 4k_4\tau \cos(\omega_{cr}\tau)\zeta - 4\zeta^2 - 4\omega_{cr}^2 - 4\omega_{cr}k_4\tau \sin(\omega_{cr}\tau). \quad (4.55d)$$

In Eq. (4.54b), the variables  $B_1$  to  $B_4$  are given as follows:

$$B_1 = -3k_3AB^2k_4\tau - 3k_3A^3k_4\tau + 4k_2\Delta Ak_4\tau, \quad (4.56a)$$

$$B_2 = 4Bk_4\tau k_2\Delta - 3k_4\tau k_3B^3 - 3Bk_4\tau k_3A^2, \quad (4.56b)$$

$$B_3 = -6\omega_{cr}k_3A^3 + 6k_3B^3\zeta - 8Bk_2\Delta\zeta - 6\omega_{cr}k_3AB^2 + 8\omega_{cr}k_2\Delta A + 6Bk_3A^2\zeta, \quad (4.56c)$$

$$B_4 = -k_4^2\tau^2 + 4k_4\tau \cos(\omega_{cr}\tau)\zeta - 4\zeta^2 - 4\omega_{cr}^2 - 4\omega_{cr}k_4\tau \sin(\omega_{cr}\tau). \quad (4.56d)$$

Now, using the polar transformation  $A(t) = R(t) \sin(\theta(t))$  and  $B(t) = R(t) \cos(\theta(t))$  in

Eqs. (4.54a) and (4.54b), the amplitude and phase modulation equations are obtained as follows:

$$\dot{R}(t) = \epsilon e_1(4k_2\Delta R(t) - 3k_3R(t)^3), \quad (4.57a)$$

$$\dot{\theta}(t) = \epsilon e_2(4k_2\Delta - 3k_3R(t)^2), \quad (4.57b)$$

where  $e_1$  and  $e_2$  are defined as follows:

$$e_1 = (k_4\tau \cos(\omega_{cr}\tau) - 2\zeta)e_3, \quad (4.58a)$$

$$e_2 = (2\omega_{cr} + k_4\tau \sin(\omega_{cr}\tau))e_3. \quad (4.58b)$$

Here,  $e_3 = 4(-k_4^2\tau^2 + 4k_4\tau \cos(\omega_{cr}\tau)\zeta - 4\zeta^2 - 4\omega_{cr}^2 - 4\omega_{cr}k_4\tau \sin(\omega_{cr}\tau))$ . The approximate solution of the DDE presented in Eq. (4.47), accurate to  $\mathcal{O}(\epsilon^0)$ , can now be written using the normal-form equations (Eqs. (4.57a) and (4.57b)) as follows:

$$r(t) \approx R(t) \cos(\omega_{cr}t + \theta(t)), \quad (4.59a)$$

$$\dot{r}(t) \approx \dot{R}(t) \cos(\omega_{cr}t + \theta(t)) - R(t) \sin(\omega_{cr}t + \theta(t))(\omega_{cr} + \dot{\theta}(t)). \quad (4.59b)$$

#### 4.4.1.1 Hopf bifurcation at point $P_1$

Substituting the values of  $p_{cr}$  and  $\omega_{cr}$  for point  $P_1$  (see Table 4.1) in Eqs. (4.57a) and (4.57b), we get:

$$\dot{R}(t) = 5.7073 \times 10^{-4}(\epsilon\Delta)R(t) - 6.1730 \times 10^{-3}R(t)^3, \quad (4.60a)$$

$$\dot{\theta}(t) = 2.8203 \times 10^{-2}(\epsilon\Delta) - 30.5050 \times 10^{-2}R(t)^2. \quad (4.60b)$$

Figure 4.9(a) shows the local bifurcation diagram (supercritical Hopf bifurcation) obtained from Eq. (4.60a). In all the bifurcation diagrams reported in this chapter, solid lines are used to represent stable solutions, while dashed lines are used to represent the unstable solutions. Also, non-zero equilibrium solutions ( $R \neq 0$ ) correspond to the amplitudes of the periodic solutions that arise from the Hopf bifurcation. The blue circles in Fig. 4.9(a) are the amplitudes of the periodic solutions obtained by integrating Eq. (4.47) using the *dde23* MATLAB solver. Equation (4.47) is a DDE for which the history function must be defined for numerical integration. First, with initial conditions  $R(0)$  and  $\theta(0)$ , the set of ODEs given by Eqs. (4.60a) and (4.60b) are solved. Then,  $r(t)$  (Eq. (4.59a)) and  $\dot{r}(t)$  (Eq. (4.59b)) obtained for the interval  $[0, \tau]$  ( $\tau = \frac{2\pi}{\omega}$ ) is given as the history function for Eq. (4.47). Figures 4.9(b) (for  $\epsilon\Delta = -0.1$ ) and 4.9(c) (for  $\epsilon\Delta = 0.1$ ) show  $R(t)$  obtained using Eq. (4.60a) (red



line) and the system response  $r(t)$ , obtained by integrating Eq. (4.47) using the *dde23* MATLAB solver (blue line).

Figures 4.9(a) and 4.9(b) indicate that for  $\epsilon\Delta < 0$ , the system settles at the zero equilibrium (solid black line in Fig. 4.9(a)) for any initial condition. For  $\epsilon\Delta > 0$  (see Figs. 4.9(a) and 4.9(c)), the system settles into a periodic motion whose amplitude is given by  $R^*$  corresponding to the value of  $\epsilon\Delta$ .

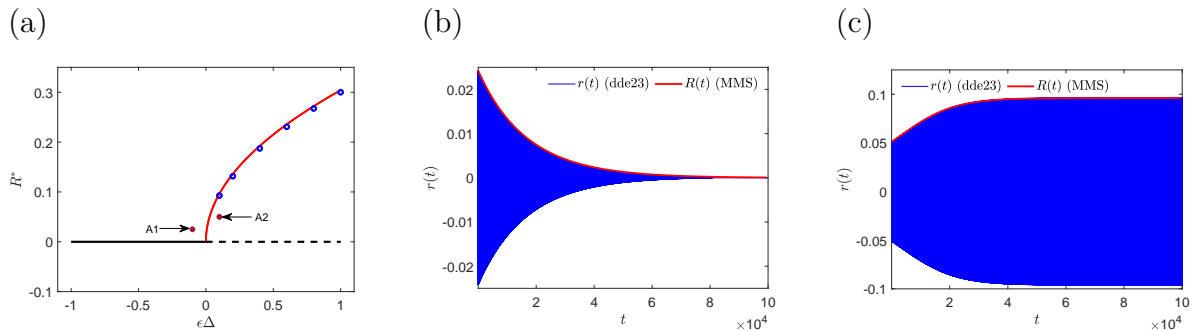


FIGURE 4.9: (a) Local bifurcation diagram at point  $P_1$ . System response at local bifurcation point  $P_1$  for (b)  $\epsilon\Delta = -0.1$  with initial conditions for Eqs. (4.60a) and (4.60b) given by point A1 in Fig. 4.9(a) and (c)  $\epsilon\Delta = 0.1$  with initial conditions for Eqs. (4.60a) and (4.60b) given by point A2 in Fig. 4.9(a).

#### 4.4.1.2 Hopf bifurcation at point $P_2$

Substituting the values of  $p_{cr}$  and  $\omega_{cr}$  for point  $P_2$  (see Table 4.1) in Eqs. (4.57a) and (4.57b), we get:

$$\dot{R}(t) = -6.7009 \times 10^{-4}(\epsilon\Delta)R(t) + 7.2477 \times 10^{-3}R(t)^3, \quad (4.61a)$$

$$\dot{\theta}(t) = 3.0835 \times 10^{-2}(\epsilon\Delta) - 33.3519 \times 10^{-2}R(t)^2. \quad (4.61b)$$

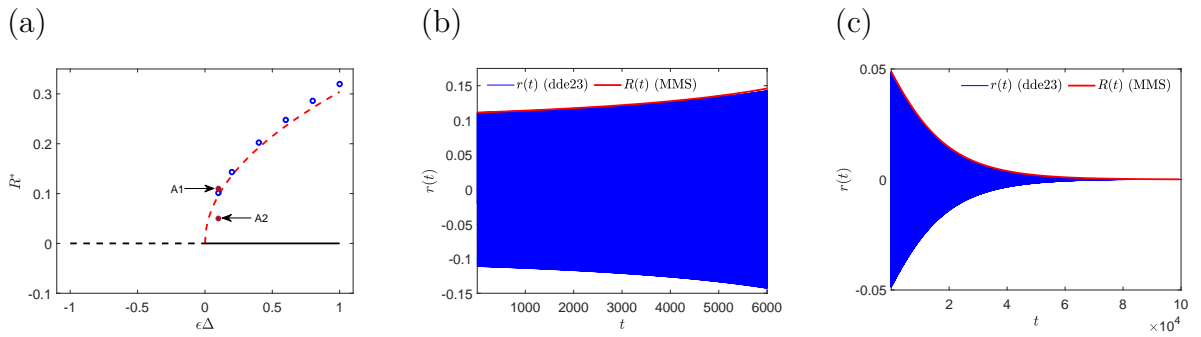


FIGURE 4.10: (a) Local-bifurcation diagram at point  $P_2$ . System response at local bifurcation point  $P_2$  for  $\epsilon\Delta = 0.1$  with initial conditions for Eqs. (4.61a) and (4.61b) given in Fig. 4.10(a) by point (b) A1 and (c) A2.

Figure 4.10(a) shows the local bifurcation diagram (subcritical Hopf bifurcation) obtained from Eq. (4.61a). For a given  $\epsilon\Delta$ , the amplitude of unstable periodic solutions is obtained from Eq. (4.47) as follows. We numerically integrate Eq. (4.47) for increasing values of constant history function and track the equilibrium solution. The critical value of the magnitude of the history function, above which the equilibrium will not approach zero, is considered to be the magnitude of the unstable limit cycle (blue circle). Figure 4.10(b) shows  $R(t)$  obtained using Eq. (4.61a) (red line) and the system response  $r(t)$  obtained by integrating Eq. (4.47) using the *dde23* MATLAB solver (blue line). Both cases are for  $\epsilon\Delta = 0.1$  and for the magnitude of history function given by point A1 in Fig. 4.10(a). Figure 4.10(c) shows the same physical quantities for the magnitude of the history function given by point A2 in Fig. 4.10(a).

Figures 4.10(a) and 4.10(b) indicate that for a given value of  $\epsilon\Delta (> 0)$ , any initial condition greater than  $R^*$  results in a diverging solution. Conversely, for a given value of  $\epsilon\Delta (> 0)$ , any initial condition less than  $R^*$  (see Figs. 4.10(a) and 4.10(c)) results in the system settling at the zero equilibrium (solid black line in Fig. 4.10(a)).

#### 4.4.1.3 Hopf bifurcation at point $P_3$

Substituting the values of  $p_{cr}$  and  $\omega_{cr}$  for point  $P_3$  (see Table 4.1) in Eqs. (4.57a) and (4.57b), we get:

$$\dot{R}(t) = 144.5864 \times 10^{-4}(\epsilon\Delta)R(t) - 156.3844 \times 10^{-3}R(t)^3, \quad (4.62a)$$

$$\dot{\theta}(t) = 7.8807 \times 10^{-2}(\epsilon\Delta) - 85.2384 \times 10^{-2}R(t)^2. \quad (4.62b)$$

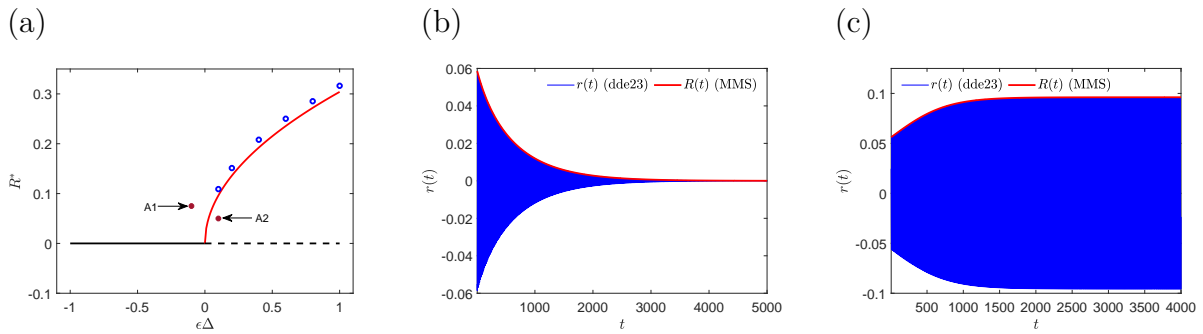


FIGURE 4.11: (a) Local bifurcation diagram at point  $P_3$ . System response at local bifurcation point  $P_3$  for (b)  $\epsilon\Delta = -0.1$  with initial conditions for Eqs. (4.62a) and (4.62b) given by point A1 in Fig. 4.11(a) and (c)  $\epsilon\Delta = 0.1$  with initial conditions for Eqs. (4.62a) and (4.62b) given by point A2 in Fig. 4.11(a).

Figure 4.11(a) shows the local bifurcation diagram (supercritical Hopf bifurcation) obtained from Eq. (4.62a). Figures 4.11(a), 4.11(b) and 4.11(c) are similar to Figs. 4.9(a), 4.9(b) and 4.9(c), except that these results are for the bifurcation point  $P_3$ . Figures 4.11(a) and 4.11(b) indicate that for  $\epsilon\Delta < 0$ , the system settles at the zero equilibrium (solid black line in Fig. 4.11(a)) for any initial condition. For  $\epsilon\Delta > 0$  (see Figs. 4.11(a) and 4.11(c)), the system settles into a periodic motion whose amplitude is given by  $R^*$  corresponding to the value of  $\epsilon\Delta$ .

It can be seen from Figs. 4.9, 4.10 and 4.11 that both the transient and the steady-state solutions of the normal-form equation obtained using the MMS, match closely with the results from direct numerical integration.

#### 4.4.2 Hopf bifurcation for the case of $\bar{q} = \bar{q}_2$

To study the Hopf bifurcation at buckled equilibrium ( $\bar{q} = \bar{q}_2$ ), we substitute the value of  $\bar{q}_2$  from Eq. (4.10) into Eq. (4.38). It should be noted that the “ $\pm$ ” sign in front of the expression for  $\bar{q}_2$  in Eq. (4.10) corresponds to the upward/downward buckled configuration of the beam. Here, we study the bifurcation corresponding to the upward configuration (+ve sign). Due to the symmetric nature of the buckling problem, the results are equally valid for the downward configuration (–ve sign). It must be noted that the underlying assumption in this analysis is that the buckling and fluid-elastic instabilities are in the same plane and phase. Therefore, it is implicit in this analysis that buckling, which is predominantly attributed to axial loads, and fluid forces are coupled.

The characteristic equation corresponding to the linearized version of Eq. (4.38)

around the equilibrium  $\bar{q} = \bar{q}_2$  is given by:

$$D(\lambda, p_0) = \lambda^2 + 2\zeta\lambda - 2k_1 + 2k_2p_0 - 3k_4 + k_4e^{-\lambda\tau} = 0. \quad (4.63)$$

The characteristic equation  $D(\lambda, p_0)$  satisfies Eq. (4.43); therefore, we have:

$$\frac{d\lambda}{dp_0} = \frac{-2k_2}{2\lambda + 2\zeta - k_4\tau e^{-\lambda\tau}}. \quad (4.64)$$

At the Hopf bifurcation point we have  $p_0 = p_{cr}$  and  $\lambda = j\omega_{cr}$ . Substituting these values in Eq. (4.64) we get:

$$\left. \frac{d\lambda}{dp_0} \right|_{p_0=p_{cr}, \lambda=j\omega_{cr}} = \frac{-2k_2}{2j\omega_{cr} + 2\zeta - k_4\tau e^{-j\omega_{cr}\tau}}. \quad (4.65)$$

With  $\Gamma = \text{Real}\left(\left. \frac{d\lambda}{dp_0} \right|_{p_0=p_{cr}, \lambda=j\omega_{cr}}\right)$ , we have:

$$\Gamma = \frac{-2k_2(-2\zeta + k_4\tau \cos(\omega_{cr}\tau))}{-4\zeta^2 + 4\zeta k_4\tau \cos(\omega_{cr}\tau) - k_4^2\tau^2 - 4\omega_{cr}^2 - 4\omega_{cr}k_4\tau \sin(\omega_{cr}\tau)}. \quad (4.66)$$

Substituting  $\sin(\omega_{cr}\tau)$  and  $\cos(\omega_{cr}\tau)$  obtained from Eqs. (4.18a) and (4.18b) in Eq. (4.66), we get:

$$\Gamma = \frac{-2k_2(-2\zeta + \tau(\omega^2 + 2k_1 - 2k_2p_0 + 3k_4))}{-4\zeta + 4\zeta\tau(\omega_{cr}^2 + 2k_1 - 2k_2p_0 + 3k_4) - k_4^2\tau^2 - 4\omega_{cr}^2 - 8\omega_{cr}^2\tau\zeta}. \quad (4.67)$$

The velocity of root-crossing ( $\Gamma$ ), calculated from Eq. (4.67), at points  $P_5$ ,  $P_6$ , and  $P_7$  (Fig. 4.5) is shown in the fourth column of Table 4.1. It can be seen from Table 4.1 that the analytically predicted values of  $\Gamma$  at the Hopf bifurcation points are in close agreement with those obtained numerically using Galerkin approximations. Furthermore, at the critical points ( $P_5$ ,  $P_6$ , and  $P_7$ ), we have  $\Gamma \neq 0$  in both cases.

Next, the normal form equations for Eq. (4.38), around the Hopf bifurcation points for the equilibrium at  $\bar{q} = \bar{q}_2$ , are derived. As there is a quadratic nonlinearity in Eq. (4.38), we substitute  $p_0 = p_{cr} + \epsilon^2\Delta$  and  $\alpha_4 = \epsilon^2k_3$  in Eq. (4.38) to obtain the normal form near the Hopf bifurcation point. Substituting the parameters  $\zeta$ ,  $k_1$ ,  $k_2$ ,  $k_4$  (as defined in Eq. (4.40)),  $p_0$  and  $\alpha_4$  in Eq. (4.38), we obtain:

$$\ddot{r}(t) + 2\zeta\dot{r}(t) + [k_1 - (p_{cr} + \epsilon^2\Delta)k_2 + 3\epsilon^2k_3\bar{q}_2^2]r(t) + 3\epsilon^2k_3\bar{q}_2r(t)^2 + \epsilon^2k_3r(t)^3 + k_4r(t-\tau) = 0. \quad (4.68)$$

Substituting the parameters  $k_1, k_2, k_3, k_4, \epsilon^2$  and  $\Delta$  in Eq. (4.10), we get:

$$\bar{q}_2 = \sqrt{\frac{-\alpha_3[1 - \frac{p_0}{\pi^2}] - \alpha_5 U^2}{\alpha_4}} = \sqrt{\frac{-k_4 - k_1 + k_2 p_{cr} + k_2 \epsilon^2 \Delta}{\epsilon^2 k_3}}. \quad (4.69)$$

Substituting Eq. (4.69) into Eq. (4.68), we get:

$$\begin{aligned} \ddot{r}(t) + 2\zeta\dot{r}(t) + (2k_2 p_{cr} - 2k_1 - 3k_4 + 2k_2 \epsilon^2 \Delta)r(t) + \epsilon^2 k_3 r(t)^3 \\ + 3\epsilon \sqrt{k_3(-k_4 - k_1 + k_2 p_{cr} + k_2 \epsilon^2 \Delta)}r(t)^2 + k_4 r(t - \tau) = 0. \end{aligned} \quad (4.70)$$

Next, expanding the square-root term in Eq. (4.70) using the Taylor series around  $\epsilon = 0$ , we get:

$$\sqrt{k_3(-k_4 - k_1 + k_2 p_{cr} + k_2 \epsilon^2 \Delta)} \approx a_1 - a_2 \epsilon^2 \Delta, \quad (4.71)$$

where  $a_1 = \sqrt{-k_3(k_4 + k_1 - k_2 p_{cr})}$  and  $a_2 = \frac{1}{2} \frac{\sqrt{-k_3(k_4 + k_1 - k_2 p_{cr})} k_2}{k_4 + k_1 - k_2 p_{cr}}$ . Substituting Eq. (4.71) into Eq. (4.70), we get:

$$\ddot{r}(t) + 2\zeta\dot{r}(t) + (a_3 + a_4 \epsilon^2 \Delta)r(t) + 3\epsilon(a_1 - a_2 \epsilon^2 \Delta)r(t)^2 + \epsilon^2 k_3 r(t)^3 + k_4 r(t - \tau) = 0, \quad (4.72)$$

where  $a_3 = 2k_2 p_{cr} - 2k_1 - 3k_4$  and  $a_4 = 2k_2$ . Now introducing the new time scales  $T_0 = \epsilon^1 t$  and  $T_1 = \epsilon^2 t$ ,  $r(t)$  is expanded as follows:

$$r(t) = r(t, T_0, T_1) = r_0(t, T_0, T_1) + \epsilon r_1(t, T_0, T_1) + \epsilon^2 r_2(t, T_0, T_1) + \dots \quad (4.73)$$

In Eq. (4.73),  $t = \epsilon^0 t$  is the actual time-scale;  $T_0$  and  $T_1$  are the slow time-scales. The time-delay term  $r(t - \tau)$  is expanded up to  $\mathcal{O}(\epsilon^2)$  using the Taylor series similar to Eq. (4.49). Upon substituting the expressions for  $r(t - \tau)$  and  $r(t)$  in Eq. (4.72), terms with coefficients of  $\epsilon^0, \epsilon^1$  and  $\epsilon^2$  are collected and are each equated to zero to obtain the following equations :

$$\mathcal{O}(\epsilon^0) : \frac{\partial^2 r_0}{\partial t^2} + 2\zeta \frac{\partial r_0}{\partial t} + a_3 r_0 + k_4 r_0(t - \tau) = 0, \quad (4.74a)$$

$$\begin{aligned} \mathcal{O}(\epsilon^1) : \frac{\partial^2 r_1}{\partial t^2} + 2\zeta \frac{\partial r_1}{\partial t} + a_3 r_1 + k_4 r_1(t - \tau) \\ = \tau k_4 \frac{\partial r_0(t - \tau)}{\partial T_0} - 2 \frac{\partial^2 r_0}{\partial T_0 \partial t} - 2\zeta \frac{\partial r_0}{\partial T_0} - 3a_1 r_0^2, \end{aligned} \quad (4.74b)$$

$$\mathcal{O}(\epsilon^2) : \frac{\partial^2 r_2}{\partial t^2} + 2\zeta \frac{\partial r_2}{\partial t} + a_3 r_2 + k_4 r_2(t - \tau) = K_1 + K_2 + K_3 - 6r_0 r_1 a_1, \quad (4.74c)$$

where  $K_1$ ,  $K_2$  and  $K_3$  are given as follows:

$$K_1 = -\left(a_4\Delta r_0 + k_3r_0^3 + 2\frac{\partial^2 r_0}{\partial T_1 \partial t} + \frac{\partial^2 r_0}{\partial T_0^2}\right), \quad (4.75a)$$

$$K_2 = -\left(2\zeta\frac{\partial r_0}{\partial T_1} - k_4\tau\frac{\partial r_0(t-\tau)}{\partial T_1} + \frac{1}{2}\tau^2k_4\frac{\partial^2 r_0(t-\tau)}{\partial T_0^2}\right), \quad (4.75b)$$

$$K_3 = -\left(2\frac{\partial^2 r_1}{\partial T_0 \partial t} + 2\zeta\frac{\partial r_1}{\partial T_0} - k_4\tau\frac{\partial r_1(t-\tau)}{\partial T_0}\right). \quad (4.75c)$$

Since the only non-decaying solution at the Hopf bifurcation point is the one due to the roots lying on the imaginary axis with frequency  $\omega_{cr}$ , the solution of Eq. (4.74a) can be written as follows:

$$r_0(t, T_0, T_1) = A(T_0, T_1) \cos(\omega_{cr}t) + B(T_0, T_1) \sin(\omega_{cr}t). \quad (4.76)$$

Substituting Eq. (4.76) into Eq. (4.74b), we get:

$$\begin{aligned} \frac{\partial^2 r_1}{\partial t^2} + 2\zeta\frac{\partial r_1}{\partial t} + a_3r_1 + k_4r_1(t-\tau) \\ = -Z_5 \cos(\omega_{cr}t) - Z_6 \sin(\omega_{cr}t) - Z_7 \cos(2\omega_{cr}t) - Z_8 \sin(2\omega_{cr}t) - Z_9, \end{aligned} \quad (4.77)$$

where  $Z_5$ ,  $Z_6$ ,  $Z_7$ ,  $Z_8$ , and  $Z_9$  are given by:

$$Z_5 = -k_4\tau\frac{\partial A}{\partial T_0} \cos(\omega_{cr}\tau) + k_4\tau\frac{\partial B}{\partial T_0} \sin(\omega_{cr}\tau) + 2\zeta\frac{\partial A}{\partial T_0} + 2\frac{\partial B}{\partial T_0}\omega_{cr}, \quad (4.78a)$$

$$Z_6 = 2\zeta\frac{\partial B}{\partial T_0} - 2\frac{\partial A}{\partial T_0}\omega_{cr} - k_4\tau\frac{\partial A}{\partial T_0} \sin(\omega_{cr}\tau) - k_4\tau\frac{\partial B}{\partial T_0} \cos(\omega_{cr}\tau), \quad (4.78b)$$

$$Z_7 = \frac{3}{2}a_1A^2 - \frac{3}{2}a_1B^2, \quad (4.78c)$$

$$Z_8 = 3a_1AB, \quad (4.78d)$$

$$Z_9 = \frac{3}{2}a_1A^2 + \frac{3}{2}a_1B^2. \quad (4.78e)$$

In order to eliminate the secular terms, we set  $Z_5 = 0$  and  $Z_6 = 0$ . Equations (4.78a) and (4.78b) then give us:

$$\frac{\partial A}{\partial T_0} = 0, \quad (4.79a)$$

$$\frac{\partial B}{\partial T_0} = 0. \quad (4.79b)$$

Equation (4.77) is now rewritten as:

$$\frac{\partial^2 r_1}{\partial t^2} + 2\zeta\frac{\partial r_1}{\partial t} + a_3r_1 + k_4r_1(t-\tau) + Z_7 \cos(2\omega_{cr}t) + Z_8 \sin(2\omega_{cr}t) + Z_9 = 0. \quad (4.80)$$

The solution  $r_1(t, T_0, T_1)$  of Eq. (4.80) is assumed as follows:

$$r_1(t, T_0, T_1) = C_1(T_0, T_1) + C_2(T_0, T_1) \cos(2\omega_{cr}t) + C_3(T_0, T_1) \sin(2\omega_{cr}t). \quad (4.81)$$

Substituting Eq. (4.81) in Eq. (4.80) and solving for  $C_1$ ,  $C_2$  and  $C_3$ , we get:

$$C_1 = -\frac{3a_1(A^2 + B^2)}{2k_4 + a_3}, \quad (4.82a)$$

$$C_2 = \frac{h_1 \cos(2\omega_{cr}\tau) + h_2 \sin(2\omega_{cr}\tau) + h_3}{h_4}, \quad (4.82b)$$

$$C_3 = \frac{h_5 \cos(2\omega_{cr}\tau) + h_6 \sin(2\omega_{cr}\tau) + h_7}{h_8}, \quad (4.82c)$$

where  $h_1$  to  $h_8$  are defined as follows:

$$h_1 = -3a_1k_4B^2 + 3a_1k_4A^2, \quad (4.83a)$$

$$h_2 = 6a_1ABk_4, \quad (4.83b)$$

$$h_3 = -24a_1AB\omega_{cr}\zeta - 12a_1\omega_{cr}^2A^2 + 12a_1\omega_{cr}^2B^2 - 3a_1a_3B^2 + 3a_1a_3A^2, \quad (4.83c)$$

$$h_4 = (-4k_4a_3 + 16\omega_{cr}^2k_4) \cos(2\omega_{cr}\tau) - 2k_4^2 + 16k_4\zeta\omega_{cr} \sin(2\omega_{cr}\tau) - 32\zeta^2\omega_{cr}^2 - 2a_3^2 - 32\omega_{cr}^4 + 16\omega_{cr}^2a_3, \quad (4.83d)$$

$$h_5 = 3a_1B^2k_4 - 3a_1A^2k_4, \quad (4.83e)$$

$$h_6 = 6a_1ABk_4, \quad (4.83f)$$

$$h_7 = -24a_1AB\omega_{cr}^2 + 12a_1A^2\zeta\omega_{cr} - 12a_1B^2\zeta\omega_{cr} + 6a_1a_3AB, \quad (4.83g)$$

$$h_8 = (-4k_4a_3 + 16\omega_{cr}^2k_4) \cos(2\omega_{cr}\tau) - 2k_4^2 + 16k_4\zeta\omega_{cr} \sin(2\omega_{cr}\tau) - 32\zeta^2\omega_{cr}^2 - 2a_3^2 - 32\omega_{cr}^4 + 16\omega_{cr}^2a_3. \quad (4.83h)$$

Substituting Eq. (4.73) and (4.81) in Eq. (4.74c) and by setting the coefficients of secular terms to zero, we solve for  $\frac{\partial A}{\partial T_1}$  and  $\frac{\partial B}{\partial T_1}$ . Then, using the relations  $\dot{A} = \epsilon \frac{\partial A}{\partial T_0} + \epsilon^2 \frac{\partial A}{\partial T_1}$  and  $\dot{B} = \epsilon \frac{\partial B}{\partial T_0} + \epsilon^2 \frac{\partial B}{\partial T_1}$ , and substituting  $\frac{\partial A}{\partial T_0} = \frac{\partial B}{\partial T_0} = 0$  (see Eqs. (4.79a) and (4.79b)) in  $\dot{A}$  and  $\dot{B}$ , we note that:

$$\dot{A} = \epsilon^2 \frac{\partial A}{\partial T_1}, \quad (4.84a)$$

$$\dot{B} = \epsilon^2 \frac{\partial B}{\partial T_1}. \quad (4.84b)$$

Now, substituting the polar transformation  $A(t) = R(t) \sin(\theta(t))$  and  $B(t) = R(t) \cos(\theta(t))$  in Eqs. (4.84a) and (4.84b) and simplifying, the amplitude and phase modulation

equations can be written as follows:

$$\dot{R}(t) = R_1 \epsilon^2 \Delta R(t) + R_2 R^3(t), \quad (4.85a)$$

$$\dot{\theta}(t) = \theta_1 \epsilon^2 \Delta + \theta_2 R^2(t). \quad (4.85b)$$

The approximate solution of the DDE presented in Eq. (4.72), accurate to  $\mathcal{O}(\epsilon^0)$ , can now be written using the normal form equations (Eqs. (4.85a) and (4.85b)) as follows:

$$r(t) \approx R(t) \cos(\omega_{cr} t + \theta(t)), \quad (4.86a)$$

$$\dot{r}(t) \approx \dot{R}(t) \cos(\omega_{cr} t + \theta(t)) - R(t) \sin(\omega_{cr} t + \theta(t))(\omega_{cr} + \dot{\theta}(t)). \quad (4.86b)$$

#### 4.4.2.1 Hopf bifurcation at point $P_5$

Substituting the values of  $p_{cr}$  and  $\omega_{cr}$  for point  $P_5$  (see Table 4.1) in Eqs. (4.85a) and (4.85b), we get:

$$\dot{R}(t) = -289.1699178 \times 10^{-4} (\epsilon^2 \Delta) R(t) + 498.7098850 \times 10^{-3} R(t)^3, \quad (4.87a)$$

$$\dot{\theta}(t) = 15.76079909 \times 10^{-2} (\epsilon^2 \Delta) - 3.121840462 R(t)^2. \quad (4.87b)$$

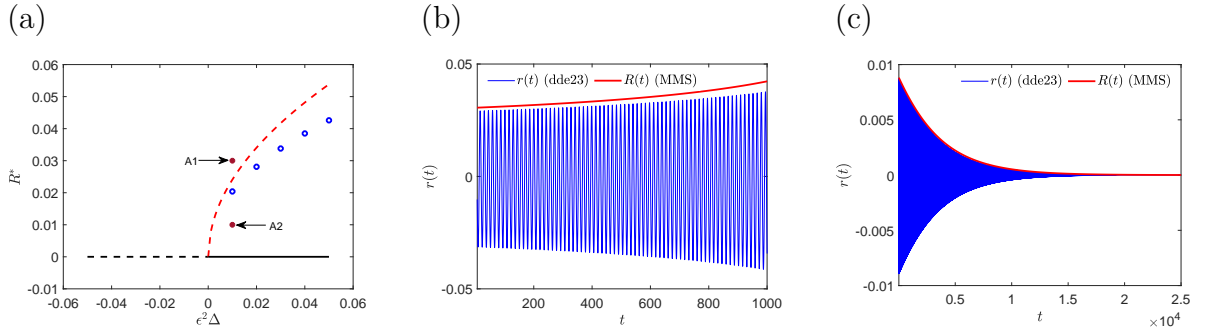


FIGURE 4.12: (a) Local bifurcation diagram at point  $P_5$ . System response at local bifurcation point  $P_5$  for  $\epsilon^2 \Delta = 0.01$  with initial conditions for Eqs. (4.87a) and (4.87b) given in Fig. 4.12(a) by point (b) A1 and (c) A2.

Figure 4.12(a) shows the local bifurcation diagram (subcritical Hopf bifurcation) obtained from Eq. (4.87a). To obtain the amplitude of unstable periodic solutions, we numerically integrate Eq. (4.72) for a given  $\epsilon^2 \Delta$  and for increasing values of the constant history function, and track the equilibrium solution. The critical value of the magnitude of the history function above which the equilibrium will not approach zero



is considered the magnitude of the unstable limit cycle (blue circle). Figure 4.12(b) shows  $R(t)$  obtained using Eq. (4.87a) (red line) and the system response (blue line) obtained by integrating Eq. (4.72) using the *dde23* MATLAB solver. Both cases are for  $\epsilon^2\Delta = 0.01$  and the magnitude of the history function given by point A1 in Fig. 4.12(a). Figure 4.12(c) shows the same physical quantities for the magnitude of the history function given by point A2 in Fig. 4.12(a).

Figures 4.12(a) and 4.12(b) indicate that for a given value of  $\epsilon^2\Delta (> 0)$ , any initial condition greater than  $R^*$  results in a diverging solution. On the contrary, for a given value of  $\epsilon^2\Delta (> 0)$ , any initial condition less than  $R^*$  (see Figs. 4.12(a) and 4.12(c)) results in the system settling at the buckled equilibrium (solid black line in Fig. 4.12(a)).

#### 4.4.2.2 Hopf bifurcation at point $P_6$

Substituting the values of  $p_{cr}$  and  $\omega_{cr}$  for point  $P_6$  (see Table 4.1) in Eqs. (4.85a) and (4.85b), we get:

$$\dot{R}(t) = 13.18331333 \times 10^{-4}(\epsilon^2\Delta)R(t) - 30.54194023 \times 10^{-3}R(t)^3, \quad (4.88a)$$

$$\dot{\theta}(t) = 6.161982410 \times 10^{-2}(\epsilon^2\Delta) - 1.331671312R(t)^2. \quad (4.88b)$$

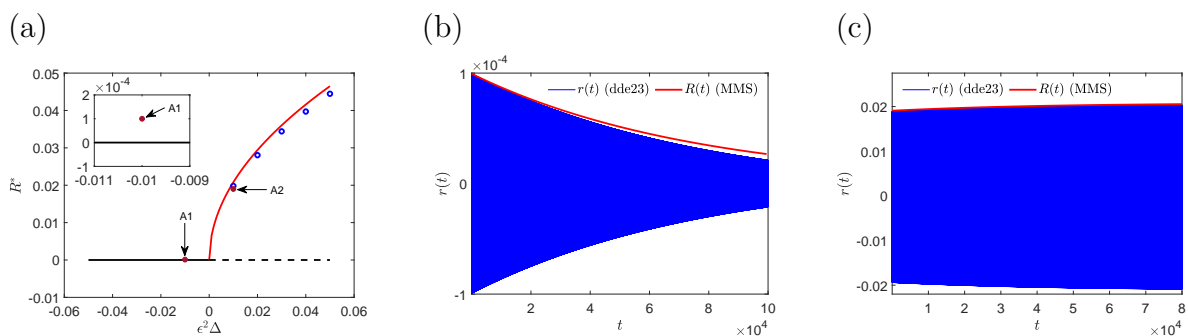


FIGURE 4.13: (a) Local bifurcation diagram at point  $P_6$ . System response at local bifurcation point  $P_6$  for (b)  $\epsilon^2\Delta = -0.01$  with initial conditions for Eqs. (4.88a) and (4.88b) given by point A1 in Fig. 4.13(a) and for (c)  $\epsilon^2\Delta = 0.01$  with initial conditions for Eqs. (4.88a) and (4.88b) given by point A2 in Fig. 4.13(a).

Figure 4.13(a) shows the local bifurcation diagram (supercritical Hopf bifurcation) obtained from Eq. (4.88a). Figures 4.13(b) (for  $\epsilon^2\Delta = -0.01$ ) and 4.13(c) (for  $\epsilon^2\Delta = 0.01$ ) show  $R(t)$  obtained using Eq. (4.88a) (red line) and the system response

obtained by integrating Eq. (4.72) using the *dde23* MATLAB solver (blue line). Figures 4.13(a) and 4.13(b) indicate that for  $\epsilon^2\Delta < 0$ , the system settles at the buckled equilibrium (solid black line in Fig. 4.13(a)) for any initial condition. For  $\epsilon^2\Delta > 0$  (see Figs. 4.13(a) and 4.13(c)), the system settles into a periodic motion whose amplitude is given by  $R^*$  corresponding to the value of  $\epsilon^2\Delta$ .

#### 4.4.2.3 Hopf bifurcation at point $P_7$

Substituting the values of  $p_{cr}$  and  $\omega_{cr}$  for point  $P_7$  (see Table 4.1) in Eqs. (4.85a) and (4.85b), we get:

$$\dot{R}(t) = -11.35943198 \times 10^{-4}(\epsilon^2\Delta)R(t) + 20.63464775 \times 10^{-3}R(t)^3, \quad (4.89a)$$

$$\dot{\theta}(t) = 5.641822544 \times 10^{-2}(\epsilon^2\Delta) - 1.215852977R(t)^2. \quad (4.89b)$$

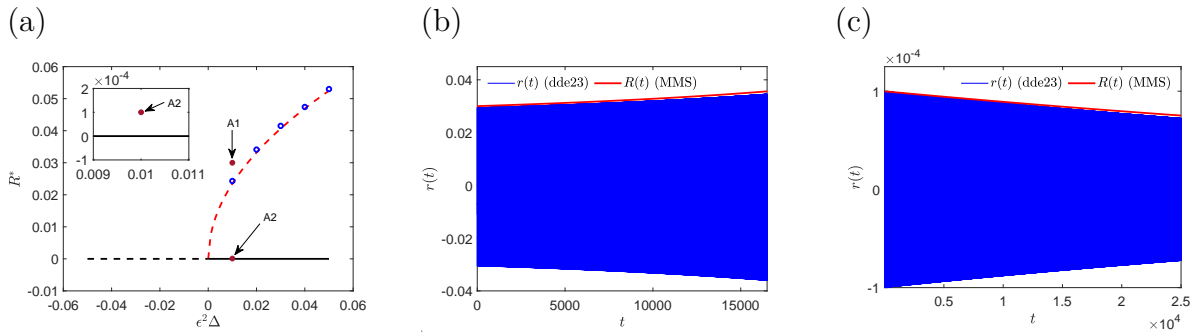


FIGURE 4.14: (a) Local bifurcation diagram at point  $P_7$ . System response at local bifurcation point  $P_7$  for  $\epsilon^2\Delta = 0.01$  with initial conditions for Eqs. (4.89a) and (4.89b) given in Fig. 4.14(a) by point (b) A1 and (c) A2.

Figure 4.14(a) shows the local bifurcation diagram (subcritical Hopf bifurcation) obtained from Eq. (4.89a). Figures 4.14(a), 4.14(b) and 4.14(c) are similar to Figs. 4.12(a), 4.12(b) and 4.12(c), except that these results are for the bifurcation point  $P_7$ . Figures 4.14(a) and 4.14(b) indicate that for a given value of  $\epsilon^2\Delta (> 0)$ , any initial condition greater than  $R^*$  results in a diverging solution. On the contrary, for a given value of  $\epsilon^2\Delta (> 0)$ , any initial condition less than  $R^*$  (see Figs. 4.14(a) and 4.14(c)) results in the system settling at the buckled equilibrium (solid black line in Fig. 4.14(a)).

It can be seen from Figs. 4.12, 4.13 and 4.14 that the transient and the steady-state solutions of the normal-form equations for buckled equilibrium, obtained using

the MMS, both match closely with the results obtained from direct numerical integration. This implies that both the methods are appropriate choices for this study. The mutual consistency of the results also serves to authenticate the results themselves. It should also be noted that for this study, the results obtained using the MMS were computationally less expensive than the results obtained from direct numerical integration. This makes MMS a candidate approach for studying the Hopf bifurcations of such systems.

All the results obtained using the MMS reported in this section are valid for small values of  $\epsilon$ . To study the behaviour of the system far from the bifurcation points, we resort to numerics and generate a global bifurcation diagram. These results are described in the next section.

### 4.5 Global bifurcation analysis

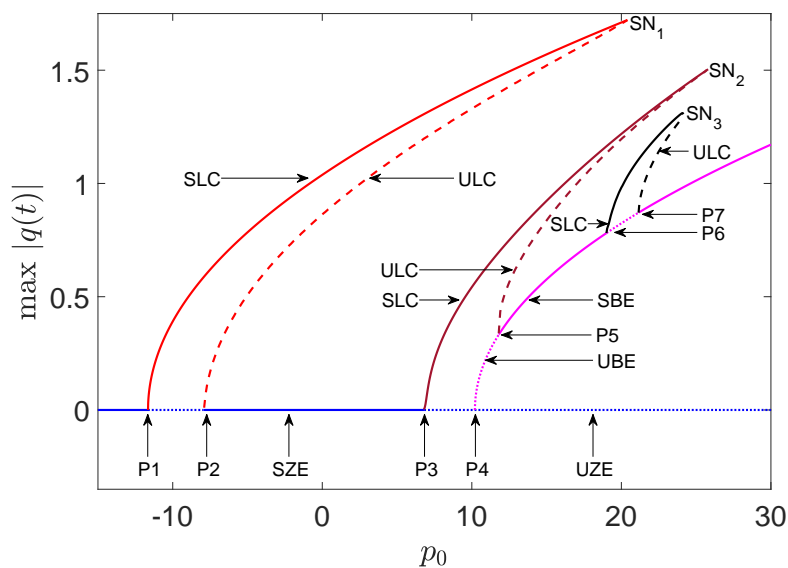


FIGURE 4.15: Global bifurcation diagram of Eq. (4.8) for  $U = 1$  and  $p_0 \in [-15, 30]$ . Stable limit-cycles arising from points  $P_1$ ,  $P_3$  and  $P_6$  are denoted by SLC and the unstable limit-cycles arising from points  $P_2$ ,  $P_5$  and  $P_7$  are denoted by ULC. Stable zero equilibrium is represented by blue solid line (SZE) and the unstable zero equilibrium is represented by dotted blue line (UZE). Magenta solid line represents the stable buckled equilibrium (SBE) and magenta dotted line represents the unstable buckled equilibrium (UBE).

Figure 4.15 shows the global bifurcation diagram obtained by integrating Eq. (4.8) using the *dde23* MATLAB solver, for  $U = 1$  and varying the axial load  $p_0$ , with

$p_0 \in [-15, 30]$ . It can clearly be seen from Fig. 4.15 that  $P_1, P_2, P_3, P_5, P_6,$  and  $P_7$  are the Hopf bifurcation points. Furthermore, it should be observed that from point  $P_4$ , a second equilibrium ( $\bar{q} = \bar{q}_2$ ) coexists with the equilibrium given by  $\bar{q} = \bar{q}_1$ . Solid blue lines indicate the stable equilibrium points and dotted blue line indicate the unstable equilibrium points for  $\bar{q} = \bar{q}_1 = 0$ . Solid magenta lines are the stable equilibrium points and dotted magenta lines are the unstable equilibrium points for  $\bar{q} = \bar{q}_2 = \pm \sqrt{\frac{-\alpha_3[1-\frac{p_0}{\pi^2}] - \alpha_5 U^2}{\alpha_4}}$ . In Fig. 4.15, solid and dashed-lines represent the stable and unstable solutions, respectively. The stable and unstable periodic solutions are tracked using the same method as described in Section 4.4.

It can be seen from Fig. 4.15 that the stable and unstable periodic solutions arising from  $P_1$  and  $P_2$  meet at the **cyclic-fold** bifurcation point  $SN_1$ . At  $SN_1, p_0 = 20.41$ , after which both stable and unstable periodic solutions arising from  $P_1$  and  $P_2$  cease to exist.  $SN_2$  is the **cyclic-fold** bifurcation point for the stable and unstable periodic solutions arising from  $P_3$  and  $P_5$ , respectively.  $SN_3$  is the **cyclic-fold** bifurcation point for the stable and unstable periodic solutions arising from  $P_6$  and  $P_7$ , respectively. The axial loads at  $SN_2$  and  $SN_3$  are 25.8 and 24.15, respectively. The following important observations can be made from Fig. 4.15.

1. For  $p_0 \in (P_1, SN_2]$  there exist multiple limit-cycles (both stable and unstable) for the system, due to Hopf bifurcation at different points.
2. The zero equilibrium is unstable in the intervals  $[P_1, P_2]$ , and  $P_3$  and beyond. The buckled equilibrium is unstable over intervals  $[P_4, P_5]$  and  $[P_6, P_7]$ . Since no stable static equilibrium exists in these regions, the system can only settle in a stable limit-cycle.

Figures 4.16(a), 4.16(b), and 4.16(c) show the limit-cycles for  $p_0 = 1, p_0 = 13$  and  $p_0 = 20$ , respectively. For  $p_0 = 1$  (Fig. 4.16(a)), two coexisting limit-cycles are present: one originating from supercritical Hopf bifurcation at  $P_1$  (stable limit-cycle, red solid-line) and the other from the subcritical Hopf bifurcation at  $P_2$  (unstable limit-cycle, red dashed-line). For  $p_0 = 13$  (Fig. 4.16(b)), four limit-cycles coexist. Of these, two stable limit-cycles arise from the supercritical Hopf bifurcation originating at points  $P_1$  (red solid-line) and  $P_3$  (brown solid-line), and two unstable limit-cycles arise from the subcritical Hopf bifurcation originating at points  $P_2$  (red dashed-line) and  $P_5$  (brown dashed-line). For  $p_0 = 20$  (Fig. 4.16(c)), five limit-cycles coexist. Of these, three stable limit-cycles arise from the supercritical Hopf bifurcation originating at points  $P_1$  (red solid-line),  $P_3$  (brown solid-line) and  $P_6$  (black solid-line), and two unstable limit-cycles arise from the subcritical Hopf bifurcation originating at points

$P_2$  (red dashed-line) and  $P_5$  (brown dashed-line). Figure 4.16 should be contrasted with Fig. 4.15. All stable limit-cycles for  $p_0 = 1$ ,  $p_0 = 13$  and  $p_0 = 20$  are obtained by directly integrating the DDE given by Eq. (4.8). Obtaining unstable limit-cycles for a system is a challenging task and hence the bisection method is used [58].

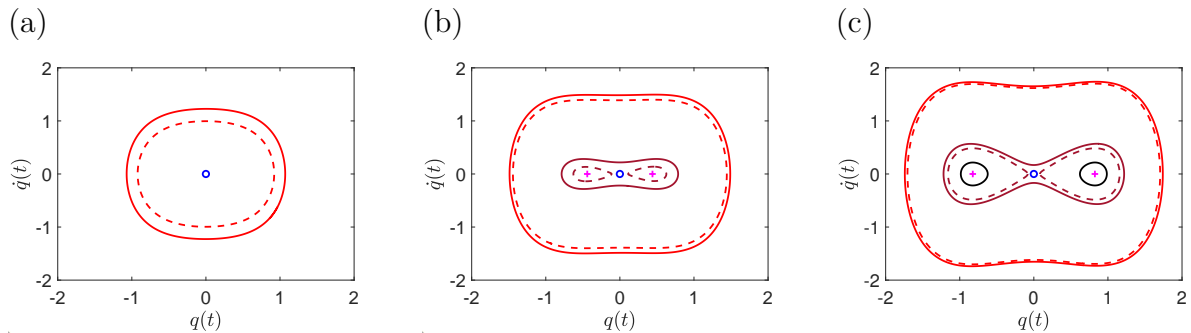


FIGURE 4.16: (a) Limit-cycles for  $U = 1$  with (a)  $p_0 = 1$ , (b)  $p_0 = 13$  and (c)  $p_0 = 20$ .

It can be seen that for  $U = 1$ , at lower axial loads (see Fig. 4.16(a)), the amplitude of stable limit-cycle oscillations is relatively less than that for higher axial loads (see Figs. 4.16(b) and 4.16(c)) making  $p_0 \leq P_1$  a more favorable region to operate as the beam settles to zero equilibrium. The existence of multiple limit-cycles at higher axial loads pose operational challenges because there are more than one settling amplitudes, that depend on the initial conditions. Multiple limit-cycles at higher values of axial load make fatigue life calculations more complicated in that region of the parametric space. However, if the operational conditions push the system into multiple limit-cycles region, fatigue-life calculations should be based on the worst case scenario of the limit-cycle amplitudes. It should be noted from the global bifurcation diagram that by inducing tensile loads, we can change  $p_0$  from positive to negative and can control the region of operation of the heat exchanger. For example, if we apply sufficient tension and make  $p_0 = -5$ , the tube will be stable around zero equilibrium for flow velocity of  $U = 1$ .

Another important observation that can be made from Figs. 4.16(b) and 4.16(c) is regarding the small margin between the larger stable and unstable limit cycles. For the system lying exactly on the larger unstable limit cycle, a small external perturbation will take the system to either the outer larger stable limit cycle or the inner smaller stable limit cycle. The inner and outer stable limit cycles have remarkably different amplitudes; this makes the behavior of the system in the vicinity of the larger unstable limit cycle highly unpredictable. This further reinforces the argument that predictive fatigue-life calculations must be based on the worst-case scenario.

## 4.6 Chapter Summary

The nonlinear dynamics of a heat-exchanger tube subjected to cross-flow has been studied. The critical curves for the resulting DDE is first obtained using an analytical approach. A Galerkin method is then used to analyze the stability of the system in the parametric space of flow velocity and axial (thermal) load. The analytical technique only gives the possible critical curves at which a stability switch may happen. However, using Galerkin approximations, the rightmost characteristic roots of the DDE in the  $[U, p_0]$  plane are obtained to generate a more comprehensive stability chart. Furthermore, the damping present in the rightmost root, in the stable region, is obtained. The highest damping is present around  $U = 2.34$  and  $p_0 = 30$ . The possibility of Hopf bifurcation has been investigated for  $U = 1$ . It is found that both zero and buckled equilibria can lose stability through supercritical or subcritical Hopf bifurcation. Using the method of multiple scales (MMS), normal forms near the bifurcation points have been obtained analytically. The results from local-bifurcation analysis using the MMS are in close agreement with numerical results indicating that both methods are appropriate for this study. The consistency of the results also serve to authenticate them. However, since the MMS is valid only in the immediate vicinity of the Hopf-bifurcation points, a global-bifurcation diagram has been generated using numerical simulations to analyze the tube motion farther away from the bifurcation points.

The presence of multiple co-existing limit-cycles at higher axial loads ( $p_0 = 13$ , and  $p_0 = 20$ ) present operational challenges. This is due to the uncertainty in the settling amplitude that is contingent on the initial conditions of the vibrating tube, which in turn are hard to capture. Furthermore, the global-bifurcation diagram indicates that apart from Hopf bifurcations, three cyclic-fold bifurcation points also exist where the stable and unstable periodic solutions meet and cease to exist thereafter. The presence of cyclic-fold bifurcations implies that at certain values of axial load, the system can switch from one limit-cycle to another, which makes the behavior of the beam unpredictable.

The stability studies carried out in this chapter are expected to be useful in the designing of heat-exchanger tubes for greater tube life and safety. Therefore, for a given flow velocity, axial load can be tuned from the stability chart for maximum damping. Further, from the global bifurcation diagram, for a given flow velocity, axial load can be adjusted to suppress the limit cycle oscillations.

In the past, Sadath et al. [40] obtained the stability regions for a simply-supported tube under axial loads and cross-flow. Contrary to the present study, a flutter instability region was also found to exist. More importantly, the present study indicates the presence of more and smaller unstable regions within previously discovered stable regions [40]. Furthermore, the present work also reports the damping in the parametric space of the axial load and flow velocity, which has not been done in ref. [40]. The results obtained in the present study can also be contrasted with those by Xia and Wang [31]. In the latter study, it was found that the impact-related force contributes principally to the nonlinearity in the system. The effect of the nonlinearity induced by axial tension was not pronounced.

# Chapter 5

## Conclusions and Future Work

Cross-flow-induced vibrations of a single flexible heat-exchanger tube in an array of rigid cylinders has been studied. This study is expected to be useful at the design stage of heat-exchanger tubes, with the intention of safe and efficient operation in the power-plant industry. Based on the results presented in Chapters 2 to 4, the following important conclusions are made:

- A stability analysis involving the second-order DDE of motion from [4] is conducted for a single flexible cylinder in the parametric space of mass-damping parameter and reduced velocity.
- Contrary to several earlier studies that have reported only the stability threshold, the information on the damping in the stable region has been reported here for the first time. The region of the highest damping and therefore, maximum stability is found to exist around  $m\delta = 1.333$  and  $U = 0.791$ , where the vibration response of the tube will decay most rapidly.
- Contrary to popular opinion, this work indicates that the region of maximum damping is a localized region in the parametric space, close to the stability boundary.
- The region of maximum damping is achieved at a comparatively lower mass-damping parameter value for  $\mu = 0.5$ , and a comparatively higher mass-damping parameter value for  $\mu = 2$ , and hence shifts with a shift in the value of the time delay, calling into the question the choice of  $\mu = 1$ .
- In the study that models a heat-exchanger tube as a cantilever beam, the stability and spectrum in the parametric space of cladding stiffness and flow velocity



has been obtained for the first time. The knowledge of damping in the parametric space is useful for the control of large-amplitude vibrations. For a given value of operational flow velocity, the value of  $k_1$  can be traced back from a region where the damping is high. In this manner, the system can be designed with a  $k_1$ , so as to operate it in a region where the damping is high, thereby guaranteeing maximum stability for a given operational flow velocity.

- Multiple limit cycles (both stable and unstable) are found to coexist for  $k_1 \in (0, 100]$ . In the case of a stable zero equilibrium and a single stable limit cycle ( $k_1 \in (33, 70]$ ), fatigue life calculations are easier. When there are multiple periodic solutions, fatigue life calculations must be based on the worst-case scenario, i.e., the largest limit-cycle amplitude.
- $k_1 \in (33, 70]$  provides a range for optimal design values of the linear spring stiffness. High values of  $k_1$  can induce high stresses on the tube in response to tube thermal expansion. Moreover, our analysis indicates that high values of  $k_1$ , i.e., stiffer claddings, do not necessarily guarantee a more stable system. On the other hand, low values of  $k_1$  may not be effective against impact with baffles, while also subjecting the system to the risk of multiple periodic solutions.
- The range  $k_1 \in (33, 70]$  is most desirable for design purposes since the zero equilibrium is stable and there is only one stable limit cycle in this range.
- For a simply-supported heat-exchanger tube, the damping present in the right-most root, in the stable region, is obtained in the parametric space of flow velocity and axial (thermal) load. The highest damping is present around  $U = 2.34$  and  $p_0 = 30$ . Using the damping information for a given flow velocity, the axial load can be tuned from the stability chart for maximum damping.
- The possibility of Hopf bifurcation has been investigated for  $U = 1$ . It is found that both zero and buckled equilibria can lose stability through supercritical or subcritical Hopf bifurcation.
- The presence of multiple co-existing limit-cycles at higher axial loads ( $p_0 = 13$ , and  $p_0 = 20$ ) present operational challenges. This is due to the uncertainty in the settling amplitude that is contingent on the initial conditions of the vibrating tube, which in turn are hard to capture. However, for a given flow velocity, the axial load can be adjusted to suppress the limit cycle oscillations.
- Apart from Hopf bifurcations, three cyclic-fold bifurcation points also exist where the stable and unstable periodic solutions meet and cease to exist thereafter. The presence of cyclic-fold bifurcations implies that at certain values of

axial load, the system can switch from one limit-cycle to another, which makes the behavior of the beam unpredictable.

## 5.1 Open problems and future work

A few open problems that are yet to be addressed are the following:

- The damping in the parametric space of mass-damping parameter and flow velocity needs to be computed in the case of the more realistic two-phase flow.
- The effect of mode-coupling can be investigated with the inclusion of multiple modes in the Galerkin approximations employed while modeling the heat-exchanger tube as a cantilever or a simply-supported beam.
- The baffle-cladding tends to deform over time, resulting in there being a gap between the tube and the cladding. In such a case, the impact of the beam with the cladding must be taken into consideration.
- Studies for the control of the vibration response of the tube are required. As is evident from this thesis, parameters such as the cladding stiffness and the axial loads can be adjusted, either at the design stage or during the course of operation for system stability. The control problem for time-delayed systems is challenging and stabilization techniques need to be developed to address the issue. Shanti et al. [?] devised a pole-placement technique for time-delayed systems, which combined the advantages of the method of receptances and an optimization-based strategy. The objective was to design a controller that places the closed-loop poles at specific locations, to achieve stability. More techniques for stabilizing time-delayed systems are currently being investigated by our group.

## References

- [1] S. F. Corzo, D. M. Godino, N. M. Nigro, and D. E. Ramajo, “Thermal hydraulics simulation of the rd-14m steam generator facility,” *Annals of Nuclear Energy*, vol. 105, pp. 282–301, 2017.
- [2] M. P. Paidoussis, S. J. Price, and E. de Langre, *Fluid-Structure Interactions : Cross-Flow-Induced Instabilities*. Cambridge University Press, 2011. New York, pp. 215-287.
- [3] A. Khalifa, *Fluidelastic Instability in Heat Exchanger Tube Arrays*. PhD thesis, McMaster University, 2012.
- [4] S. J. Price and M. P. Paidoussis, “An improved mathematical model for the stability of cylinder rows subject to cross-flow,” *Journal of Sound and Vibration*, vol. 97, no. 4, pp. 615–640, 1984.
- [5] R. T. Hartlen, *Wind-tunnel Determination of Fluid-elastic-vibration Thresholds for Typical Heat-exchanger Tube Patterns*. Ontario Hydro Research Division, 1974.
- [6] W. J. Heilker and R. Q. Vincent, “Vibration in nuclear heat exchangers due to liquid and two-phase flow,” *ASME Journal of Engineering for Power*, vol. 103, pp. 358–365, 1981.
- [7] M. J. Pettigrew, Y. Sylvestre, and A. O. Campagna, “Vibration analysis of heat exchanger and steam generator designs,” *Nuclear Engineering and Design*, vol. 48, no. 1, pp. 97–115, 1978.
- [8] D. S. Weaver and L. K. Grover, “Cross-flow induced vibrations in a tube bank—turbulent buffeting and fluid elastic instability,” *Journal of Sound and Vibration*, vol. 59, no. 2, pp. 277–294, 1978.

- [9] D. S. Weaver and M. El-Kashlan, "The effect of damping and mass ratio on the stability of a tube bank," *Journal of Sound and Vibration*, vol. 76, no. 2, pp. 283–294, 1981.
- [10] A. Sharma and S. K. Sharma, "Report of the Comptroller and Auditor General of India on Kudankulam Nuclear Power Project, Units I and II." Union Government Department of Atomic Energy, Report No. 38 of 2017.
- [11] "Draft National Electricity Plan: Generation," 2016. Central Electricity Authority, Govt. of India Ministry of Power Central Electricity Authority, Vol. 1, 2016.
- [12] P. Moore, "Going Nuclear: A Green Makes the Case," 2006. Washington Post, 2016, pp. B01.
- [13] "Nuclear Fuel." [www.nei.org/fundamentals/nuclear-fuel](http://www.nei.org/fundamentals/nuclear-fuel), 2019. Nuclear Energy Institute, Last accessed April 10, 2019.
- [14] D. Martin, "Exporting Disaster: The Cost of Selling CANDU Reactors." [www.dianuke.org/exporting-disaster-cost-selling-candu-reactors/](http://www.dianuke.org/exporting-disaster-cost-selling-candu-reactors/). Last modified April 26, 2016, last accessed April 8, 2019.
- [15] "A Reporter's Guide to Bruce Power." <http://www.brucepower.com/docs/reports/corporate/A%20Reporters%20Guide%20to%20Bruce%20Power.pdf>, 2007. Bruce Power L. P., Last accessed April 1, 2019.
- [16] "List of Generating Stations in Quebec." [https://en.wikipedia.org/wiki/List\\_of\\_generating\\_stations\\_in\\_Quebec#Nuclear](https://en.wikipedia.org/wiki/List_of_generating_stations_in_Quebec#Nuclear), 2018. Wikipedia, Last modified 10 November 2018, last accessed April 8, 2019.
- [17] M. P. Paidoussis, "Real-life experiences with flow-induced vibration," *Journal of fluids and structures*, vol. 22, no. 6-7, pp. 741–755, 2006.
- [18] S. Khushnood, Z. M. Khan, M. A. Malik, Z. Koreshi, M. A. Javaid, M. A. Khan, A. H. Qureshi, L. A. Nizam, K. S. Bashir, and S. Z. Hussain, "Cross-flow-induced-vibrations in heat exchanger tube bundles: A review," *Nuclear Power Plants*, p. 71, 2012.
- [19] S. Mittal and S. Singh, "Vortex-induced vibrations at subcritical  $Re$ ," *Journal of Fluid Mechanics*, vol. 534, pp. 185–194, 2005.
- [20] S. S. Chen, "Instability mechanisms and stability criteria of a group of circular cylinders subjected to cross-flow. Part I: Theory," *Journal of Vibration, Acoustics, Stress, and Reliability in Design*, vol. 105, no. 1, pp. 51–58, 1983.

## REFERENCES

---

- [21] S. S. Chen, “Instability mechanisms and stability criteria of a group of circular cylinders subjected to cross-flow. Part II: Numerical results and discussions,” *Journal of Vibration, Acoustics, Stress, and Reliability in Design*, vol. 105, no. 2, pp. 253–260, 1983.
- [22] C. Meskell, “A new model for damping controlled fluidelastic instability in heat exchanger tube arrays,” *Proceedings of The Institution of Mechanical Engineers Part A- Journal of Power and Energy*, vol. 223, pp. 361–368, 2009.
- [23] M. P. Paidoussis, “A review of flow-induced vibrations in reactors and reactor components,” *Nuclear Engineering and Design*, vol. 74, no. 1, pp. 31–60, 1983.
- [24] H. J. Connors Jr, “Fluid elastic vibration of tube arrays excited by cross flow,” in *ASME Symposium on Flow-Induced Vibration in Heat Exchanger, Winter annual meeting*, pp. 42–47, 1970.
- [25] Y. Bazilevs, K. Takizawa, and T. E. Tezduyar, *Computational Fluid-structure Interaction: Methods and Applications*. John Wiley & Sons, 2013. West Sussex, UK, pp. 9-19.
- [26] V. Shinde, *Fluidelastic instability in heat exchanger tube arrays and a Galerkin-free model reduction of multiphysics systems*. PhD thesis, 2015.
- [27] J. H. Lever and D. S. Weaver, “A theoretical model for fluid-elastic instability in heat exchanger tube bundles,” *Journal of Pressure Vessel Technology*, vol. 104, no. 3, pp. 147–158, 1982.
- [28] A. Khalifa, D. Weaver, and S. Ziada, “A single flexible tube in a rigid array as a model for fluidelastic instability in tube bundles,” *Journal of Fluids and Structures*, vol. 34, pp. 14–32, 2012.
- [29] L. Wang and Q. Ni, “Hopf bifurcation and chaotic motions of a tubular cantilever subject to cross flow and loose support,” *Nonlinear Dynamics*, vol. 59, no. 1-2, pp. 329–338, 2010.
- [30] L. Wang, H. L. Dai, and Y. Y. Han, “Cross-flow-induced instability and nonlinear dynamics of cylinder arrays with consideration of initial axial load,” *Nonlinear Dynamics*, vol. 67, no. 2, pp. 1043–1051, 2012.
- [31] W. Xia and L. Wang, “The effect of axial extension on the fluidelastic vibration of an array of cylinders in cross-flow,” *Nuclear Engineering and Design*, vol. 240, no. 7, pp. 1707–1713, 2010.

- [32] B. de Pedro Palomar and C. Meskell, “Sensitivity of the damping controlled fluidelastic instability threshold to mass ratio, pitch ratio and reynolds number in normal triangular arrays,” *Nuclear Engineering and Design*, vol. 331, pp. 32–40, 2018.
- [33] A. Khalifa, D. Weaver, and S. Ziada, “Modeling of the phase lag causing fluidelastic instability in a parallel triangular tube array,” *Journal of Fluids and Structures*, vol. 43, pp. 371–384, 2013.
- [34] H. Li and N. Mureithi, “Development of a time delay formulation for fluidelastic instability model,” *Journal of Fluids and Structures*, vol. 70, pp. 346–359, 2017.
- [35] J. Mahon and C. Meskell, “Estimation of the time delay associated with damping controlled fluidelastic instability in a normal triangular tube array,” *Journal of Pressure Vessel Technology*, vol. 135, no. 3, p. 030903, 2013.
- [36] T. Sawadogo and N. Mureithi, “Fluidelastic instability study on a rotated triangular tube array subject to two-phase cross-flow. Part II: Experimental tests and comparison with theoretical results,” *Journal of Fluids and Structures*, vol. 49, pp. 16–28, 2014.
- [37] M. P. Paidoussis and G. X. Li, “Cross-flow-induced chaotic vibrations of heat-exchanger tubes impacting on loose supports,” *Journal of Sound and Vibration*, vol. 152, no. 2, pp. 305–326, 1992.
- [38] S. Granger and M. P. Paidoussis, “An improvement to the quasi-steady model with application to cross-flow-induced vibration of tube arrays,” *Journal of Fluid Mechanics*, vol. 320, pp. 163–184, 1996.
- [39] A. Sadath, H. N. Dixit, and C. P. Vyasarayani, “Dynamics of cross-flow heat exchanger tubes with multiple loose supports,” *Journal of Pressure Vessel Technology*, vol. 138, no. 5, p. 051303, 2016.
- [40] A. Sadath, V. Vinu, and C. P. Vyasarayani, “Vibrations of a simply supported cross flow heat exchanger tube with axial load and loose supports,” *Journal of Computational and Nonlinear Dynamics*, vol. 12, no. 5, p. 051001, 2017.
- [41] Y. Cai and S. S. Chen, “Chaotic vibrations of nonlinearly supported tubes in crossflow,” *Journal of Pressure Vessel Technology*, vol. 115, no. 2, pp. 128–134, 1993.

## REFERENCES

---

- [42] B. de Pedro, J. Parrondo, C. Meskell, and J. F. Oro, “Cfd modelling of the cross-flow through normal triangular tube arrays with one tube undergoing forced vibrations or fluidelastic instability,” *Journal of Fluids and Structures*, vol. 64, pp. 67–86, 2016.
- [43] N.-b. Jiang, B. Chen, F.-g. Zang, and Y.-x. Zhang, “An unsteady model for fluidelastic instability in an array of flexible tubes in two-phase cross-flow,” *Nuclear Engineering and Design*, vol. 285, pp. 58–64, 2015.
- [44] J. Liu, C. Huang, and N. Jiang, “Unsteady model for transverse fluid elastic instability of heat exchange tube bundle,” *Mathematical Problems in Engineering*, vol. 2014, 2014.
- [45] C. Meskell, “A new model for damping controlled fluidelastic instability in heat exchanger tube arrays,” *Proceedings of the Institution of Mechanical Engineers, Part A: Journal of Power and Energy*, vol. 223, no. 4, pp. 361–368, 2009.
- [46] M. Hassan and A. Hossen, “Time domain models for damping-controlled fluidelastic instability forces in tubes with loose supports,” *Journal of Pressure Vessel Technology*, vol. 132, no. 4, p. 041302, 2010.
- [47] I.-C. Chu, H. J. Chung, and S. Lee, “Flow-induced vibration of nuclear steam generator U-tubes in two-phase flow,” *Nuclear Engineering and Design*, vol. 241, no. 5, pp. 1508–1515, 2011.
- [48] V. Shinde, E. Longatte, F. Baj, and M. Braza, “A theoretical model of fluidelastic instability in tube arrays,” *Nuclear Engineering and Design*, vol. 337, pp. 406–418, 2018.
- [49] C. P. Vyasrayani, S. Subhash, and T. Kalmár-Nagy, “Spectral approximations for characteristic roots of delay differential equations,” *International Journal of Dynamics and Control*, vol. 2, no. 2, pp. 126–132, 2014.
- [50] S. Sandström, “Vibration analysis of a heat exchanger tube row with adina,” *Computers & Structures*, vol. 26, no. 1-2, pp. 297–305, 1987.
- [51] R. Azizian and N. Mureithi, “A simple empirical model for tube–support normal impact interaction,” *Journal of Pressure Vessel Technology*, vol. 136, no. 5, p. 051303, 2014.

- [52] M. R. Saffarian, F. Fazelpour, and M. Sham, “Numerical study of shell and tube heat exchanger with different cross-section tubes and combined tubes,” *International Journal of Energy and Environmental Engineering*, vol. 10, no. 1, pp. 33–46, 2019.
- [53] “Standards of the tubular exchanger manufacturers association.” [http://www1.frm.utn.edu.ar/electromecanica/materias%20pagina%20nuevas/INSTALACIONES%20TERMICAS%20MECANICAS%20Y%20FRIGORIFICAS/material/apuntes/TEMA\\_9TH\\_EDITION\\_2007.pdf](http://www1.frm.utn.edu.ar/electromecanica/materias%20pagina%20nuevas/INSTALACIONES%20TERMICAS%20MECANICAS%20Y%20FRIGORIFICAS/material/apuntes/TEMA_9TH_EDITION_2007.pdf), 2018. Tubular Exchanger Manufacturers Association Inc., 2007, last accessed March 22, 2019.
- [54] “Metals and alloys- densities.” [www.engineeringtoolbox.com/metal-alloys-densities-d\\_50\\$.html](http://www.engineeringtoolbox.com/metal-alloys-densities-d_50$.html), 2004. Engineering Toolbox, 2004, last accessed March 28, 2019.
- [55] P. Wahi and A. Chatterjee, “Galerkin projections for delay differential equations,” *Journal of Dynamic Systems, Measurement, and Control*, vol. 127, no. 1, pp. 80–87, 2005.
- [56] J.-H. He, “Bookkeeping parameter in perturbation methods,” *International Journal of Nonlinear Sciences and Numerical Simulation*, vol. 2, no. 3, pp. 257–264, 2001.
- [57] S. Das and A. Chatterjee, “Multiple scales without center manifold reductions for delay differential equations near Hopf bifurcations,” *Nonlinear Dynamics*, vol. 30, no. 4, pp. 323–335, 2002.
- [58] A. H. Nayfeh and B. Balachandran, *Applied Nonlinear Dynamics: Analytical, Computational, and Experimental Methods*. John Wiley & Sons, 2008.
- [59] M. J. Pettigrew, M. Yetisir, N. J. Fisher, B. A. Smith, C. E. Taylor, and V. P. Janzen, “Fretting-wear damage due to vibration in nuclear and process equipment,” in *ASME 2017 Pressure Vessels and Piping Conference*, p. V004T04A032, American Society of Mechanical Engineers, 2017.
- [60] S. Yi, P. W. Nelson, and A. G. Ulsoy, *Time-Delay Systems: Analysis and Control Using the Lambert W Function*. Hackensack, NJ, USA: World Scientific, 2010.
- [61] F. M. Asl and A. G. Ulsoy, “Analysis of a system of linear delay differential equations,” *Journal of Dynamic Systems, Measurement, and Control*, vol. 125, no. 2, pp. 215–223, 2003.



## REFERENCES

---

- [62] E. Jarlebring and T. Damm, “The lambert w function and the spectrum of some multidimensional time-delay systems,” *Automatica*, vol. 43, no. 12, pp. 2124–2128, 2007.
- [63] S. Yi, P. W. Nelson, and A. G. Ulsoy, “Survey on analysis of time delayed systems via the lambert w function,” *differential equations*, vol. 25, p. 28, 2007.
- [64] P. Wahi and A. Chatterjee, “Asymptotics for the characteristic roots of delayed dynamic systems,” *Journal of Applied Mechanics*, vol. 72, no. 4, pp. 475–483, 2005.
- [65] C. P. Vyasarayani, “Galerkin approximations for higher order delay differential equations,” *Journal of Computational and Nonlinear Dynamics*, vol. 7, no. 3, p. 031004, 2012.
- [66] A. Sadath and C. P. Vyasarayani, “Galerkin approximations for stability of delay differential equations with distributed delays,” *Journal of Computational and Nonlinear Dynamics*, vol. 10, no. 6, p. 061024, 2015.
- [67] T. Insperger and G. Stépán, *Semi-discretization for Time-Delay Systems: Stability and Engineering Applications*, vol. 178. New York, NY, USA: Springer Science & Business Media, 2011.
- [68] E. A. Butcher, H. Ma, E. Bueler, V. Averina, and Z. Szabo, “Stability of linear time-periodic delay-differential equations via chebyshev polynomials,” *International Journal for Numerical Methods in Engineering*, vol. 59, no. 7, pp. 895–922, 2004.
- [69] D. Breda, S. Maset, and R. Vermiglio, “Pseudospectral differencing methods for characteristic roots of delay differential equations,” *SIAM Journal on Scientific Computing*, vol. 27, no. 2, pp. 482–495, 2005.
- [70] Z. Wu and W. Michiels, “Reliably computing all characteristic roots of delay differential equations in a given right half plane using a spectral method,” *Journal of Computational and Applied Mathematics*, vol. 236, no. 9, pp. 2499–2514, 2012.
- [71] J.-Q. Sun, “A method of continuous time approximation of delayed dynamical systems,” *Communications in Nonlinear Science and Numerical Simulation*, vol. 14, no. 4, pp. 998–1007, 2009.
- [72] B. Song and J.-Q. Sun, “Lowpass filter-based continuous-time approximation of delayed dynamical systems,” *Journal of Vibration and Control*, vol. 17, no. 8, pp. 1173–1183, 2011.

- [73] T. Vyhlidal and P. Zítek, “Mapping based algorithm for large-scale computation of quasi-polynomial zeros,” *IEEE Transactions on Automatic Control*, vol. 54, no. 1, pp. 171–177, 2009.
- [74] N. Olgac and R. Sipahi, “An exact method for the stability analysis of time-delayed linear time-invariant (LTI) systems,” *IEEE Transactions on Automatic Control*, vol. 47, no. 5, pp. 793–797, 2002.
- [75] L. Pekař and Q. Gao, “Spectrum analysis of LTI continuous-time systems with constant delays: A literature overview of some recent results,” *IEEE Access*, vol. 6, pp. 35457–35491, 2018.
- [76] P. Wahi and A. Chatterjee, “Averaging oscillations with small fractional damping and delayed terms,” *Nonlinear Dynamics*, vol. 38, no. 1-4, pp. 3–22, 2004.
- [77] T. G. Molnar, T. Insperger, and G. Stepan, “Closed-form estimations of the bistable region in metal cutting via the method of averaging,” *International Journal of Non-Linear Mechanics*, vol. 112, pp. 49–56, 2019.
- [78] T. Kalmár-Nagy, G. Stépán, and F. C. Moon, “Subcritical Hopf bifurcation in the delay equation model for machine tool vibrations,” *Nonlinear Dynamics*, vol. 26, no. 2, pp. 121–142, 2001.